ALMA MATER STUDIORUM · UNIVERSITÀ DI BOLOGNA

Dipartimento di Fisica e Astronomia
Corso di Laurea magistrale in Astrofisica e Cosmologia

Real time aperture photometry with Cherenkov Telescope Array

Tesi di Laurea

Presentata da:
Simone Tampieri

Relatore:
Prof. Cristian Vignali

Correlatori:
Dott. Andrea Bulgarelli
Dott.ssa Valentina Fioretti

Sessione IV
Anno Accademico 2018–2019

A mia moglie Angela

Contents

Sommario

Il lavoro svolto nella mia tesi riguarda l'analisi del segnale proveniente da sorgenti gamma utilizzando la fotometria d'apertura in un contesto di analisi in tempo reale (i.e. Real-Time Analysis, RTA) effettuata con il Cherenkov Telescope Array (CTA). CTA è l'osservatorio di nuova generazione per l'astrofisica nei raggi gamma che fornirà una miglior comprensione dei fenomeni riscontrabili nelle parti più energetiche dello spettro elettromagnetico con una sensibilità dieci volte migliore dei sistemi attualmente disponibili.

La mia tesi si concentra sulla valutazione della significatività del segnale nell'ambito del sistema RTA, una serie di processi dove un software valuta l'osservazione in tempi molto brevi e fornisce notifiche scientifiche quando vengono individuati fenomeni transienti nel campo di vista. La RTA si occuperà di analisi su osservazioni da pochi secondi a 30 minuti, cercando eventi transienti ed avendo la possibilità di cambiare la strategia osservativa in corso e la programmazione della stessa. Un requisito centrale di RTA è la capacità di generare un'allerta scientifica entro 30 secondi dall'acquisizione del dato, quindi l'esecuzione delle mie analisi ha bisogno di rispettare questo vincolo.

Uno dei temi principali di questo lavoro è definire il tempo minimo necessario per rivelare un fenomeno transiente come un Gamma-Ray Burst (GRB). Inoltre potranno essere fornite ulteriori informazioni riguardanti la sorgente individuata, come una stima del flusso gamma e una curva di luce.

Individuare fotoni ad energie molto alte con esposizioni brevi, come 100 secondi o meno, significa operare con conteggi scarsi sia dalla sorgente che dal background; per questa ragione è stato effettuato un confronto fra i risultati ottenuti utilizzando l'analisi di massima verosimiglianza e quelli derivanti dalla fotometria d'apertura.

Per questo tipo di analisi sono stati considerati strumenti già esistenti per le consuete osservazioni su tempi lunghi ed uno in particolare è stato investigato. I risultati del confronto sono evidenziati nella tesi. Tuttavia, considerando i requisiti di RTA, durante l'evoluzione di questo lavoro è emersa la necessità di un approccio differente rispetto all'analisi di verosimiglianza sul campo di vista ed è stata sviluppata una tecnica innovativa basata sulla fotometria d'apertura.

Il metodo per valutare il segnale su osservazioni in tempi brevi, come investigato nel mio lavoro, è cruciale nella generazione delle notifiche scientifiche e nelle attività derivanti dalle segnalazioni esterne di transienti (come i *follow-up* delle onde gravitazionali), e richiede una rapida estrazione del segnale e valutazione della rilevazione rispetto alla maggioranza degli studi che usualmente vengono effettuati con dati acquisiti su osservazioni della durata di diverse ore.

Il software in cui viene implementata la fotometria d'apertura per RTA ha dimostrato di essere accurato come altri metodi ma più flessibile, di fornire diverse misure utili (come i conteggi nella regione della sorgente e nel background, oppure l'eccesso stimato), di poter generare metriche importanti (come la significatività della rilevazione o il flusso) in tempi più brevi. Inoltre sono stati identificati alcuni criteri per configurare il processo RTA in modo da individuare sorgenti simili a quelle simulate, fra cui l'*afterglow* di un GRB.

La mia tesi si sviluppa come segue:

- Il primo capitolo vuole presentare una panoramica dell'Universo alle alte energie, delle tecniche di *Imaging Cherenkov* e degli osservatori di raggi gamma, compreso CTA. In questo capitolo viene descritta anche l'RTA.

- Il secondo capitolo descrive gli aspetti teorici e pratici coinvolti nell'analisi dei raggi gamma, con interesse particolare verso l'analisi fotometrica di apertura che è la metodologia principale del mio lavoro.

- La terza parte esamina brevemente `ctools`, un pacchetto software usato per analisi scientifiche nei raggi gamma. Questo software è stato sviluppato specificatamente per i dati di CTA, ma è utilizzabile anche per altri telescopi ad *Imaging Cherenkov* come H.E.S.S., MAGIC o VERITAS.

- Il quarto capitolo illustra i risultati ottenuti con l'analisi on/off effettuata con `ctools` e con altre valutazioni fotometriche.

- Il quinto capitolo entra nei dettagli della tecnica innovativa sviluppata nell'ambito di questa tesi, sfruttando la fotometria d'apertura nei raggi gamma. Vengono mostrati i risultati ottenuti.

- Infine le conclusioni, dove viene presentato un breve riepilogo del lavoro svolto e sono indicate alcune idee per sviluppi futuri.

Abstract

The work accomplished in my thesis concerns the aperture photometry analysis applied to γ-ray source signal evaluation in the context of Real-Time Analysis (RTA) exploiting the Cherenkov Telescope Array (CTA) facility. CTA is the next generation γ-ray ground-based observatory which will provide a deeper understanding of the most energetic part of the electromagnetic spectrum with unprecedented sensitivity, a factor of ~ 10 better then current facilities.

My thesis is focused on the evaluation of the significance of the signal through the RTA system, a specific pipeline where a software evaluates the observation in short time and provides science alerts when transient phenomena are detected in the field of view. The RTA timescales span from a few seconds to 30 minutes, searching for transient events and opening to a possible change of the observational strategy and schedule. An important requirement of the RTA is to be able to generate scientific alerts within 30 seconds with respect to the data acquisition, therefore my analysis needs to respect this constraint strictly.

One of the main topics of this work is defining the minimum time needed to detect a transient phemenon as Gamma-Ray Burst (GRB). Furthermore, additional information about the detected object will be provided, such as the γ-ray source flux measurement and lightcurve.

To detect very high-energy photons in short exposure as 100 seconds or less involves low counts from source and background; in this regard, a comparison between the best fit obtained using the maximum likelihood method and the one from aperture photometry was performed.

Existing tools for standard long-time analysis have been considered and one in particular has been tested. Results of this comparison are provided in my thesis. However, considering the requirements of the RTA pipeline, the necessity of a different approach with respect to the full field maximum likelihood has emerged and a novel technique, based on aperture photometry, has been developed and is described in this work.

The method to evaluate signals on short time scales – as pursued in my work – is crucial in alerts generation context and transient follow-up activities, but it requires fast signal extraction and detection evaluation compared to the large majority of studies usually developed on data acquired over long observation time (i.e. hours).

The RTA aperture photometry tool has proven to be as accurate as other methods but more flexible, producing multiple useful measures (i.e. on- and off-source counts, estimated excess), and capable of providing important metrics, as detection significance and flux, with a faster response.
In addition, sets of constraints have been found to configurate the RTA pipeline so that it can detect targets similar to the simulated GRB afterglow.

The outline of my thesis is the following:

- The first chapter is an introduction to very high energy Universe, to the Imaging Cherenkov Technique and γ-ray observatories – among which

CTA. The RTA will also be described.

- The second chapter describes the theoretical and pratical aspects involved in the γ-ray analysis, focusing on the aperture photometry analysis that is the main topic of my work.
- The third part examines briefly `ctools`, a software package used for scientific γ-rays analaysis — for CTA data, but also other existing Imaging Air Cherenkov Telescopes (such as H.E.S.S., MAGIC or VERITAS).
- The fourth chapter illustrates the results obtained with the on/off analysis via `ctools` and other photometric evaluations.
- The fifth chapter details a novel technique developed in this work based on aperture photometry for γ-rays. The achieved results are reported.
- Finally the conclusions, where I will make a brief summary of the work carried out and indicate some possible directions for future developments.

1 Gamma-rays in multimessenger era

Starting with visible light, astronomers studied the sky since ancient times. With time the astronomers have not only improved the observation tools, but they also grasped the most profound nature of the "light messenger" unfolding the electromagnetic radiation.

Although the electromagnetic radiation is a continuous and describes the full range of existent light, astronomers provided names for different regions of the spectrum: starting from low energy radio waves and microwaves, going through infrared, visible and ultraviolet light, up to the X-rays and, finally, γ-rays. The electromagnetic radiation unfolds over twenty orders of magnitude in energy, and the different energies allow us to analyze several emitting physics processes.

Taking into account that the boundaries of the energy regions are blurred, we can consider photons with energy in the order of MeVs or greater as γ-rays photons. From this remarkable lower limit, γ-rays are categorized in "high energy" when their energy is between 30 MeV and 30 GeV and "very high energy" (VHE) for those that exceed 30 GeV and grow up to the TeV. Sometimes the term "ultra high energy" is used to indicate those in the 30 TeV – 30 PeV interval.

It is worth noting that most of the light we receive is emitted by hot objects and is known as thermal radiation, but no object can become hot enough to emit at γ-rays frequencies. Indeed, the photons in the γ-ray band represent the most energetic photons of the electromagnetic spectrum and they are products of fundamental physics happenings in the more violent processes in the Universe. Gamma-ray emission has been detected by pulsar, supernova remnants, relativistic jets from active galactic nuclei and so on.

To explore the γ-ray window provides an extraordinary picture of the non-thermal Universe and of the most spectacular events in the Cosmos.

On August 17th, 2017, a gravitational wave signal associated with the merger of two neutron stars was detected by LIGO and Virgo interferometers. The collision produced a simultaneous gravitational radiation (GW170817) and a short gamma-ray burst (GRB170817A), whose subsequent electromagnetic emissions were followed by 70 observatories in all the continents and in the space and opening a new era for the astronomy: the multimessenger era.

Nowadays astronomers are improving their understanding of the Universe not only exploring the full electromagnetic spectrum, but also investigating the elusive neutrinos from galaxies with exceptional rate of star formation or the faint gravitational waves emitted from collapsing binary systems. The γ-rays are perfect companions of all these fascinating events and to get information from all these complementary experimental branches is the key to obtain a complete knowledge of sources and environments in this multimessenger era.

1.1 The Gamma-ray Universe

Studying γ-rays means exploring the non-thermal Universe and violent phenomena in our Galaxy and beyond.

Somewhere in the Universe protons and atomic nuclei are accelerated to extraordinary high energies and, traveling very close to the speed of light, they bomb continuously the solar system. The energy of these charged particles, called cosmic rays[1] (CRs), has been increased beyond the thermal energies by the surrounding astrophysical environments.

The energy spectrum of CRs cover a very wide range of energies, and follows a power law $dN/dE \sim E^{-\Gamma}$ with different spectral indices: a first transition point is the *knee* at $E \sim 3 \cdot 10^{15}$eV, where Γ changes from 2.7 to 3. After this first change, the spectral index becomes harder at 3.3 around $E \sim 10^{17}$eV. Finally, a last transition called *ankle* flattens the spectrum with a 2.6 index at energy above $5 \cdot 10^{18}$eV. The spectrum of CRs from different experiments is shown in Figure 1. Very energetic CRs have been detected with $E \sim 10^{20}$ eV, far beyond energies achievable by the most modern particle accelerators on Earth.

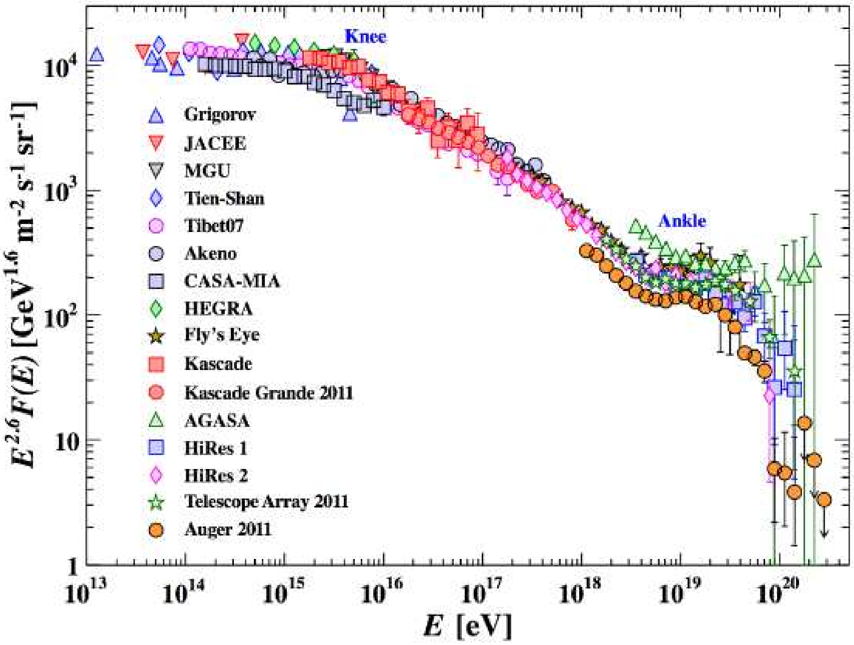

Figure 1: Cosmic-ray spectrum measured by different experiments. In the y-axis the differential flux of particles per unit energy interval $F(E)$, multiplied by energy $E^{2.6}$, is reported. The knee and ankle are evident. Image from "Cosmic Rays" from [16].

The origin of CRs is still under debate, but they can have galactic and

---

[1] The word *ray* is used for historical reasons. In 1912, V. Hess discovered a ionizing radiation originated in outer space. In 1926, R. Millikan named this radiation "Cosmic rays" thinking they were gamma rays at higher energy.

extra-galactic nature. Galactic CRs (energy up to 10^{15}eV) are assumed to be accelerated in supernova remnants, while active galactic nuclei, gamma ray bursts, quasars are potential sources for extragalactic CRs. On the one hand, as charged particles, CRs are affected by magnetic fields encountered in their path, so they cannot be tracked back to their source. On the other hand, γ rays (and neutrinos) are neutral particles and can be produced in the same non-thermal phenomena that origin the CRs.

Unlike the sky in the optical energy range, the γ-sky is dominated by diffuse background radiations. An intense Galactic component is originated by charged particles propagating in interstellar medium and emitting γ photons via π^0-decay, inverse Compton scattering and bremsstrahlung. An extragalactic background component represents the entire light emitted by stars, galaxies and active galactic nuclei over the full lifetime of the Universe. This extragalactic component will be described at the end of this section. In this background radiation, steady sources and flashes can be observed.

The Milky Way center contains several objects that could emit CRs and γ-rays. The main candidate surely is the supermassive black hole *Sgr A** hosted in the Galactic Center. It is believed to emit γ-ray photons through the π^0-decay ($\pi^0 \to 2\gamma$) produced in hadronic interactions where relativistic protons and nuclei collide producing pions, kaons and hyperons. This very high energy emission has been observed by different experiments in the Galactic Center direction but the origin is hard to track because the area is source-crowded. Recent measurements [29] interpretate the VHE emissions as the energy loss by high-energy electrons and positrons from many pulsars located near the Galactic Center. These charged particles can generate VHE photons via synchrotron radiation when they move through magnetic fields at relativistic speed or via inverse-Compton (IC) scattering when electrons lose energy in high density photon environments. The inverse-Compton scattering and the π^0-decay are believed to be the most important mechanisms to generate VHE γ-rays. Investigating areas where π^0-decay is dominant could lead to discovery of hadronic accelerators where CRs originate.

At the moment, in agreement to the TeVCat[2], pulsars and pulsar wind nebulae are the most represented galactic object emitting γ-rays at GeV and TeV energies. Pulsars (PSRs) are rotating neutron stars. If associated with an extended nebula, pulsars are classified as pulsar wind nebulae (PWNe). Both types can emit high-energy radiation, but the winds of energetic particles in PWNe are well suited to provide very high-energy γ-rays via inverse Compton effect of electrons on low-energy radiations. The most famous source of this type is the Crab Nebula, a pulsar born from a supernova explosion detected in 1054 AD and surrounded by the remnants of the progenitor star. The Crab is well-studied in all the wavelength (Figure 2) and in 2019 has been seen emitting photons with energy above 100 TeV [32].

When a massive star at the end of its life cannot oppose its internal pressure

---

[2] TeVCat is an online catalog for TeV Astronomy by S. Wakely and D. Horan from the University of Chicago. See `http://tevcat.uchicago.edu/` .

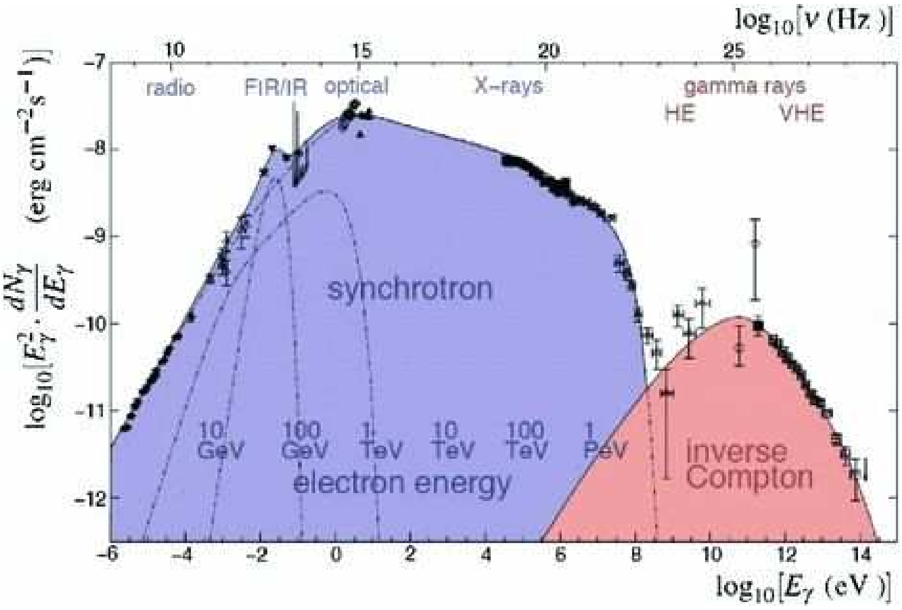

Figure 2: Multiwavelength observations of the Crab nebula. The synchrotron emission is given by the superposition of the contributions of electrons with different energies. The synchrotron spectrum provides the target photons for the inverse Compton process. Credits to M. Spurio [31].

to the gravitational forces anymore, it collapses and a Type II supernova explosion occurs. During the explosion the most external materials of the star are ejected at thousands of kilometers per second and the shockwave heats the interstellar medium creating an expanding shell of gas and dust called supernova remnant (SNR). SNRs contribute to enrich interstellar medium with heavier elements and can play a role in star formation processes. Furthermore, galactic CRs are believed to be accelerated from the shock. The study of some supernova remnants indicates that the γ-ray emission is consistent with the hadronic model [13], [19], but other contributions by the leptonic component (i.e. the bremsstrahlung process and inverse-Compton scattering) may increase the detectable flux of very high-energy photons and are debated [20], [25].

In our exploration of the Galaxy, the γ-ray binary systems have proven to accelerate particles up to very high energies. These objects have been deeply studied at X-ray wavelengths, but they populate also the γ-sky — indeed, a handful of these sources has been detected from H.E.S.S. and M.A.G.I.C. telescopes as described in [9] and [10]. When matter falls from companion to compact object a large amount of energy is released. The γ-ray spectrum to several TeV implies that the electrons and protons parent particles might be accelerated (e.g. via shocks) in accretion disks and jets and emit via synchrotron radiation or scattering abundant thermal photons to higher energy via Inverse Compton.

Another VHE emission scenario in binary systems occurs when a pulsar loses rotational energy via a relativistic wind composed by high-energy electrons interacting with surrounding plasma (see [3]). In this case Compton scattering, synchrotron radiation and π^0-decay mechanisms are involved.

Accretion disks have a critical role in very energetic emissions from extra galactic objects: the Active Galactic Nuclei (AGN). The active galaxies are characterized by supermassive black hole (SMBH) collecting matter from the surroundings. The falling matter is strongly heated in the inner parts of the accretion disk near the SMBH and radiates at optical and ultraviolet frequencies via dissipative processes, up to X-rays energies when very energetic electrons interact with photons from the very hot corona region where inverse-Compton phenomena occur. Some AGN can have a nonthermal emission when highly energetic particles are accelerated in relativistic jets of plasma that may form perpendicularly to the galaxy plane when the black hole spins and the accretion disk is strongly magnetized [33]. These jets can accelerate particles as protons up to PeV energies[3], so they can contribute to CRs generation and initiate pair cascades that can radiate synchrotron γ-rays in the high-energy regime [28].

A few times per day the γ-ray sky is characterized by extremely luminous eruptions called gamma ray bursts (GRBs) that exceed the γ-ray emission from any other source. These flashes are randomly distributed in sky directions and it is currently known that they have an extragalactic origin. GRBs are the most energetic phenomena in the Universe, and were discovered serendipitously in 1967[4] and publicly announced in 1973. The bursts are featured by amazing energy release ($\sim 10^{52}$ erg[5]) in very short time, and they are mainly classified in short-duration (from few milliseconds to about 2 seconds) and long-duration bursts (up to hundreds of seconds) — see Figure 3. Ultra-long GRBs, emitting continuously for thousands of seconds, are also under study.

With the discoveries of the Italian-Dutch BeppoSAX mission, launched in 1996, GRBs have been also characterized by a post-prompt afterglow phase. This phase lasts more than the prompt one (the typical duration time is one week) and the spectrum is distributed through all the wavelengths: indeed, the study of the afterglow emission in multi-wavelength observations was important to determinate the events' redshift and the possible origin of the main γ-ray emission.

Observations have shown that long GRBs appear where active star forming galaxies are, and a correlation with supernova events has been found in many cases [15]. The short GRB population has a higher energy spectrum than longer GRBs by many orders of magnitude and their presence has been confirmed in galaxies containing a considerable quantity of old stars compatible with neutron

---

[3] The origin of ultrahigh energy CRs is still not clear, but shocks in the backflows of radio galaxies can meet the physical requirements to accelerate particles up to the EeV regimes [35].

[4] During the Cold Wars years, USA and USSR launched military satellites to monitor nuclear weapon explosions that violated nuclear test ban treaty. In July, 1967 the U.S. Vela satellites identified suspicious gamma emissions to which a cosmic origin was attributed.

[5] As a comparison, the estimated luminosity of the Milky Way is 10^{43} erg/s. The Sun provides 10^{33} erg/s.

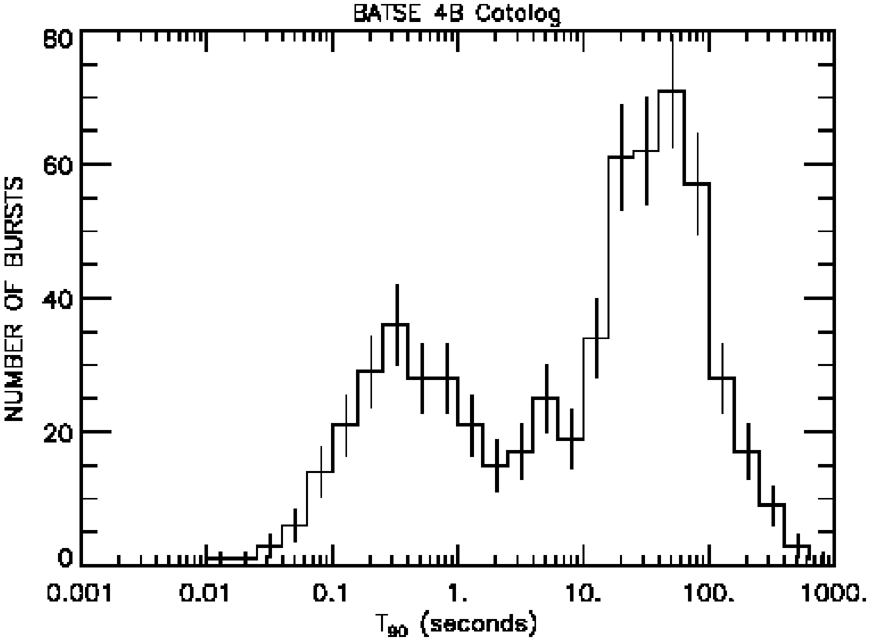

Figure 3: Durations of the 4B Catalog Gamma-Ray Bursts recorded with the Burst and Transient Source Experiment on board of NASA's Compton Gamma-Ray Observatory. The duration parameter used is T90, which is the time over which a burst emits from 5% to 95% of its total measured counts. The data used for the calculation are the BATSE 4 energy channel discriminator data. Lightcurves used for the calculation of T90 are integrated over all 4 channels ($E > 20$ keV). Image from BATSE group here `https://gammaray.nsstc.nasa.gov/batse/grb/duration` .

stars binary systems. The current hyphotesis is that short GRBs are generated from processes where two compact objects merge: when a couple of neutron stars spirals closer, in the very last moments the structure emits gravitational radiation, thermal neutrinos, and an amazing quantity of energy.

The most accredited acceleration mechanism producing γ-rays is the *fireball model* (see Figure 4) and is independent on the details of the region where it is originated. In agreement to this model, the photon emission starts with an energy release where the radiation pressure overcomes the gravity, causing an explosion of relativistic blast waves. These pressures generate different shells of progenitor matter, each moving at its own speed: when a fast shell encounters a slower one an internal shock happens and the GRB prompt emission is emitted. While shells interact with the interstellar medium, external shocks produce the GRB afterglow.

The Universe is permeated by diffuse radiation fields present at all wavelengths. The most well known radiative background is surely the Cosmic Mi-

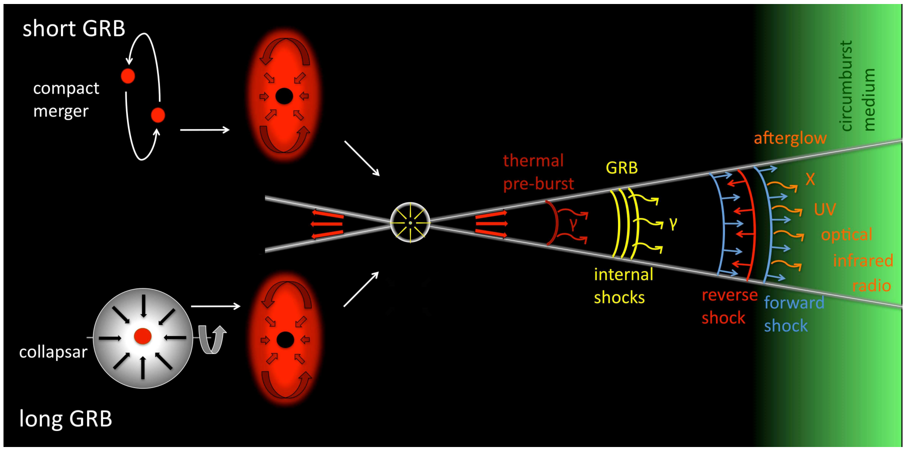

Figure 4: Production sites of γ-ray and afterglow emission in the fireball model. Progenitor models for short and long GRBs are shown on the left. Image from [18].

crowave Background (CMB) that provides information about the very early Universe and dominates at longer wavelengths. The total light emitted by stars, galaxies and AGN in all the epochs is a pervasive background radiation spanning from ultraviolet to infrared frequencies and it is called Extragalactic Background Light (EBL). When a very high energy photon travels through the intergalactic medium, the interaction between it and an EBL photon will lead to the pair creation $\gamma + \gamma_{background} \rightarrow e^{+} + e^{-}$ and to the absorption of the very high energy extragalactic photon. The interaction is dependent on the EBL's spectral energy distribution and the redshift of the γ-ray source. Direct measurements of EBL are hard to take and a wide range of models has been developed (see, for instance, Finke et al. 2010 [14], Gilmore et al. 2012 [17]).

1.2 The Imaging Cherenkov Technique

The Earth's atmosphere is opaque to γ-rays: when a very high energy photon interacts with the atmosphere it produces electron/positron pairs (Figure 5). These secondary particles provide new secondary γ-rays via a bremsstrahlung mechanism that emits pairs again, creating an electromagnetic cascade with a so-called "shower effect"[6]. A great number of these particles travel with relativistic speed through the atmosphere generating Cherenkov light — a detectable near-UV radiation flash at 300–350nm. When a charged particle traverses a medium with a speed larger than light speed in that medium, Cherenkov light is emitted. Conversely to optical telescopes, the Cherenkov telescopes do not look at celestial objects, but record nuclear reactions in the atmosphere

---

[6] As historical note, the term "shower" is the English translation by P. Blackett of the Italian expression "sciame", first used by B. Rossi (citing [31]).

following the Cherenkov flashes that accompany them.

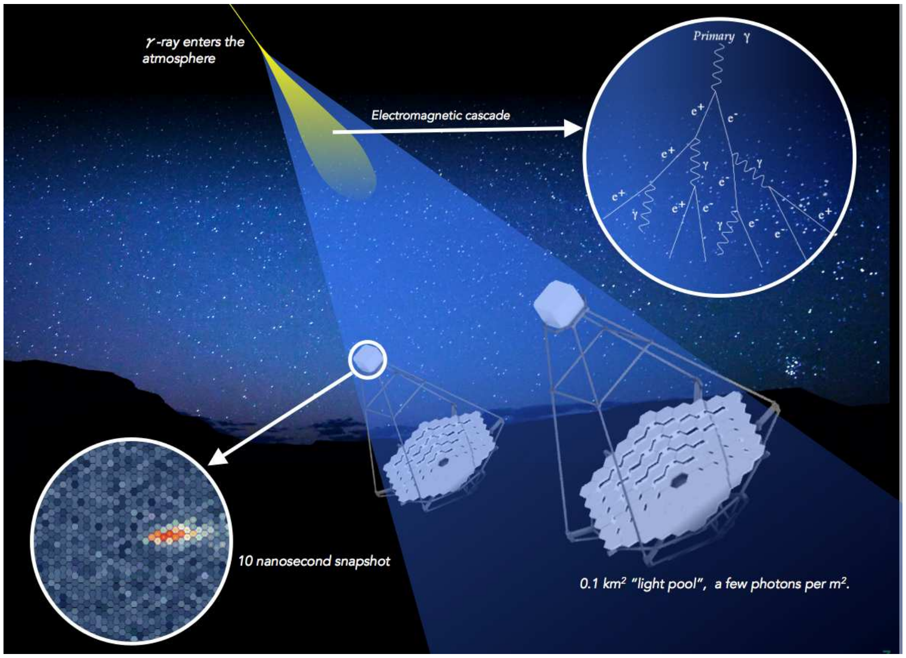

Figure 5: Image explaining how CTA detects Cherenkov light produced by a primary γ-ray interacting with the Earth's atmosphere. Credits to `https://www.cta-observatory.org` .

When high-energy γ photons and CRs impinge the Earth's atmosphere, the interactions with atmospheric nuclei create secondary particles that induct the shower. The shower creation persists until a specific energy threshold[7] is reached and the maximum number of shower particles was produced. This maximum emission occurs at an altitude of about 10 km above the sea level for primary particles in the 100 GeV–10 TeV energy range.

An electromagnetic cascade (containing e^+, e^- and γ-rays) propagates Cherenkov light as a cone with a maximum emission angle $\theta_C = \cos^{-1}(1/n) \approx 1.3^\circ$ at standard temperature and pressure (STP) conditions. The angle increases going from top to ground level following the atmosphere's refraction index n that changes with altitude. An electromagnetic shower can propagate for 10 km resulting in a projected light pool with about 120 meters radius at ground level (about 2000 meters on sea level). The Imaging Atmospheric Cherenkov Telescopes (IACTs) use wide-field mirrors to focus the light pool towards high-speed cameras to detect nanoseconds-lasting faint Cherenkov flashes.

---

[7] The energy at which radiation energy losses equal those derived from excitation/ionization. This energy depends on the medium refraction index, therefore can change at different altitudes.

The shower image, an approximately elliptical shape on the camera, is analyzed in an early phase to reconstruct the primary γ-ray origin, energy and direction. The electromagnetic showers, like those initiated by γ-rays, are different from the hadronic showers initiated by CRs (protons and nuclei). The former showers project compact elliptic shapes on the focal plane, while the latter have larger structure deriving by π^0 decay and can be therefore distinguished. The air showers initiated by electrons/positrons[8] constitute irriducible isotropic background for IACT detectors because they have the same development as those deriving by γ-ray photons.

The efficiency in discriminating between hadronic and γ-ray showers defines, among other parameters, the minimum detectable flux (the sensitivity) of the telescope.
After raw data are collected, an image cleaning process occurs to reconstruct the shower information needed to perform the parametrization of the shower itself.

The fundamental image parameters were introduced by A. M. Hillas [5] in 1985, when single telescope configuration was still used. Through these parameters it is possibile to evaluate the obtained Cherenkov images and achieve a good γ-ray/hadron separation.

- SIZE is the total number of photoelectrons in the shower image. It is proportional to the energy of the incoming primary γ-ray or particle;
- LENGTH is the half of the major axis of the shower image;
- WIDTH is the half of the minor axis of the shower image;
- FRAC measures the general concentration of light;
- MISS is the perpendicular distance of the center of the field (where the source is supposed to be in single telescope configuration and pointing in center of field of view) from the image axis;
- AZIMUTHAL-WIDTH is the image width relative to a new axis which joins the center of the field to the centroid of the image;
- DISTANCE is the distance of the brightest point from the center of the field.

Through these parameters (Figure 6), Hillas noticed hadronic showers had wider images, not systematically aligned with the source because isotropic, while γ-ray showers were more collimated.

When the source is not in the camera center (i.e. the telescope is pointing in Wobble mode, see section 2.5), new useful parameters are used to track the source position:

---

[8] Electrons constitute about 1% of galactic cosmic rays [31].

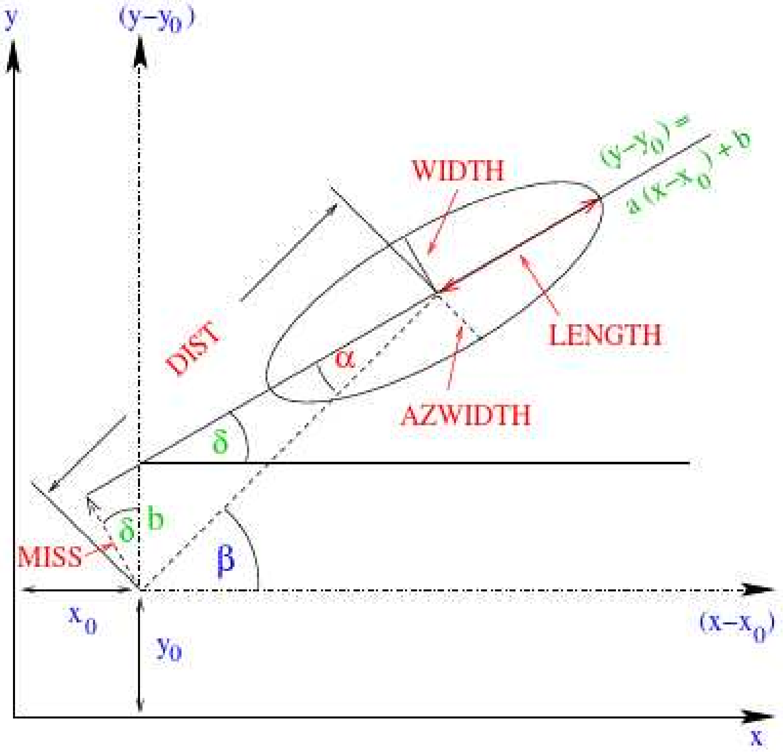

Figure 6: Parametrization of a shower image through Hillas parameters. The nominal position of the observed source is (x_0, y_0). The full parameters description is provided in the main text. Credits to [22].

- ALPHA is the angle between the major axis of the ellipse and the direction of the source position from the center of gravity of the image;
- DIST is the distance of the center of gravity of the image from the source position.

The ALPHA parameter has the highest γ-hadron separation power since γ-ray images have small values, while hadron images have flat distributed ALPHA angles.

Observations of individual showers with array of Cherenkov telescopes allows a three-dimensional reconstruction of γ-ray showers in a more effective stereoscopic observation[9]. Reconstruction algorithms are used to point back to the astrophysical source and to discriminate the electromagnetic showers from

---

[9] Quoting [31], the stereo observation increase the background suppression efficiency by a factor about 100, improves the angular resolution and enable morphological studies of extended γ-ray sources.

the hadronic showers produced by isotropic cosmics rays. These algorithms are based on Hillas' parameters and are implemented with statistical techniques like the *Random Forest* regression method [12].

After this step, the reconstructed data can be collected and processed to provide science results.

1.3 Previous very high-energy experiments

Gamma-ray signals have been studied in various ways over the time since the 1960s: using balloons, water ground-based detectors, imaging ground-based telescopes and detectors on spacecraft.

In the sixties γ-ray emissions were detected by instruments on satellites (Vela, OSO3) but the first detailed sky map were took in the seventies with SAS-2 and Cos-B satellite missions. The resolution of these instruments was insufficient to detect most of γ-ray point sources, but they recorded the diffuse Galactic emission due to the interactions of CRs with the interstellar medium, some pulsars and unidentified objects[10].

In the 90's two important satellites took off: the Compton Gamma Ray Observatory (CGRO) and BeppoSAX. CGRO carried different instruments for specific gamma-ray astronomy: among them, the Burst and Transient Source Experiment (BATSE) contribution was remarkable as it led to the detection of one GRB per day (for about 2700 total detections). The Energetic Gamma Ray Experiment Telescope (EGRET) was the high-energy instrument on CGRO, covering the energy range from 20 MeV to 30 GeV, and it conducted the first survey above 100 MeV. BeppoSAX identified the first non-gamma ray counterpart to a GRB, opening the way to a better characterization of GRBs and their extragalactic distance. These space missions were followed in 2000s by Swift, INTEGRAL, Fermi and AGILE that contributed to map the γ-ray emissions from pulsars, GRBs, microquasars, black holes and background radiation.

Recent space experiments cover a γ-ray energy interval from a few MeV to hundreds of GeV. However, beyond the GeV range the γ-ray fluxes are so small that the effective detection area of space-based experiments cannot provide a sufficiently large collection of events, so the astrophysics studies rely on ground-based detectors[11].

Starting with the Whipple Telescope in Massachussets in 1968, the ground-based telescopes have grown in number and technologies. The Imaging Air Cherenkov Technique was developed in the 70s, just with the Whipple telescope; since then the field has been demonstrated to provide contributions in astrophysical observations and particle physics. In the last two decades ground-based gamma-ray astronomy has experienced impressive astrophysical results obtained with facilities like H.E.S.S., VERITAS and MAGIC. A short summary is in Table 1.

---

[10] One of the best known results of Cos-B is the 2CG catalogue with 25 γ-ray point sources discovered in three years. See `https://sci.esa.int/s/8OpVjpA` .

[11] The Fermi effective collecting area is ~ 6500 cm^2 at 1 GeV.

The High Energy Stereoscopic System (H.E.S.S.) has a five telescope configuration (four 12 meters in diameter mirrors, with a larger 28 meters mirror built in the center of array) which allows to investigate γ-ray sources in the energy range from 10s GeV to tens of TeV with intensities much lower than the Crab Nebula flux. H.E.S.S. is operative in Namibia since 2002 and was updated in 2012 with the 28 meter mirror. Over time it has detected several TeV γ-ray sources and reported the presence of petaelectronvolt protons from the supermassive black hole at the Milky Way center [26] in 2016.

The Very Energetic Radiation Imaging Telescope Array System (VERITAS) is another ground-based γ-ray observatory with a peak effective area of 100,000 m^2 to receive signals from very high energy band. VERITAS was designed on the Whipple project (decommissioned in 2013) and was originally planned as an array of seven telescopes, but only four were built. In 2009, one telescope was moved to a new location to improve the system sensitivity. The VERITAS telescopes are able to slew simultaneously at a rate of 1° per second in elevation and azimuth enabling the GRB observations. Since 2008, VERITAS has discovered new TeV sources and allowed to study SNRs and Crab Nebula deeply. Furthermore, it has observed over one hundred AGN and it has an extensive Dark Matter program.

The Major Atmospheric Gamma-ray Imaging Cherenkov (MAGIC) is a two-mirror Cherenkov telescope with a very fast repositioning (7 degrees per second) of about 40 seconds on average in order to quickly react to alert for transient events like GRBs. The dish of both telescopes has a 17 meters diameter and they were installed on Canary island of La Palma in 2004 and 2009. More technical and performance information are described in [24]. Until the advent of the CTA observatory, MAGIC is the most advanced Cherenkov telescope for gamma astronomy.

Instrument	Emisph.	Alt.	no. tel.	FoV	ang. res. at 1 TeV	slewing time (s)	energy range
Whipple	North	2300	1	2.6	0.12	180	300GeV–10TeV
H.E.S.S.	South	1800	4	5.0	0.1	n/a	30GeV–100TeV
H.E.S.S. II	South	1800	1	3.2	0.4	61	30GeV–100TeV
VERITAS	North	1275	4	3.5	0.08	100	85GeV–30TeV
MAGIC	North	2230	2	3.5	0.07	40	30GeV–100TeV

Table 1: Summary of Cherenkov observatories. The altitude is in meters, field of view in degrees. The slewing time is intended as an approximation. Information about these telescopes are eterogeneous given the composite nature of these detectors systems. Whipple project is showed for historical reason (it was decommissioned in 2013). Furthermore, many facilities have been updated changing initial characteristics: Whipple has improved its angular resolution from initial 0.3 degree, HESS installed a new mirror (H.E.S.S. II) and the NECTAr faster chips, and so on.

1.4 The CTA observatory

The Cherenkov Telescope Array represents the state of the art for the γ-ray detections at ultra-high energy. This ground-based telescope will bring a significant improvement in terms of accuracy and sensitivities in the γ-ray astronomy and a broader than ever observable energy interval — from tens of GeV to the hundreds of TeVs.

CTA will be composed with more than 100 telescopes: about 19 in the northern emisphere, in La Palma island, and 99 telescopes in the southern emisphere in the Atacama Desert in Chile. The northern site array, with large and medium size telescopes spread in about 0.5 km^2 area, will focus on low-mid energy range, from 20 GeV to 20 TeV. The southern site array will cover energies from 20 GeV up to 300 TeV with the full range of telescopes (small, medium and large sized) built in about 5 km^2 area in Paranal.

The CTA telescopes are from three different classes, each covering a specific energy range. The Table 2 is a short summary about the different classes of CTA telescopes.

Instrument	number of telescopes	FoV	ang. res. at 1 TeV	slewing time (s)	energy range
LST	4N + 4S	4.5	n/a	30	20GeV–150GeV
MST	15N + 25S	8.0	n/a	90	150GeV–5TeV
SST	0N + 70S	10.0	n/a	60	5TeV–300TeV
North or South full array			0.05		20GeV–300GeV

Table 2: CTA telescopes summary. The field of view is reported in degrees. The angular resolution is given only for a full array configuration and not for telescope's size.

At the center of the northern and southern sites a set of 4 large-sized telescopes (LST) will rise to catch the fainter Cherenkov lights from the low-energy gamma rays (20-200 GeV) with a 4.5 degrees field of view. The large telescopes are amazing instruments that can re-position their 400 m^2 mirror with a 28-meters focal in tens of seconds to allow quick follow-ups of transient (i.e. GRBs) alerts. The first LST prototype, LST-1, was completed at La Palma, Canary Islands, in October 2018 and detected its first γ-ray signal on 23 November 2019 pointing the Crab Nebula[12].

About 40 medium-sized telescopes (MST) will be in the array, covering 100 GeV–10 TeV energies. The MSTs will be placed in both the emispheres and scattered around the large-sized telescopes and spaced about 100 meters from each other. The MST mirror is 12 meters in diameter with an 8 degrees field of view, useful for a rapid survey of γ-ray sky.

The small-sized telescopes (SSTs) will outnumber all the other detectors in an array with 70 units. The SSTs will be sensitive at the higher energies

---

[12] `https://www.cta-observatory.org/lst1-detects-first-gamma-ray-signal/` .

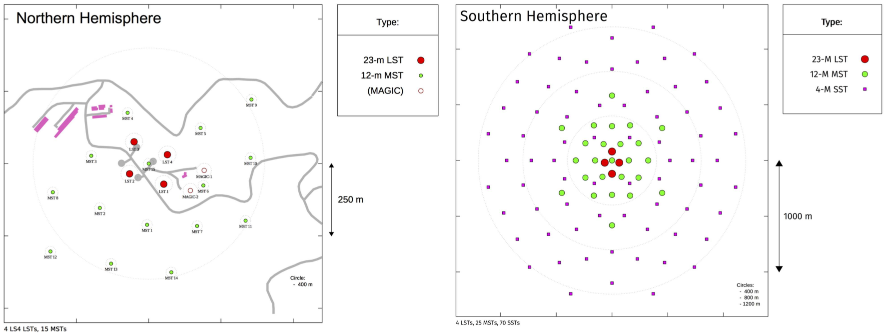

Figure 7: The proposed layout for all the types of telescopes in the CTA project, in Northern (left) and Southern (right) sites. Credits to `www.cta-observatory.com` .

detecting γ-rays from a few TeVs up to hundreds of TeV with 4 meters in diameter mirrors[13]. Operating in the most extreme energy range (as 5 TeV–300 TeV) where the number of detected γ-rays showers will be rarer, SST array need to cover an area of several square kilometers.
The proposed layout for all the CTA telescopes is displayed in Figure 7.

The current baseline design of CTA foresees a factor of 10 improvement in sensitivity in the current energy domain of about 100 GeV to some 10 TeV and an extension of the accessible energy range well below 100 GeV and above 100 TeV (see Figure 8).

The southern hemisphere array will cover the full energy range from tens of GeV to hundreds of TeV to allow a deep investigation of the central part of the Galactic plane and see most of the Galactic sources. Indeed, a key science project of CTA is the Galactic Plane Survey that will cover the entire Galactic plane looking for very high energy source population as PWNe, SNRs, and binaries [34]. The northern hemisphere array will be optimised for extragalactic astronomy, and will consist in the low-medium energy instrumentation (up to about 1 TeV). The EBL attenuation on TeV photons provides an effective horizon that makes sensitive instruments with low energy thresholds more suitable to detect distant objects.

The CTA Consortium, established in 2008, includes over 1300 members from 210 institutes in 32 countries in all the continents. Therefore, the CTA collaboration can be defined as a world wide effort promoting a strong and true no-barrier cooperation.

---

[13] One among SST prototypes is the italian ASTRI project, a dual-mirror Schwarzschild-Couder configuration that detected its first Cherenkov light in 2017, and achieved the first Crab detection in December 2018 [37].

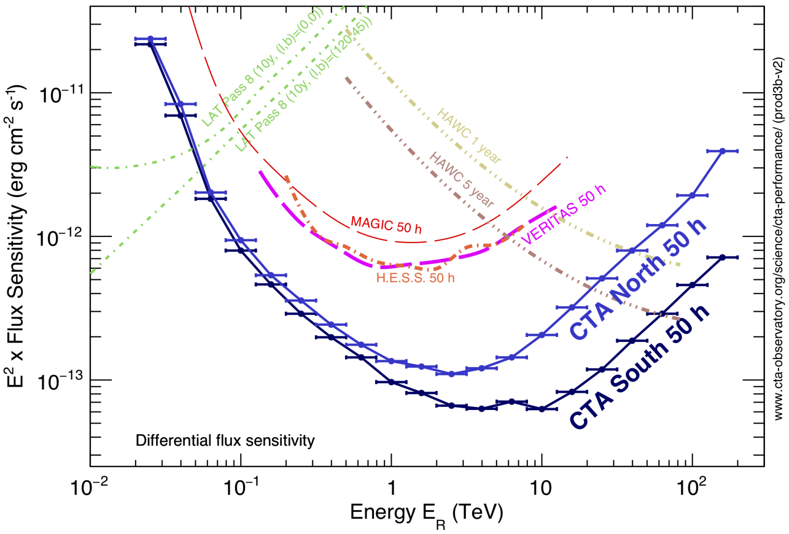

Figure 8: Sensitivity curves of different very high-energy facilities. The CTA data are from the more recent public version prod3b-v2 IRFs. Credits to `www.cta-observatory.com` .

1.5 The Real-Time Analysis

The Real-Time Analysis (RTA) is a software system that analyzes CTA data while the observation is in progress. The scope of this software is to detect unexpected events and trigger science alerts when transient phenomena are identified with specific time contraints. The RTA workflow must be operative during the observation to monitor the field of view for variability on a wide range of timescales and to provide scientific feedbacks that could change the observation strategies in live time.

To maximize the scientific return, the CTA observatory will have to be able to detect transient sources and to broadcast fast alerts with a latency of 30 seconds with respect to the last acquired event. It will search phenomena on different timescales – from seconds to hours time windows – and with an analysis sensitivity not worse than a factor of 3 than the final one [21].

Thanks to its large sensitivity and fast slewing ability, CTA will play a crucial role in very high energy counterparts searches in gravitational wave and neutrino follow-ups. The key science projects which rely on the short-timescale capabilites of CTA include transients as GRBs and PWN flares, flaring activities by AGN, and variable objects as γ-ray binaries on the Galactic Plane.

The RTA requires effective systems communications with strict time constraints, speed and accuracy in analysis process which should last between 10 seconds to 30 minutes, but also a flexibile strategy to detect different types of transient phenomena or serendipitous discoveries, and reliability — the expected RTA availability must be greater than 98%.

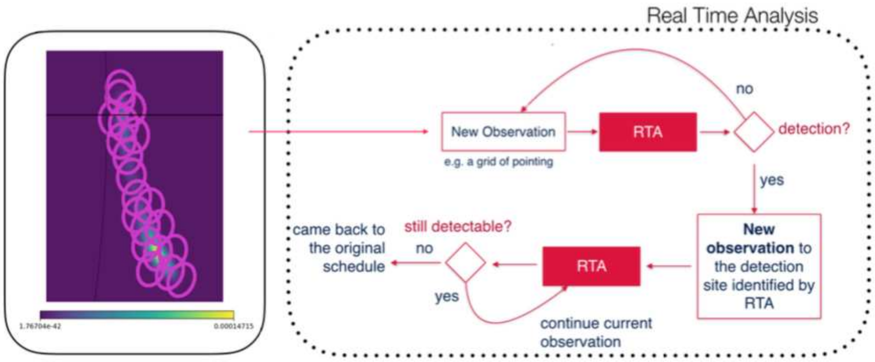

Figure 9: A gravitational wave follow-up program of CTA with the RTA pipeline. On the left side, the gravitational wave sky map with superimposed in purple the CTA pointings to inspect with RTA software is shown; this follows the algorithm on the right side of the figure. Modified from an original drawing by ICRC2019 [36].

In Figure 9 a gravitational waves follow-up is shown. After the gravitational waves detections, an array of positions to be verified will be evaluated by the CTA observation scheduler. A sequence of observations will be analyzed by the RTA software to identify the electromagnetic emission position corresponding to the gravitational signal. If no detection is localized, a new observation from the starting array is selected and analyzed. If RTA finds an electromagnetic signal in the chosen area, a second step begins and the RTA pipeline evaluates the γ-ray signal and stays on the same area following the electromagnetic transient until the flux has a satisfying significance. When the identified transient has faded, the specific observation is ended and the telescope returns to the original schedule preceeding the follow-up.

The RTA will be a key system in the multi-messenger context and multi-wavelength astronomy and this software will be installed and run on-site, with the telescopes.

2 Analysis of Gamma-ray signals

In this chapter I will describe different aspects of signal analysis in the very high energy γ-rays context. Due to the astrophysical characteristics of the γ radiation and the features of the telescopes used to collect the signal, several techniques are used through various steps to provide reliable results.

When a high-energy photon, emitted by a γ-ray source, collides with the Earth's atmosphere, the net result is an electromagnetic air shower that produces Cherenkov emission then observed with an array of optical telescopes on the ground as described in section 1.2. The light generated in the shower triggers the telescope, and the incoming signals are cleaned and classified to reconstruct the primary event. Unfortunately, the observations are highly dominated by background events originated mainly by cosmic hadrons, therefore major effort is needed to discriminate astrophysics events and background. Finally, a list of reconstructed photons is provided and the high-level γ-ray analysis will be performed to evaluate the signal and to provide skymaps, spectra and lightcurves. Different approaches can be followed for this kind of analysis, and they will be described in the following sections.

2.1 The aperture photometry analysis

Measuring the photons received from astronomical sources is the main way to get information about the sources themselves. The aperture photometry is a technique to collect fundamental photometric qualities (as the number of photons) from astronomical images in specific regions of interests. Starting from a photon list it is possible to estimate the source event counts applying the so-called on/off method. Conventionally, a closed region (the aperture) containing the source is centered on the source itself and used to count the on-source photons N_{on}. Unfortunately, this is not sufficient to evaluate the contribution of photons by the source: a pervasive background needs to be removed from "behind" the object in the aperture. A background estimation is derived observing one (or more) off-source region with no source signals in. The number of photons N_{off} inside the off regions is the contribute from background apertures. If it is desiderable to use many and large background regions to get good statistics, it is also important not to contaminate the data with background counts too different from those expected in the source one. Therefore background regions must have the same characteristics of the source region, as far as possible.

The excess photons from the source are calculated subtracting the normalized number of off regions events from the on-region data. The probable number of photons contributed by the source is:

$$N_S = N_{on} - \alpha N_{off} \tag{1}$$

where N_{on} are the counts in the source region, N_{off} are the entries in only background regions and α is a background scale factor. To achieve a valid background statistics, several observations are usually necessary, introducing more scaling factors to consider, because the on and off observations are characterized by different effective area (A), and/or exposure (t) and/or size of the region (k):

$$\alpha = \frac{A_{on} \cdot t_{on} \cdot k_{on}}{A_{off} \cdot t_{off} \cdot k_{off}} \ . \tag{2}$$

Having extracted the counts in the on and off regions and the excess counts, it is possible to estimate the detection significance, the source flux and the lightcurve with no modelling and in a simple and fast way.

2.2 The full field maximum likelihood analysis

Another popular method to analyze the data is the likelihood statistical technique, used to quantify the relative extent to which the data support a statistical hypothesis [8]. The likelihood is the joint probability of the observed data given the hypothesis and can be used to estimate parameters through its maximization — hence the expression "maximum likelihood estimation".

Likelihood analysis can be performed in binned or unbinned way, taking into account the number of events available for bin (e.g. pixels or time). For photon counting experiments, the binned likelihood that observed data are following a specific γ-rays emission model is given by the product of the probability for the finite number of i bins

$$L = \prod_i P(i) \tag{3}$$

where

$$P(i) = \frac{\theta_i^{n_i}}{n_i!} e^{-\theta_i} \tag{4}$$

is the Poisson probability of observing n_i count when the predicted count by model is θ_i. The logarithm of likelihood used to estimate the parameters is

$$\ln L = \sum_i n_i \ln \theta_i - \sum_i \theta_i \tag{5}$$

where the $n_i!$ from equation 4 is model independent therefore it is ignored, n_i is the number of observed events for each bin, and θ_i is the predicted number of events from model[14].

When the number of events for bin is small, unbinned likelihood analysis is preferable. With a very fine mesh of bins, n_i is either 0 or 1, and likelihood becomes

$$\ln L = \sum_i \ln I(i|M) - \sum_i \theta_i \tag{6}$$

where $I(i|M)$ is the probability density of receiving a photon i at the point where one was received, given the model M.

---

[14] It is worth noting that the first term in equation 5 increments the likelihood when predicted counts are where real counts actually occur, while the second term subtracts the prediction value dampening excessive assessments by the model.

The ratio between two likelihoods allows to compare the two models: indeed, the likelihood ratio test is used to compare a null hypothesis for the data divided by the likelihood of alternative hypothesis for the same data. The likelihood ratio test becomes particularly useful applying the fundamental Wilks' theorem [1] that proves that the statistic distribution of the log-likelihood ratio

$$TS = -2 \ln \frac{L_{null}}{L_{alt}} \tag{7}$$

when null hypothesis is true, is expected to asymptotically follow χ^2_{n-m}, except for terms of order $N^{-1/2}$ where N is the number of samples and $n - m$ is the number of degrees of freedoms. The parameter estimation via likelihood ratio in high-energy astronomy was performed by Cash in the late seventies [2].

A likelihood analysis on a full field of view offers the potential to reach great sensitivity and accurate flux measurement, as backgrounds can be modeled out and detailed source models can be applied.

2.3 Evaluating detections with Li & Ma significance

The procedures to analyze results in γ-ray astronomy experiments are examined in the 1983 Li and Ma article [4]. Particular attention is needed to determinate the confidence level of a candidate source, distinguishing an excess associated with a genuine source from background fluctuations and systematic effects that should have been removed.

Li and Ma show, through Monte Carlo simulations, that the significance based on standard deviation of the number of background photons (i.e. $\hat{N}_B = \alpha N_{off}$), (a) does not follow a Poisson distribution if $\alpha \neq 1$ when the significance $S = N_S \,/\, \sqrt{\alpha N_{off}}$, and (b) underestimates the statistical error of the signal and overestimates the significance when $S = N_S \,/\, \alpha\sqrt{N_{off}}$.
Furthermore, similar considerations are made for significance evaluated as $S = N_S/\sqrt{N_{on}}$ and $S = N_S/\sqrt{N_S}$.

Therefore, Li and Ma solve the estimation of the significance issues with the likelihood ratio method.
Starting from equation 1 and using the Wilks' theorem [1] to test the null hyphotesis that all the observed photons are due to background, Li and Ma define the maximum likelihood ratio as the rate of probability of null hyphotesis versus the alternative hyphotesis as follows.

The null hyphotesis has signal $N_S = 0$ and extimated background counts as $N_B = (\alpha/(1+\alpha)) \cdot (N_{on} + N_{off})$, so the likelihood function is:

$$\begin{aligned} L_{null} &= P_r\left(N_{on}, N_{off} | \langle N_S\rangle = 0, \langle N_B\rangle = \frac{\alpha}{1+\alpha}(N_{on} + N_{off})\right) \\ &= P_r\left(N_{on} | \langle N_{on}\rangle = \frac{\alpha}{1+\alpha}(N_{on} + N_{off})\right) \\ &\quad \cdot P_r\left(N_{off} | \langle N_{off}\rangle = \frac{1}{1+\alpha}(N_{on} + N_{off})\right) \end{aligned} \tag{8}$$

and the alternative hyphotesis function is:

$$\begin{aligned} L_{alt} &= P_r(N_{on}, N_{off} | \langle N_S \rangle = N_{on} - \alpha N_{off}, \langle N_B \rangle = \alpha N_{off}) \\ &= P_r(N_{on} | \langle N_{on} \rangle = N_{on}) \cdot P_r(N_{off} | \langle N_{off} \rangle = N_{off}) \ . \end{aligned} \tag{9}$$

Developing the calculations from the two previous equations 8 and 9 with a Poissonian distribution

$$P(k) = \frac{n^k}{k!} e^{-n} \tag{10}$$

where n is the expected number of events and k is the number of observed events, the resulting maximum likelihood ratio is:

$$\begin{aligned} \lambda &= \frac{L_{null}}{L_{alt}} \\ &= \left[\frac{\alpha}{1+\alpha} \left(\frac{N_{on} + N_{off}}{N_{on}} \right) \right]^{N_{on}} \left[\frac{1}{1+\alpha} \left(\frac{N_{on} + N_{off}}{N_{off}} \right) \right]^{N_{off}} \ . \end{aligned} \tag{11}$$

In this case Li and Ma test the null hyphotesis with only one free parameter that is the expectation of the number of source photons $\langle N_S \rangle$.

According to the Wilks' theorem, if the null hypothesis is true, $-2 \ln \lambda$ follows a χ_1^2 distribution, and if u is a standard normal variable, u^2 will follow a χ_1^2, so we have:

$$\begin{aligned} -2 \ln \lambda &\sim \chi^2(1) \\ u^2 &\sim \chi^2(1) \end{aligned}$$

from which the authors take the value $(-2 \ln \lambda)^{1/2}$ as significance:

$$S = \sqrt{2} \left\{ N_{on} \ln \left[\frac{1+\alpha}{\alpha} \left(\frac{N_{on}}{N_{on} + N_{off}} \right) \right] + N_{off} \ln \left[(1+\alpha) \left(\frac{N_{off}}{N_{on} + N_{off}} \right) \right] \right\}^{1/2} \tag{12}$$

If an event was obtained by a single observation and N_{on} and N_{off} counts are not too few, the value of significance is evaluated by equation 12. The probability that an event with a significance which is not less than S is produced by background can be evaluated with the standard Gaussian probability

$$p = N(u = S; \mu = 0, var = 1) \tag{13}$$

The article proves the equation 12 can be applied with fewer counts ($N_{on} \geq 10$ and $N_{off} \geq 10$) and it is consistent with Gaussian probability and can be applied also when $\alpha \neq 1$.

2.4 The reflected-region background

The ground based very-high energy γ-ray telescopes have remarkable sensitivity but to achieve their full detecting potential they need to handle a main source of systematic error: the subtraction of background. The background estimation in γ-ray data analysis is a key element in Imaging Atmospheric Cherenkov techniques. In the low-level reconstruction phase it is mandatory to distinguish CR induced hadronic showers by the γ-ray initiated showers. Later, in the high-level data science analysis, it is needed to evaluate the γ-ray signal from the science target. As described in § 2.1, to perform an aperture photometry analysis it is needed to count photons in on source region and subtract an estimated background.

Many background strategies can be adopted to estimate an observation background [11], and the common goal is to provide the better estimation of the term αN_{off} from equation 1.

The reflected-region background model was originally developed for wobble observation (§ 2.5) where the source was not at the center of the field of view but displaced with an offset with respect to the telescope pointing direction. The simplest reflection estimation uses a single off region in the opposite direction relative to the center of the field, with the same shape of the on source region. To have a better statistics in the background measurements, the method can be generalized using a number of background regions equidistant from the telescope pointing direction (see Figure 10). Off regions near the one of the source are avoided to prevent the contamination by spilled counts from the on region.

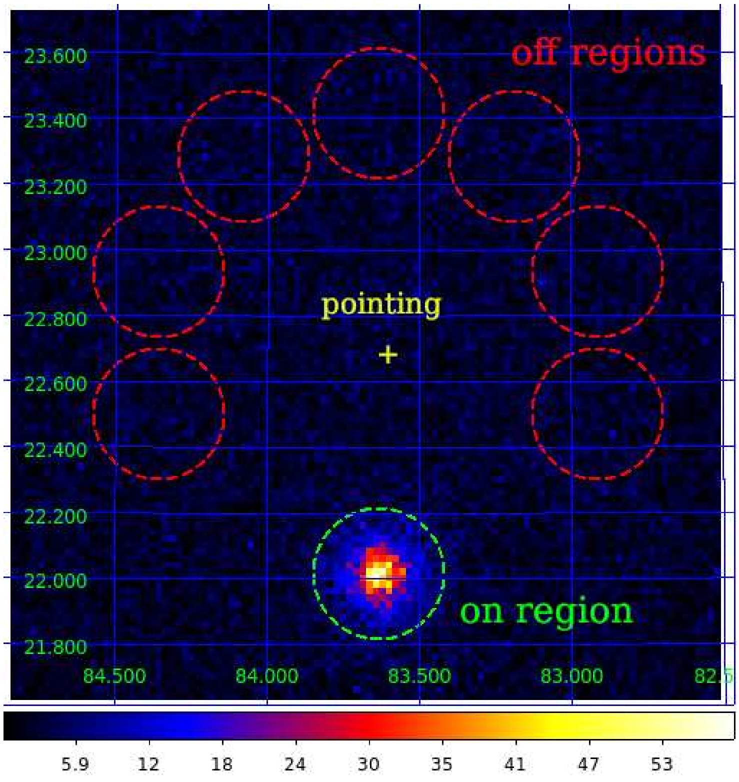

Figure 10: Reflection algorithm with a 0.7 degrees angular distance between source and pointing direction.

The sum of the event counts N_{off} from these off regions are used to estimate the background of on region, scaled by an α factor – the number of off regions. This method cannot be used without an appropriate offset between pointing and source direction that avoids overlapping between regions.

2.5 The wobble method

In a typical observation the source is located at the center of field of view. To determinate the background counts, an analogue sky region must be observed with the possibility that the observational conditions may be different (clouds, humidity, lights, etc.). The background region is chosen in a such way that during the off observation the telescope tracks the same range of zenith angles as during the source tracking.
Furthermore, having to take these different pointings into account, the overall observation time will be splitted between pointings, reducing the crucial collecting time on the γ-ray emitting source.

Exploiting the wide field of view typical for IACTs, the observations are often performed in the so-called "wobble" mode, an observational strategy where the pointing of the telescope is slightly off-axis with respect to the source center under observation. Instead of observing the source at the center of the field of view, the telescope points with an offset with respect to the source position and extracts signal from the on region while the background counts will be extracted from at least one false-source (or *anti-source*) region (see [7]) placed at a symmetrical position with respect to the pointing direction. The resulting distance between source and false-source regions is chosen in a way that background measurement is not influenced by the source presence itself. Under such observation mode, the on and off regions are observed at the same time, making more efficient the limited duty cycle of these telescopes. The region radius is fixed during all the observation time. For extended sources, typically only a single off region is considered in order to avoid overlap of the on and off circles.

Due to the alt-azimuth mount of the telescope, the on-source and false-source regions rotate around the center of the camera following the circumference of radius equal to the source-pointing distance. In Figure 11 two false sources are selected. In this case, the candidate γ-ray event rate for the source is the difference between the rate at the source position and the average rate at the two false source positions. The significance of the signal is

$$SNR = \frac{R - (F_1 + F_2)/2}{[R + (F_1 + F_2)/4]^{1/2}} \tag{14}$$

where R denotes the rate of gamma-ray showers at the source position and F_1 and F_2 denote the rate at the false source position [7].

This tracking mode captures photons spreading systematics errors and keeping the same observing conditions for all the considered regions, thus increasing the accuracy of cosmic-ray background. Moreover, this observation mode increases the available observation time while decreasing systematic differences

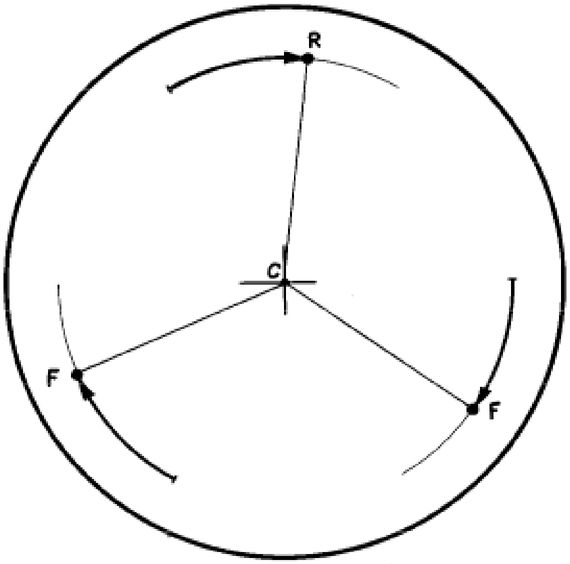

Figure 11: Movement of the real and the false sources in the field of view of the telescope in the tracking method when the telescope mount is altitude-azimuth. F is the false source, R is the real source, C is the center of the field of view. Solid lines are the movement trajectories. Original image from [7].

between on and off regions. The duration of the observation session is limited only by zenith angle and external conditions (i.e. weather). The wobble strategy involves a loss of sensitivity due to off-axis observation, but this is compensated by the possibility to observe the source continuously.

For the CTA's Large Size Telescope inaugurated the October 10th, 2018 in La Palma, a wobble observation mode will be adopted. The LST-1 observation strategy will be the following: adopting a shift between pointing and source position between 0.4 and 0.8 degrees, the source position will be swapped of 90 degrees every 20 minutes, as illustrated in Figure 12. Then the procedure will take off counts from 3 fake regions in the same time of the source region, saving observation time and recording background counts at the same conditions. This pointing strategy will be used in the analyses described in § 5.

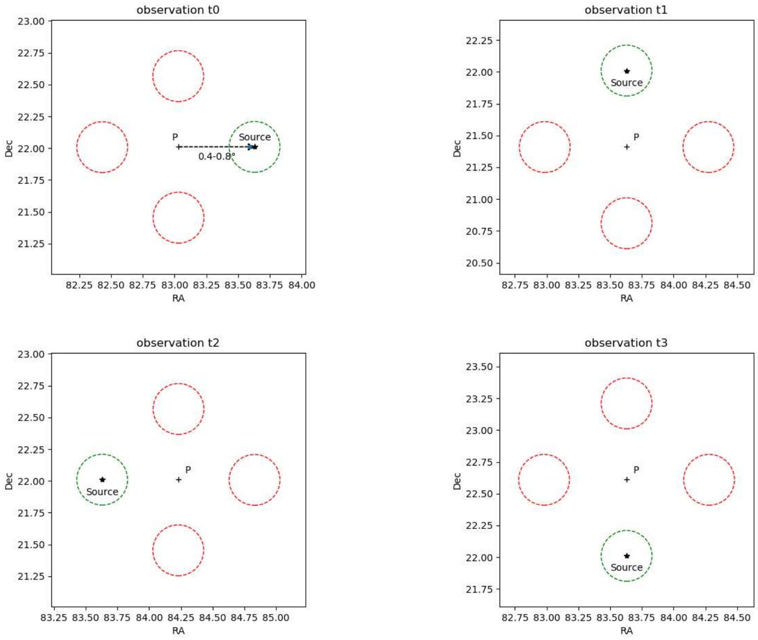

Figure 12: Wobble strategy for LST-1. Every 20 minutes the pointing direction swap by 90° with respect to the source region center, keeping the same distance. The souce region is displayed in green, the off regions are red. The pointing distance is between 0.4° and 0.8°.

3 The `ctools` framework

In this chapter `ctools` are described, the framework provided by Institut de Recherche en Astrophysique et Planétologie (IRAP) for the scientific analysis of CTA high-level data.

3.1 Introducing `ctools`

`ctools` is an open-source software framework developed by J. Knödlseder et al. [27] to perform scientific analysis of astronomical data from Imaging Air Cherenkov Telescopes (IACTs). The `ctools` framework leverages on GammaLib, a powerful and flexible core library written in `C++`. Furthermore, many high-level `ctools` functionalities are wrapped and extended in Python language (i.e. the `cscripts`) to make the user interface easier and providing a better readibility to the not-technical users.

`ctools` provides ready-to-use programs to create and drill down datasets. Information and examples about this framework are available online[15] and documented on published papers as [27].

The software is designed to analyze high-level data after the reconstruction phase (see § 1.2), so the simulated events have no information based on the air Cherenkov shower image characteristics but represent the reconstructed primary photons from source and diffuse background.

The `ctools` framework includes an instrument response functions (IRFs) database, required in many processes to take into account the instrument influence during the observation. The IRFs describe the transformation from physical properties of photons to measured events and for CTA are factorized into effective area, point spread function and energy dispersion as

$$R(p', E', t'|p, E, t) = A_{eff}(p, E, t) \times PSF(p'|p, E, t) \times E_{disp}(E'|p, E, t)\ . \quad (15)$$

The effective area A_{eff} represents the geometric area of the detector multiplied by the detection efficiency in units of cm^2. The PSF factor describes the response of the instrument to a point source. The factor E_{disp} takes into account the difference between the reconstructed event energy and the true photon energy. This energy dispersion effect becomes important at low energy.

Given an incoming primary γ-ray of intensity $I(p, E, t)$ as a function of direction of the true photon p, its energy E and time t, the expected event rate with reconstructed position p', energy E' and time t' is

$$e(p', E', t') = \int R(p', E', t'|p, E, t) \times I(p, E, t)\, dp\, dE\, dt\ . \quad (16)$$

A partial list of `ctools` programs involved in our tests is shortly described below.

---

[15] `http://cta.irap.omp.eu/ctools/index.html` .

ctobssim to simulate photons lists. It generates events that will be analyzed using our data pipelines. The simulations need a model for the astrophysical source and the background with the receiving instrument characteristics. Furthermore the program requires other parameters to describe the observation as location, time and energy boundaries.

ctselect to cut the lists of events in time, energies or positions. It represents a quick tool to reshape the starting dataset.

ctlike determinates the model free parameters (i.e. flux, spectral index, position and more) analyzing binned or unbinned data. This procedure is clearly the `ctools`' "workhorse" module. A significant amount of the workflows goes through the use of `ctlike` program that detects the input type[16] and adapts its analysis to provide a final model[17] containing the best fitting parameters using the maximum likelihood approach.

csphagen is a `ctools` script to extract data cubes[18] from on-source and off-source regions. It provides a set of data as On-Off observation needed to perform the on/off analysis with `ctlike`.

cslightcrv is part of `cscripts`. It computes an observation lightcurve starting from an event list and using a model and `ctlike` for each selected time bin. It can operate in different ways, including "unbinned" and "onoff".

ctskymap is a `ctools` program to generate a sky map from a selected list of events. It is fundamental to decide the pixel-degree scale and the resulting image pixel size. This program can also perform an energy cut and apply a background-subtraction method.

`ctools` provide skymap, spectra, residual analysis and different ways to bin data over many dimensions (usually spatial coordinates, energies and time). Furthermore, the framework allows user to run binned and unbinned likelihood analysis to provide best-fit models as final result.

For unbinned data `ctools` uses the Poisson formula to compute the log-likelihood function:

$$-\ln L(M) = E(M) - \sum_i \ln P(p'_i, E'_i, t'_i|M) \tag{17}$$

where P is the probability density that, given the model M, an event with instrument direction p', measured energy E' and trigger time t' occurs. $E(M)$

---

[16] Many `ctools` programs, including `ctlike`, accept different input as plain event list, counts cube or observation definition XML file.

[17] The model XML file is inspired from the Large Area Telescope aboard NASA's Fermi satellite (*Fermi*-LAT) science tools and it is compatible with it. More info about `ctools` models are provided here `http://cta.irap.omp.eu/gammalib/users/user_manual/modules/model/sky/index.html` .

[18] Data cubes are multi-dimensional matrix filled with data binned in their specific dimensions — typical cases have counts splitted for spatial coordinates and energy bins. In `csphagen` output the data are binned by energy dimension.

is the total number of events predicted, computed integrating the probability density over energies (the energy bounds, Ebounds), contiguous time interval (called Good Time Intervals, GTIs) and region of interest (ROI) as

$$E(M) = \int_{GTI} \int_{Ebounds} \int_{ROI} P(p', E', t'|M) \; dp' dE' dt' \; . \tag{18}$$

For binned data `ctools` computes the likelihood following a Poisson distribution

$$-\ln L(M) = \sum_i e_i(M) - n_i \ln e_i(M) \tag{19}$$

where the i data are taken from binned data. n_i is the observed events in the bin i, and the predicted number of events for model M is

$$e_i(M) = P(p'_i, E'_i, t'_i|M) \times \Omega_i \times \Delta E_i \times \Delta T_i \tag{20}$$

where the probability density P is multiplied by the solid angle Ω_i, the energy ΔE_i and the exposure time ΔT_i.

3.2 The `ctools` reflection method

The `ctools` `csphagen` script can generate the on/off observation using the reflected background algorithm; see § 2.4 for a general description of the reflected background method. The software will use a source region shape and a pointing distance to generate off regions that are "reflected" with respect to the pointing direction, by placing regions of the same source shape[19] at the same offset to the pointing direction, leading to reduced systematic uncertainties in the background determination.

The `csphagen` reflection algorithm implementation considers the on and off regions on the circumference having as radius the distance between pointing and source region center. As shown in Figures 13a and 13b, a larger distance from the target is reflected in a larger number of background regions, and therefore in a different background scaling factor α (see equation 2).

This method is derived by the "wobble mode" pointing and uses all the possible off regions on the circumference skipping only the nearest ones to the source region. Number of regions apart, the method follows the same guideline of false source tracking mode described in § 2.5: an observation session collects on and off counts at the same time and conditions. Furthermore, we will obtain the count excess subtracting averaged background counts from the on source photons.

The reflected regions are used by `csphagen` to provide a fits file in OGIP[20] format with the total counted photons for each energy channel selected. This off count will be used as N_{off} in equation 1 to extimate the probable number of photons from source. The background scaling factor α is also contained for

---

[19] At the moment of writing, only circular regions are supported.

[20] `https://heasarc.gsfc.nasa.gov/docs/heasarc/ofwg/docs/spectra/ogip_92_007/node5.html` .

each energy channel. `csphagen` will not provide a complete on/off observation if the distance between pointing and source is not enough to compute off regions safely — the angular distance is expected to be larger than approx 0.5 degrees. In this particular condition, the program will silently create only an on-source observation.

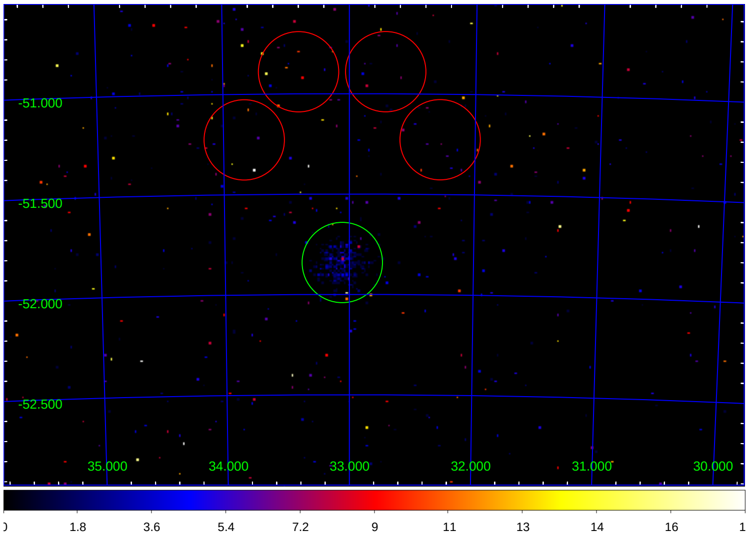

(a) In this skymap the pointing declination is source dec +0.5°.

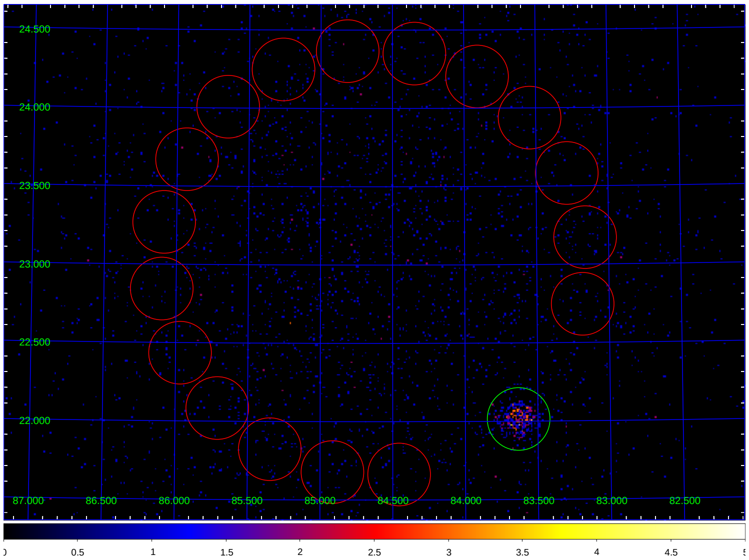

(b) The telescope pointing is +1.0° on RA and Dec shift with respect to source center.

Figure 13: The reflection algorithm draws regions during the Crab simulation. The green region is on source, the red regions are off source. The number of off regions is strictly dependent on the distance between the pointing direction and the source. It is possibile to appreciate the "skipped" regions near the source to avoid spilled counts.

3.3 The on/off analysis with `ctools`

Using `ctools`, a user can perform an on/off analysis, as described in § 2.1, through the `csphagen` program that provides a specific on/off observation as results. Starting with a photons' list, `csphagen` uses a built-in reflection algorithm (§ 3.2) to extract counts from the on-source region and the off regions. The `csphagen` output will be used as `ctlike` input to obtain a best-fit model as final result.

The process can be summarized as follows:

1. events simulations for specific CTA pointing;
2. events selection for each time window;
3. on/off analysis with the `csphagen` tool from `cscripts`;
4. final best-fit model with `ctlike` parameters fitting using the on/off analysis results.

These four steps are now described in detail.

To generate events and analyze the data, `ctools` uses an xml model file. A simple file includes both source and background models factorized in spectral, spatial and also temporal components — for what concerns us the temporal component is skipped because we are mostly interested in spectral evaluation. The spectrum is modelled by a power law characterized by *prefactor*, *index* and *scale*. The spatial model describes position and morphology of the source, showing source type and coordinates (celestial or galactic ones); i.e. the Crab Pulsar is a point source with $RA = 83.6331$ and $DEC = 22.0145$ degrees. Each parameter has a value and a scale factor that will be multiplied by the value to provide the model parameter: typically the scale is chosen so that the value is of the order of 1. Model parameters can be `free` to vary: this is a requirement during the model fitting while it is not relevant in data generation.

The spectral intensity of the power law is used in the spectral model component

$$\frac{dN}{dE} = N_0 \left(\frac{E}{E_0}\right)^{\gamma} \tag{21}$$

where N_0 is the normalization in $\mathrm{ph\,cm^{-2}\,s^{-1}\,MeV^{-1}}$, γ is the spectral index and E_0 the pivot energy in MeV for the XML model.

The instrumental background of CTA is modelled using the background information provided in the instrument response function multiplied by a power law as described in the `CTAIrfBackground` type component. In our model the background powerlaw value is a constant 1 so the IRF background is used with no modifications.

An example of Crab nebula model is the listing 1.

```
<?xml version="1.0" standalone="no"?>
<source_library title="source␣library">
  <source name="Crab" type="PointSource" tscalc="1">
    <spectrum type="PowerLaw">
       <parameter name="Prefactor"   scale="1e-16" value="5.7"
           min="1e-07" max="1000.0" free="1"/>
       <parameter name="Index"       scale="-1"    value="2.48"
           min="0.0"   max="+5.0"   free="0"/>
       <parameter name="PivotEnergy" scale="1e6"   value="0.3"
           min="0.01"  max="1000.0" free="0"/>
    </spectrum>
    <spatialModel type="PointSource">
      <parameter name="RA"  scale="1.0" value="83.6331" min="-360"
          max="360" free="0"/>
      <parameter name="DEC" scale="1.0" value="22.0145" min="-90"
          max="90"  free="0"/>
    </spatialModel>
  </source>
  <source name="CTABackgroundModel" type="CTAIrfBackground"
      instrument="CTA">
    <spectrum type="PowerLaw">
      <parameter name="Prefactor"   scale="1.0"  value="1.0"
          min="1e-3" max="1e+3"   free="1"/>
      <parameter name="Index"       scale="1.0"  value="0.0"
          min="-5.0" max="+5.0"   free="1"/>
      <parameter name="PivotEnergy" scale="1e6"  value="1.0"
          min="0.01" max="1000.0" free="0"/>
    </spectrum>
  </source>
</source_library>
```

Listing 1: An example of Crab model template.

The selection procedure is used to cut the chosen events that will be studied in specific runs: usually we start a full 1800-seconds observation and later we cut it in smaller time windows (i.e. 5 seconds, 10 seconds and so on) in order to test data with a sort-term perspective.

As third step we use the `csphagen` script to derive a set of On/Off observations from the simulated event list. The on information is derived from the on-source region, whereas the off information represents the ensemble of all regions used to sample the background photons. This step is fundamental in this kind of analysis. A pointing offset with respect to the source position is needed to extract photon counts from regions that cover only the source area and to sample the background in the sky map. `csphagen` uses a built-in reflection algorithm (§ 3.2) to locate off regions and estimate counts for the on/off analysis. The script produces count spectra for On and Off regions in OGIP[21] format files, and also relevant information from instrument response functions. The on and off spectral files contain counts, errors and the background scaling information α for every energy channel chosen at run time; all these information will be used in the last step procedure – but were also investigated with customized code for double checks.

---

[21] `https://heasarc.gsfc.nasa.gov/docs/heasarc/ofwg/docs/spectra/ogip_92_007/node5.html` .

The last step uses the `ctlike` program and, as input, the `csphagen` data and source model to compare with the likelihood method. The output will be a new source template with the best-fit values for the free parameters. To instruct `ctlike` to compute the Test Statistic value for a given source, a special attribute `tscalc="1"` must be added to the XML model file.

With the obtained best-fit model, a detection significance estimation is possibile using the test statistic (TS) value defined as

$$TS = 2\left[\ln L(M_s + M_b) - \ln L(M_b)\right] \tag{22}$$

where M_s and M_b represent the model for source and background, $\ln L(M_s{+}M_b)$ is the log-likelihood value obtained when fitting the source and the background together to the data, and $\ln L(M_b)$ is the log-likelihood value obtained when fitting only the background model to the data[22].

For the On/Off observation, `ctools` computes the log-likelihood value as $\ln L = \sum_i \ln L_i$ looping over i energy bins. Each energy bin log-likelihood is:

$$\ln L_i = -N_{on} \ln N_{pred} + N_{pred} - N_{off} \ln N_{bgd} + N_{bgd} \tag{23}$$

with $N_{pred} = N_\gamma + \alpha N_{bgd}$ being the total number of predicted events for energy bin in the on region, N_{bgd} is the predicted number of background events for energy bin in the off region, N_{on} and N_{off} are the number of observed events for energy bin in their respective regions. The number N_{on} and N_{off} are taken from the On and Off spectra, the expected number of γ-ray events N_γ and background events N_{bgd} are computed from the spectral models of the relevant components in the model container (spatial and temporal components are ignored so far).

As a rule of thumb, the square root of the Test Statistic value gives the source detection significance in Gaussian sigmas when the source model degrees of freedom are equal to 1.

---

[22] As explained in § 2.2 and in `ctools` documentation, TS follows a χ^2_n distribution with n degrees of freedom, where n is the number of free parameters in the source model component.

4 Short-term detection with on/off analysis

In this chapter is presented a preliminary on/off analysis obtained targeting a Crab-like source, empty fields and a GRB afterglow. These results are mainly carried out using the `ctools` framework described previously and the aperture photometry technique. The goals are multiple: to check the detection significance reliability at observation times of less than 30 minutes, to estimate the false alarm probability, and to test the software limits or inconsistencies.

4.1 Crab-like simulations

We run our first tests simulating a stable γ-rays emitter point-source model with a Crab-like spectral component. The Crab Nebula is a supernova remnant containing a spinning neutron star emitting radiation from γ-rays to radio waves. It is the brightest source in the γ-ray sky and can be considered a steady standard candel at very high energies[23].

This first set of simulations was performed using the full southern array through `South_z20_0.5h` fits from `Prod3b-v2` database IRF[24], a pointing direction shift of +0.5 degrees in declination with respect to the source position (this is a requirement to trigger the `ctools` reflection algorithm – see also §3.2), and ten logarithmically defined energy bins for `csphagen` analysis on a full energy range between 25 GeV and 150 TeV. Furthermore, the radius of the chosen region to extract on and off counts was set arbitrarily to 0.2°[25].
The on/off observation list generated by `csphagen` program is used to perform the Maximum Likelihood Estimation (MLE) of free parameters in the model to fit. `ctlike` program compares the on/off observation data and a Crab model[26] with one degree of freedom — only the spectral prefactor component is a free parameter, the index is fixed to -2.48 value — to obtain a best-fit model from which to extract the test statistic (TS) value to evaluate the detection significance and the flux.
Simultaneously with this `ctools` processing, the detection significance is computed with the Li and Ma formula 12.
To evaluate the detection limit in the RTA perspective, each simulation was cut in different time windows: starting from the longest duration of 1800 seconds, decreasing time by step down to on observation time of 1 second.

The detection significances resulting from 10000 simulations are shown in Table 3.

Assuming a detection if $S \geq 5\sigma \sim \sqrt{TS}$, we can consider as detected a Crab-like source with a 3 seconds lasting observation. In Figure 14 the TS dis-

---

[23] This claim is questioned due to the discovery of γ flares `https://sci.esa.int/s/w7Vv3MA`, but Crab remains a typical reference for many tests.

[24] `https://www.cta-observatory.org/science/cta-performance` .

[25] Checking the IRFs' Point Spread Function we noticed that the 0.2 degrees radius is sufficient to contain 99.73% of the PSF at energies $\geq$ 300 GeV.

[26] The Crab nebula model has only a spectral and a spatial component, as described above in listing 1.

	`ctools` MLE		Li & Ma		MLE (1 en.bin)
secs	TS	$\sqrt{TS}$	Significance	σ/S	$\sqrt{TS}_{e1}$
1800	15642.39 ± 277.64	125.06 ± 1.11	110.52 ± 1.10	0.01	110.50 ± 1.09
600	5214.70 ± 159.00	72.20 ± 1.10	63.80 ± 1.08	0.02	63.78 ± 1.11
100	870.09 ± 65.94	29.48 ± 1.12	26.05 ± 1.11	0.04	26.02 ± 1.11
60	522.52 ± 51.21	22.83 ± 1.12	20.17 ± 1.11	0.05	20.14 ± 1.11
30	262.64 ± 36.32	16.17 ± 1.12	14.28 ± 1.10	0.08	14.26 ± 1.11
20	175.49 ± 29.58	13.20 ± 1.12	11.66 ± 1.10	0.09	11.64 ± 1.12
10	88.17 ± 20.77	9.32 ± 1.11	8.23 ± 1.09	0.13	8.20 ± 1.10
5	44.69 ± 14.90	6.59 ± 1.13	5.81 ± 1.10	0.19	5.80 ± 1.12
4	35.97 ± 13.31	5.89 ± 1.13	5.18 ± 1.10	0.21	5.16 ± 1.13
3	27.26 ± 11.52	5.10 ± 1.13	4.49 ± 1.10	0.24	4.48 ± 1.12
2	18.57 ± 9.60	4.15 ± 1.16	3.65 ± 1.11	0.30	3.65 ± 1.12
1	9.96 ± 6.85	2.94 ± 1.16	2.57 ± 1.10	0.43	2.59 ± 1.11

Table 3: `csphagen` and `ctlike` run on 10K simulated Crab-like source spectra. The `ctools` likelihood analysis provides the TS; we add a significance as $S \sim \sqrt{TS}$. The fourth and fifth columns represent the Li & Ma significance and relative error. The last column shows the significance values when `ctools` configuration uses only 1 energy bin in the on/off analysis. Pointing at $dec_{source}\ +0.5°$, E_{min} 25 GeV, E_{max} 150.0 TeV.

tributions for shorter time intervals are compared. A similar observation time limit can be deduced also from the detection significance computed with Li and Ma formula. The significance values obtained with two independent computations are similar, but the likelihood method performs better. The discrepancy is explained with the energy binning involved in maximum likelihood estimation: as stated above, the `csphagen` command has been run binning energy dimension in 10 intervals. In the presence of enough events in energy bin, the effect is to increase the TS value with respect to analysis performed with a low number of energy bin. Li and Ma significance integrates counts over the full energy range, therefore it is computed as if it were a single energy bin. Some simple tests have shown that the TS improves more markedly from a few energy bins to ten rather than going from 10 to higher energy bin numbers (i.e. 50). To verify the energy bin claim, other likelihood simulations have been run with a single energy bin configurated. The results are in the last column of Table 3: the significance is quite similar to the Li and Ma. The significance comparison is shown in Figure 15.

Unlike the `ctools` on/off likelihood method, the Li and Ma significance is subject to the constraint of “not too few counts” (i.e. ≥ 10) in on source and off source regions (§ 2.3). Table 4 summarizes the on and off counts obtained with aperture photometry and the excess computed with equation 1.
The data in Table 4 confirm that a Crab-like source observed for 1 second does not provide enough photons in on and off regions to consider the detection significance reliable. Indeed, the counts are fewer than 10, the suggested threshold in [4]. In Figure 16 it is possible to notice that the N_{on} and N_{off} photons counts remain above the Li and Ma events threshold of 10 and they also maintain a

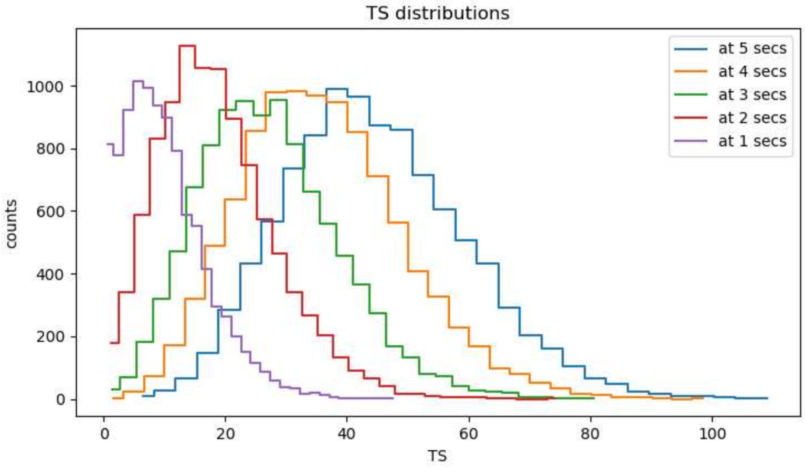

Figure 14: The TS distributions for periods in the range 1–5 seconds. Notice the shift to the left due to the increasingly worse TS at shorter time.

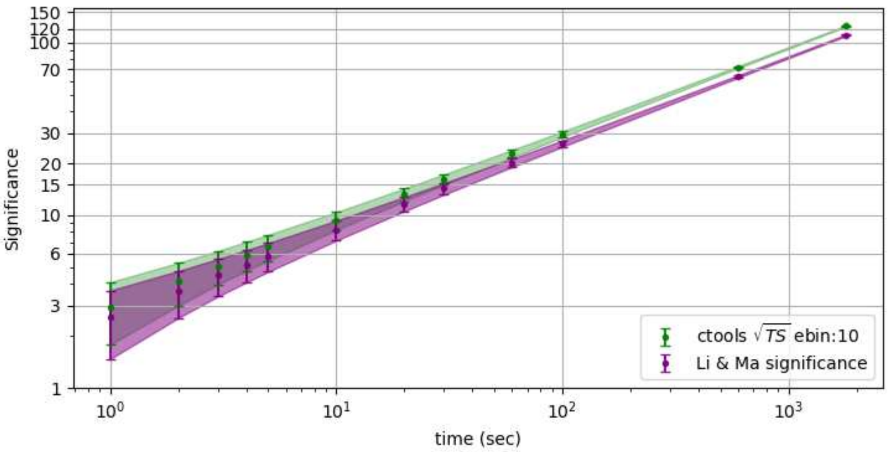

Figure 15: Comparison of the detection significance using `ctools` on/off analysis with MLE and photometric analysis adopting the Li and Ma formula. In purple the significance computed with Li and Ma formula is shown. The green color was chosen to display the `ctools` significance as $\sqrt{TS}$ obtained with a 10 energy bins on/off analysis.

Gaussian profile for short time as 2 seconds (lower panel).

Considering the on source and background counts at 1 seconds, it is also possible to analyze the TS provided by `ctools` MLE in Table 3. Although

secs	N_{on}	N_{off}	N_{exc}
1800	11929.10 ± 109.74	10376.07 ± 101.39	9335.08 ± 112.64
600	3976.01 ± 62.19	3458.90 ± 59.48	3111.28 ± 63.93
100	662.83 ± 26.04	576.67 ± 24.19	518.66 ± 26.76
60	397.55 ± 20.16	345.90 ± 18.60	311.07 ± 20.72
30	199.04 ± 14.20	172.91 ± 13.10	155.81 ± 14.59
20	132.65 ± 11.58	115.12 ± 10.67	103.87 ± 11.89
10	66.25 ± 8.17	57.59 ± 7.51	51.85 ± 8.36
5	33.11 ± 5.81	28.77 ± 5.29	25.91 ± 5.96
4	26.46 ± 5.21	23.03 ± 4.75	20.71 ± 5.34
3	19.85 ± 4.49	17.25 ± 4.10	15.54 ± 4.59
2	13.23 ± 3.68	11.52 ± 3.36	10.35 ± 3.78
1	† 6.64 ± 2.58	† 5.76 ± 2.39	† 5.20 ± 2.64

Table 4: The on source and off source counts obtained applying photometric approach on 10K simulation of the Crab-like source. The simulating environment is the same as in Table 3. The α factor is 0.25 because we are generating the same four regions of `ctools` reflection algorithm (ref. §3.2).
†: The number of counts is very limited ($n < 10$), so the Li and Ma detection significance is not reliable.

the best-fit model provides an apparently acceptable significance, checking the TS relative error can highlight an issue in short time intervals. In our tests, the standard deviation of TS for 1 and 2 seconds is over the 50% of the TS value. Therefore, we can suggest as a good practice to consider the results from `ctools` on/off analysis reliable when $TS > 25$.

Considering the limits described above, we can deduce that the `ctools` significance show better values than Li and Ma significance, but it requires a higher threshold to be accepted.

In addition to the data described above, we produced other information in the attempt of investigating the `ctools` from multiple energy perspectives.

In section A.3, I reported extra data generated selecting events in different energy ranges. The data are generated with the same on/off procedures used in the test described in this section. These results have allowed us to compare the `ctools`'s TS with the Li & Ma significance, taking also into account the photon counts from on and off source regions.

The extra data were generated following two distinct ways. The first strategy consists in decreasing the energy interval while keeping the high-energy bound fixed to 150.0 TeV. Other extra data were selected with five logarithmic steps for energy decade intervals between 25 GeV and 800 GeV.

In either narrow energy bins or more energetic energy bins it is possible to appreciate the progressive drop in the background counts; this means that longer exposures are needed to meet the Li & Ma “few counts” requirements described in §2.3 (i.e. 100 seconds when above 650 GeV).

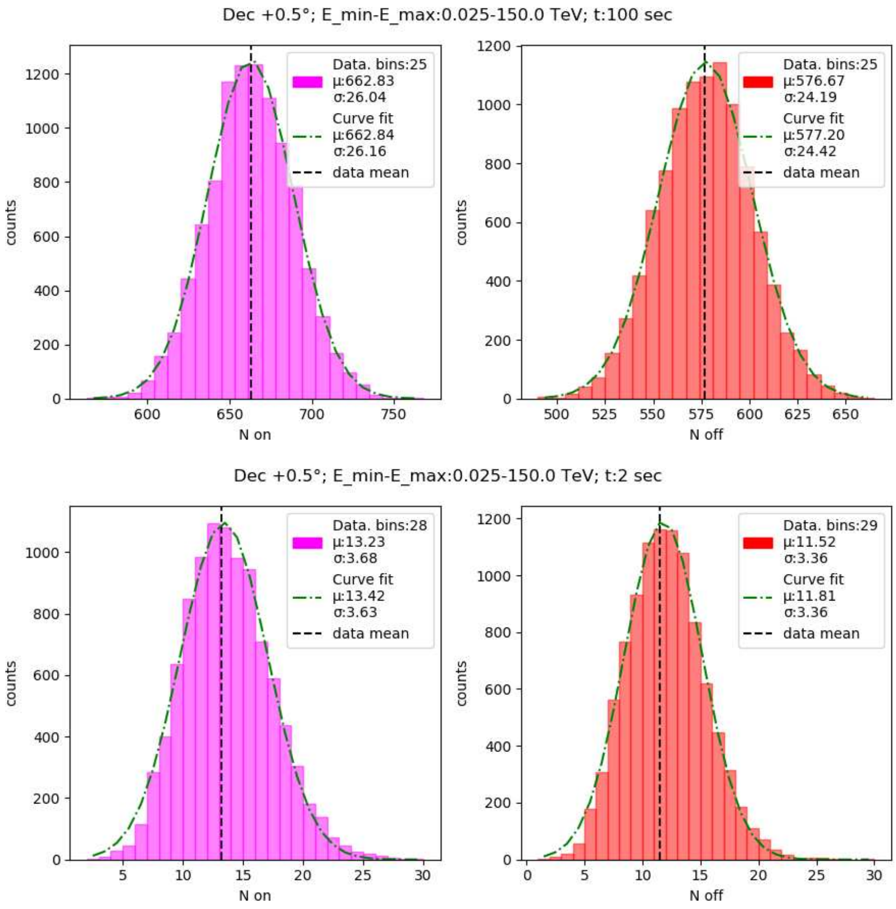

Figure 16: The on and off counts distributions at 100 and 2 seconds (top and bottom panels) for 25 GeV–150 TeV energy range; we note that the Gaussian shapes are preserved.

Fitting the relative error $\sigma/significance$ as function of the simulated time with a power law (or a broken power law for smaller energy bins) as:

$$\frac{\sigma}{significance} = A \cdot time^{k} \tag{24}$$

we have been able to derive the Li and Ma error at any given time.
A couple of examples are shown in Figure 17.
These fitted parameters led to a more in-depth analysis of the uncertainties relating to CTA's integral and differential sensitivity. As we can see in Figure 18, below 10 seconds we achieve a really good sensitivity but the uncertainties increase enormously, invalidating potential observations.

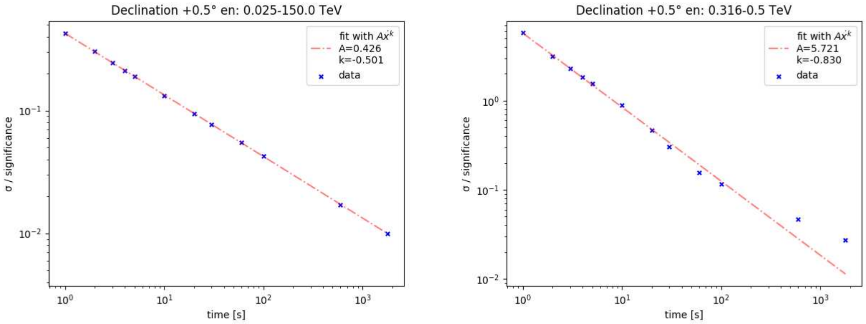

Figure 17: The significance relative error data vs powerlaw fit per simulated time in two different energy ranges (left: 25 GeV–150 TeV, right: 316 GeV–500 GeV). The fitting parameters are shown in the legend.

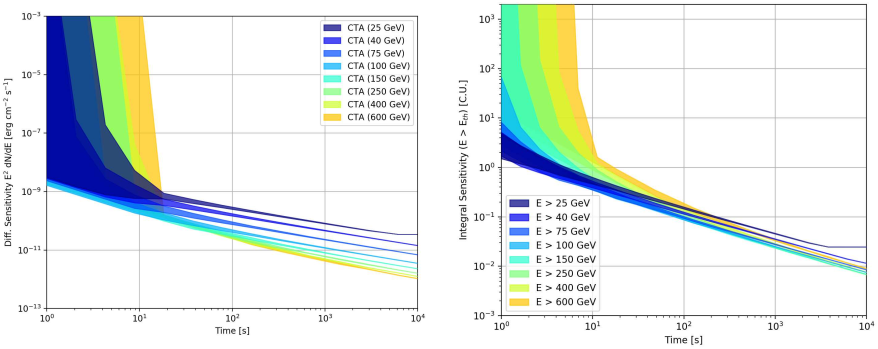

Figure 18: Differential (left) and integral sensitivity (right) as function of time with errors. Credits: V. Fioretti, October 2019 CTA Consortium Meeting. Data for these plots are based on South z20 IRFs.

4.2 Empty-field simulations

To evaluate the reliability of the detected sources in short-time analysis, we run simulations using empty fields.

The empty field was simulated 500 thousand times with a +0.5° declination shift between pointing and source coordinates; the energy range covers the CTA full array configuration (i.e. 25 GeV to 150 TeV); the `csphagen` tool was set to perform an on/off observation with 10 logarithmic separated energy bins and a source region radius of 0.2° degree. The time intervals are the same used in 4.1, from 1800 seconds to 1 second. The `ctlike` maximum likelihood estimation (MLE) provides the TS for each best-fit model. `ctlike` can return negative TS values when the maximum likelihood optimisation of model free parameter is not able to find enough excess count to discriminate the background from source.

From Wilks' theorem (see section 2.2), TS is expected to be asymptotically distributed as χ^2_1 when the null hypothesis is true, as in this empty-field case. Indeed, the data show that TS > 0 is actually distributed as $\chi^2_1/2$. The factor 1/2 is due to the fact that negative TS depends on not allowed negative flux, so about one half of statistical fluctuations goes in TS $= 0$ and are considered as such. Some examples of TS data obtained from the simulations are shown in Figure 19 and 20.

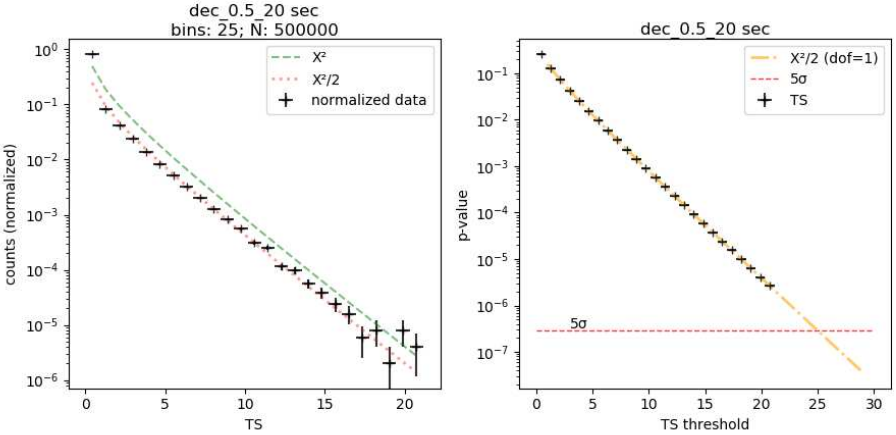

Figure 19: The empty field TS distribution for 20 seconds (left) and its relative p-value distribution with 5σ threshold (right). N is the number of samples used for these simulations, and TS values are binned in 25 intervals. We expect that the data follow a $\chi^2_1/2$ distribution excluding the $TS = 0$ counts, that aggregate the not positive TS and are responsible for the 1/2 factor.

As we can see, the data follow the $\chi^2_1/2$ trend, as expected. This consideration is valid for all the TS distributions from short time simulations, but the trend diverges when time grows – i.e. at 1800 seconds – for reasons that should be

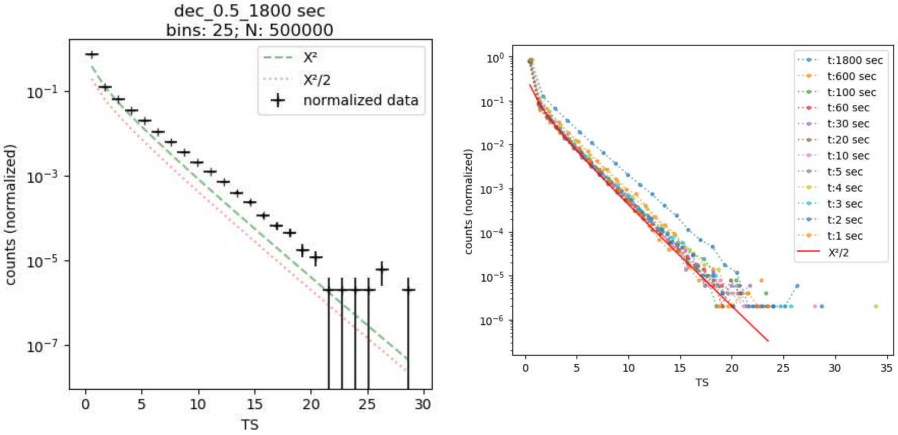

Figure 20: Left: the empty field TS distribution for 1800 seconds simulations diverges from χ^2_1. Right: all the TS in the same plot. In both plots, we can see that the 1800's TS is clearly far away from $\chi^2_1/2$ which is the distribution the data should follow according to Wilks' theorem (§2.2).

further investigated.

The probability that a source is identified in an empty fields with a $TS \geq h$ is called p-value and is calculated as:

$$P(TS \geq h) = \int_h^{+\infty} p(x)dx \ . \tag{25}$$

In this case $p(x)$ is the $\chi^2_1/2$ distribution and in Figure 19 (on the right) we can see the 5σ p-value for a TS $\geq$ 25 threshold.

With this result we deduce our `ctools` process is reliable for analysis in short-time and we can give a TS threshold to our experiments at the desired σ.

4.3 Short GRB afterglow

The POSyTIVE project[27] has the purpose to make realistic predictions for the detection rates of GRBs with CTA. The project analyzed the 40-year dataset of multi-wavelength GRB observations (short and long) in order to provide spectral information useful to create emission models of prompt and afterglow radiation. To simulate afterglow emission, the POSyTIVE project considered a synchrotron and synchrotron-self Compton (SSC) radiation from electrons accelerated by a forward shock caused by the interaction between a relativistic blastwave and the surrounding medium, following the method developed by L. Nava et al. in [23].

---

[27] The POpulation Synthesis Theory Integrated project for very high energy emission.

From an operational point of view, the spectral template provides a fits file from which we can extract an energy range-spectral model for each considered "time slice". `ctools` allows the elaboration of composed spectral model and simulate emitters following all the spectral models involved in the right time interval.

We simulated the detectability of a short GRB afterglow thanks to the spectral template – `run0406 ID000126` – provided by L. Nava and POSyTIVE project. This template provides the electromagnetic counterpart of a neutron stars merger from the GW COSMoS database[28].

The two thousand simulations were performed using the `prod3b-v2 South_z40_0.5h` IRF, with a maximum exposure time of 100 seconds and one degree of freedom powerlaw spectral model. The energy range is the full span 25 GeV–150 TeV and only one energy bin was used during the on/off analysis. Different times were selected, from 100 seconds to 1 second.

The `ctools` MLE analysis results are in Table 5. Assuming a 5σ significance, we consider valid detections only when $\mathrm{TS} \geq 25$ (see § 4.2).

secs	TS	TS rel. err.	$\sqrt{TS}$	Flux $[\mathrm{ph\,cm^{-2}\,s^{-1}}]$
100	1860.10 ± 169.33	0.09	43.08 ± 1.96	$8.6 \times 10^{-9} \pm 4.4 \times 10^{-10}$
60	1001.87 ± 123.87	0.12	31.59 ± 1.96	$8.0 \times 10^{-9} \pm 5.4 \times 10^{-10}$
30	306.45 ± 69.78	0.23	17.39 ± 1.99	$5.6 \times 10^{-9} \pm 6.9 \times 10^{-10}$
20	95.36 ± 41.61	0.44	9.53 ± 2.11	$3.3 \times 10^{-9} \pm 7.8 \times 10^{-10}$
10	4.25 ± 9.84	2.32	1.14 ± 1.72	-
5	3.40 ± 8.36	2.46	0.94 ± 1.59	-
4	3.33 ± 8.29	2.49	0.92 ± 1.58	-
3	3.43 ± 8.79	2.56	0.90 ± 1.62	-
2	3.00 ± 7.96	2.65	0.79 ± 1.54	-
1	2.27 ± 6.67	2.94	0.59 ± 1.38	-

Table 5: `csphagen` and `ctlike` run on 2000 simulated GRB afterglow source. The runs provide TS and flux; we add a significance as $\sigma \sim \sqrt{TS}$ and relative error on TS. The detection significance is too low for data with $t \leq 10$ seconds.

Comparing the results obtained from photometric approach, showed in Table 6, we can confirm what we observed in the previous table with MLE analysis: in shorter time interval the counts drop provides a negative excess count and useless relative significance. The negative excess count is a non-sense value: in the simulations the on-source region has a so weak signal with respect to background, that the background exceed the source itself. Indeed, for time below the 10 seconds we have no enough counts in on-source region to meet the Li and Ma requirements. See Figure 21.

Although in 10 seconds time interval the on and off counts meet the Li and Ma conditions, the detection significance has a large relative error and does not

---

[28] GW COSMoS – Gravitational Wave Compact binary system – is a database of simulated NS-NS merger from B. Patricelli et al. [30].

secs	N_{on}	N_{off}	N_{exc}	Significance
100	1163.78 ± 49.42	542.21 ± 63.72	1028.23 ± 51.91	43.09 ± 1.96
60	650.32 ± 36.88	325.26 ± 49.74	569.00 ± 38.76	31.60 ± 1.96
30	239.76 ± 23.05	162.82 ± 35.19	199.06 ± 24.60	17.39 ± 1.99
20	104.85 ± 17.09	108.49 ± 28.69	77.73 ± 18.53	9.54 ± 2.11
10	14.74 ± 10.19	54.29 ± 20.81	1.17 ± 11.59	1.14 ± 1.72
5	6.56 ± 6.94	27.28 ± 14.68	-0.26 ± 7.97	0.93 ± 1.58
4	5.21 ± 6.17	21.88 ± 13.17	-0.26 ± 7.11	0.89 ± 1.56
3	3.89 ± 5.39	16.43 ± 11.53	-0.22 ± 6.22	0.77 ± 1.47
2	2.58 ± 4.24	11.02 ± 9.08	-0.17 ± 4.89	0.64 ± 1.37
1	1.28 ± 2.85	5.62 ± 6.11	-0.13 ± 3.29	0.30 ± 0.93

Table 6: The photon counts for 2000 simulated GRB afterglow sources. The Li & Ma significance is in the last column.

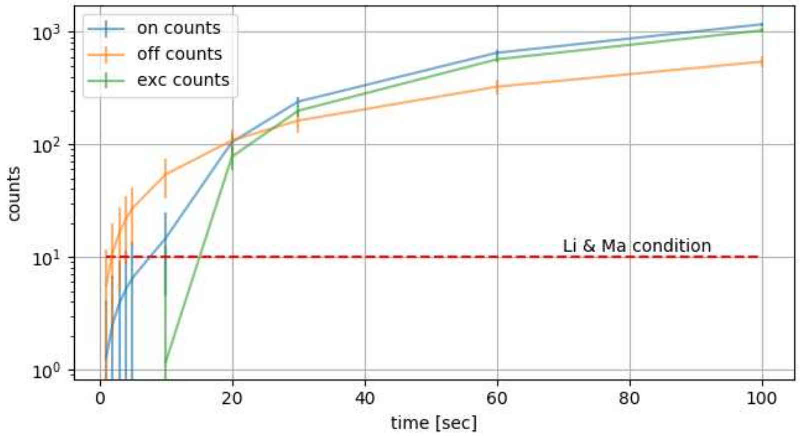

Figure 21: The GRB afterglow counts in on source, off regions and computed excess counts. No EBL absorption.

reach an acceptable level of significance, so the GRB afterglow signal is not detected at 10 seconds.

Additional simulations were run using the same GRB template with the spectral information affected by the Extragalactic background light (EBL)[29]. High-energy γ-rays interact with EBL photons in electron-positron pair production interactions removing γ-rays from view and altering the observed spectra of extragalactic high-energy sources. The resulting attenuation follows the Gilmore model described in [17]; the effect is perceptible above 10 GeV and becomes noticeable around a few hundred GeVs (see Figure 22).

---

[29] The EBL is the entire light emitted by stars, galaxies and AGN over the full lifetime of

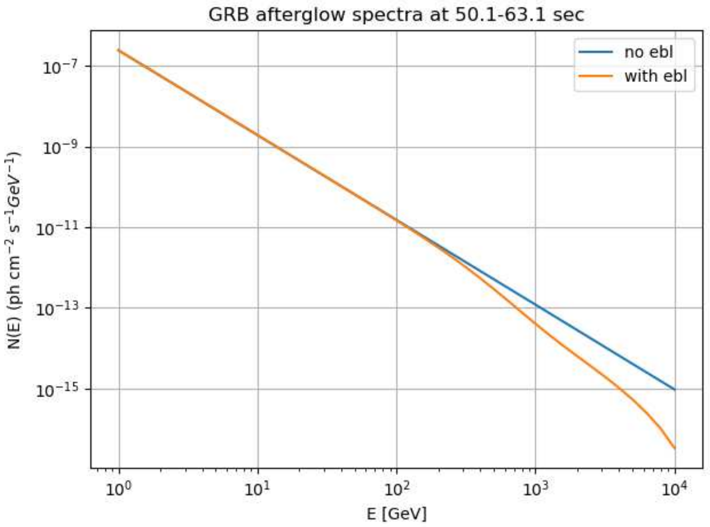

Figure 22: The GRB afterglow template spectrum at 50-63 seconds. Comparison with and without EBL.

In Tables 7 and 8 we can see how the EBL attenuation removes photons from the on source region; see also Figure 23. Comparing these data with those no-EBL previously listed, TS and flux drop but the GRB is detected in 20 seconds or longer observations. Below the 10 seconds threshold, the signal cannot be taken into consideration.

secs	TS	TS rel. err.	$\sqrt{TS}$	Flux [ph cm^{-2} s^{-1}]
100	975.08 ± 129.37	0.13	31.16 ± 2.07	$5.4 \times 10^{-9} \pm 4.0 \times 10^{-10}$
60	523.29 ± 94.33	0.18	22.78 ± 2.06	$5.0 \times 10^{-9} \pm 4.9 \times 10^{-10}$
30	156.71 ± 53.52	0.34	12.34 ± 2.12	$3.5 \times 10^{-9} \pm 6.5 \times 10^{-10}$
20	48.49 ± 31.74	0.65	6.59 ± 2.25	$2.1 \times 10^{-9} \pm 7.5 \times 10^{-10}$
10	4.03 ± 9.57	2.37	1.08 ± 1.69	-
5	3.40 ± 8.36	2.46	0.94 ± 1.59	-
4	3.33 ± 8.29	2.49	0.92 ± 1.58	-
3	3.43 ± 8.79	2.56	0.90 ± 1.62	-
2	3.00 ± 7.96	2.65	0.79 ± 1.54	-
1	2.27 ± 6.67	2.94	0.59 ± 1.38	-

Table 7: `ctools` MLE analysis on 2000 simulated GRB afterglow source affected by EBL (Gilmore's model). The runs provide TS and flux; we add a significance as $\sigma \sim \sqrt{TS}$ and relative error on TS. The data at 10 seconds and downwards are invalid.

---

the Universe, strongly altered by the redshift due the Universe expansion.

secs	N_{on}	N_{off}	N_{exc}	Significance
100	783.37 ± 44.56	542.32 ± 64.21	647.79 ± 47.25	31.16 ± 2.07
60	440.07 ± 33.02	325.27 ± 50.15	358.75 ± 35.19	22.79 ± 2.06
30	166.16 ± 21.35	162.82 ± 35.40	125.46 ± 23.16	12.34 ± 2.12
20	76.13 ± 16.18	108.49 ± 28.82	49.01 ± 17.86	6.59 ± 2.25
10	14.24 ± 10.17	54.30 ± 20.81	0.66 ± 11.57	1.08 ± 1.69
5	6.56 ± 6.94	27.28 ± 14.68	-0.26 ± 7.97	0.93 ± 1.58
4	5.21 ± 6.17	21.88 ± 13.17	-0.26 ± 7.11	0.89 ± 1.56
3	3.89 ± 5.39	16.43 ± 11.53	-0.22 ± 6.22	0.77 ± 1.47
2	2.58 ± 4.24	11.02 ± 9.08	-0.17 ± 4.89	0.64 ± 1.37
1	1.28 ± 2.85	5.62 ± 6.11	-0.13 ± 3.29	0.30 ± 0.93

Table 8: The photon counts for 2K simulated GRB afterglow sources with EBL attenuation. The background counts N_{off} are the same as in Table 6.

This run of simulations is not completely satisfactory. No delay was introduced to simulate the response to a transient alert (inter-systems communications, slewing time, etc.), and this change surely the observed measurements in short time intervals. Since the afterglow of the GRB develops over time, analyzing it not in the very first seconds is expected to change the counts in on source region, therefore the detection significance. It is plausibile that the counts in on source region with EBL and without it, are pretty similar (or the same for very short time interval, indeed) due to the combination of low statistics for short time and high number of low energy events which are more likely.

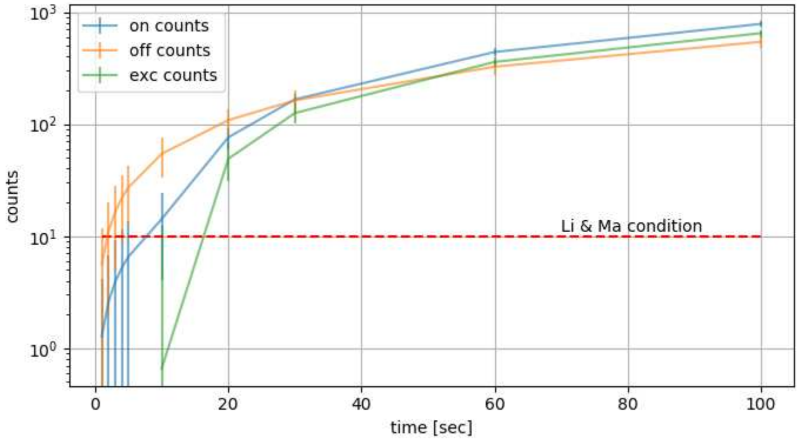

Figure 23: The GRB afterglow with EBL counts in on source, off regions and computed excess counts. Because of the EBL absorption the on-source (blue) and excess counts (green) lose photons and their values get closer to the off-source counts (orange).

According to these results, we can conclude that to detect an afterglow flux of similar intensity to the one tested here we will need to gather photons for about 20 seconds with our GRB and EBL models. As expected, the aperture photometry approach has exactly the same detection significance as maximum likelihood estimation from `ctools` if a single energy bin is used to process the on/off data with `csphagen`.

5 A new procedure for aperture photometry for γ-rays

Using the aperture photometry python code written to check the `ctools` results, we decided to extend it and improve the Real-Time Analysis pipeline. In this chapter I will explain the software library that applies the photometry approach to the reconstructed γ photon list to evaluate the γ-ray source detection and estimate the source flux. The working context simulates observations performed with the Large sized-telescope (LST-1) built in La Palma in 2018, with its specific wobbling pointing strategy in four steps, swapping the direction every 20 minutes as described in section 2.5. The RTA photometric approach will be applied to empty-field simulations, a Crab-like source observation and a short GRB afterglow analysis.

5.1 The aperture photometry in the RTA pipeline

As described in § 1.5, the Real-Time Analysis (RTA) is a complex system to provide fast alerts on variable and transient sources [21]. A specific software, the RTA pipeline, takes care of the search and evaluation of transient phenomena in multiple timescales and defined regions or elsewhere in the field of view.

The software I wrote was designed to evaluate a transient detection after a previous localization with an aperture photometry approach. Furthermore, the software will also provide a flux estimation of the observation target.

5.1.1 Counting photons with Photometrics class

Starting from a simulated events list, the software filters and counts the events in different on source regions and in background regions selected following reflection algorithms as explained in § 2.1. The detection significance of the observation is evaluated with Li and Ma formula (§ 2.3).

It is important to pick the "right" size for the region radius: it has to be large enough to take all the source emitted photons but not too large to include other sources in the same area. To measure the effective γ-ray source flux, it is needed to count the photons in on-source region and subtract the diffuse background counts: the estimated signal from the source is given from equation 1.

The `Photometrics` class was written to generate the useful regions to count photons from an events list. The regions are generated on the radius vector from pointing and source region center. The counter method selects all the events in events list lying inside the input region as shown in Listing 2[30] and Listing 3.

---

[30] A synopsis with more options is shown in Listing 9 in A.2.1.

```
from lib.photometry import Photometrics

phm = Photometrics({ ’events_list’: events_list })

on_count = phm.region_counter(src_coords, radius)

off_regions = phm.cross_regions(pnt_coords, src_coords, radius)

off_count = 0
for region in off_regions:
    off_count += phm.region_counter(region, radius)
```

Listing 2: The call to photometric code to extract on and off counts.

```
def region_counter(self, input_center, input_radius, emin=None,
    emax=None):
   """Counts photons in an input area"""
   region_center = utils.get_skycoord(input_center)
   region_radius = utils.get_angle(input_radius)

   # filtering...
   condlist = np.full(len(self.events_data.field(’ENERGY’)), True)
   # ... w/ energy boundaries
   if emin is not None:
       condlist &= self.events_data.field(’ENERGY’) >= emin
   if emax is not None:
       condlist &= self.events_data.field(’ENERGY’) <= emax

   events_list = np.extract(condlist, self.events_data)
   # events coordinates from the selected events list
   events_coords = SkyCoord(events_list.field(’RA’),
       events_list.field(’DEC’), unit=’deg’, frame=’icrs’)
   distances = region_center.separation(events_coords)
   return np.count_nonzero(distances < region_radius)
```

Listing 3: Counting photons with photometric code.

Two methods have been implemeted to compute the off regions. The first one, Listing 4, computes 3 regions at 90° of distance from the source center, on the circumference with radius equal to pointing-source angular distance. The second one, Listing 5, computes a variable number of off regions at minimum distance each other[31].

---

[31] This method should become a generalization of the previously described Listing 4 method.

```
@classmethod
def cross_regions(cls, input_pointing_center, input_region_center,
    input_region_radius):
    """Return the three background regions starting from pointing
        and source one.

    Parameters
    ----------
    input_pointing_center: SkyCoord or dict
    input_region_center: SkyCoord or dict
    input_region_radius: Angle or float

    Returns
    -------
    array of regions
    """
    # FIXME this algorithm has no check about distance and region
        radius.
    pointing_center = utils.get_skycoord(input_pointing_center)
    region_center = utils.get_skycoord(input_region_center)
    region_radius = utils.get_angle(input_region_radius)
    radius = pointing_center.separation(region_center)
    starting_pos_angle =
        pointing_center.position_angle(region_center)
    regions = []
    for i in range(1,4):
        theta = starting_pos_angle + i * Angle(90, unit=’deg’)
        coord_pos = pointing_center.directional_offset_by(theta,
            radius)
        regions.append({ ’ra’: coord_pos.ra.deg, ’dec’:
            coord_pos.dec.deg, ’rad’: region_radius.deg })
    return regions
```

Listing 4: Method to compute three cross background regions as in LST-1 wobble pointing mode.

```
@classmethod
def reflected_regions(cls, input_pointing_center,
    input_region_center, input_region_radius):
    """Find regions with reflected algorithm.

    Parameters
    ----------
    input_pointing_center: SkyCoord or dict
    input_region_center: SkyCoord or dict
    input_region_radius: Angle or float

    Returns
    -------
    array of regions
    """
    pointing_center = utils.get_skycoord(input_pointing_center)
    region_center = utils.get_skycoord(input_region_center)
    region_radius = utils.get_angle(input_region_radius)

    # Angular separation of reflected regions. 1.05 factor is to
        have a margin
    region_diameter = 1.05 * 2.0 * region_radius
    radius = pointing_center.separation(region_center)
    numbers_of_region_centers = int(2 * np.pi * radius /
        region_diameter)
    if numbers_of_regions_centers < 4:
        raise Exception(’the␣combination␣of␣region␣radius␣and␣
            coordinates␣does␣not␣allow␣to␣compute␣reflected␣
            regions.’)
    regions_offset_angle = Angle(360, unit=’deg’) /
        numbers_of_regions_centers

    regions = []
    # starting from the source region 0, we skip region 1 and
        region N, so 2..N-1
    starting_pos_angle =
        pointing_center.position_angle(region_center)
    for i in range(2, numbers_of_regions_centers-1):
        theta = starting_pos_angle + i * regions_offset_angle
        coord_pos = pointing_center.directional_offset_by(theta,
            radius)
        regions.append({ ’ra’: coord_pos.ra.deg, ’dec’:
            coord_pos.dec.deg, ’rad’: region_radius.deg })
    return regions
```

Listing 5: Method to compute full reflected background regions. On a circumference with a radius given by pointing-source angular distance, this method computes all the possible off regions skipping the two near the on-source region.

5.1.2 The effective area computation

When the incoming electromagnetic radiation is detected by CTA mirrors, a small number of photons with a wide range of energies must be taken into consideration in the following data analysis.

The spectral flux density $F(\nu)$ [$\mathrm{erg\,cm^{-2}\,s^{-1}\,Hz^{-1}}$] is the quantity that describes the rate at which energy is transferred by electromagnetic radiation through a surface, per unit surface area and at a given frequency ν. The surface receiving the radiation is the cross-sectional area A [cm^2] of the detector that points towards the source. The effective area is the geometric area where photons are collected, multiplied by an efficiency term composed by several factors. In the case of Cherenkov telescopes, these factors are bound to the efficiency of the collecting mirrors, the efficiency of the detector and the ability to reconstruct the primary photons. The CTA full telescope array has a specific effective area to detect photons of different energies, as shown in the Figure 24. Also the angular distance θ of the observed object from the optimal on-axis pointing plays a role in the definition of effective area.

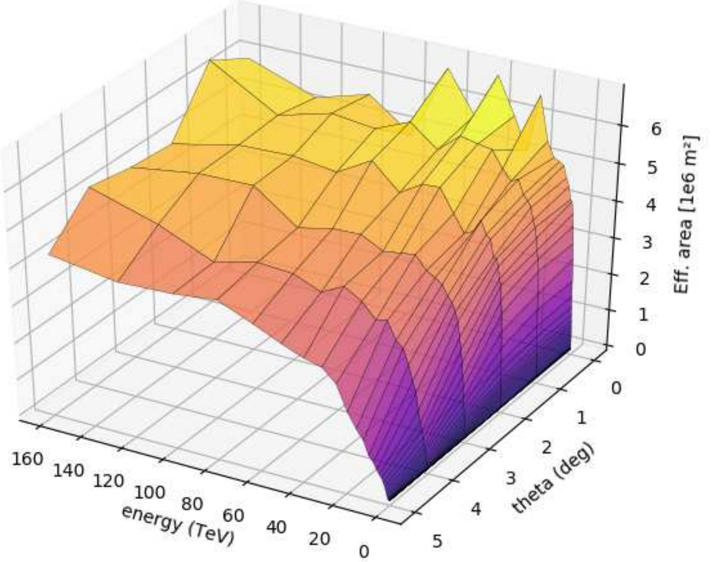

Figure 24: The effective area values from prod3b-v2 South_z40_avg_0.5h public IRF. The plot shows that CTA has a higher effective area in the high-energy range, and a slow degradation with respect to the pointing-source angle.

Therefore, the effective area $A_{eff}(\theta, E_\gamma)$ depends on the energy of incoming photons and the pointing direction[32]. To compute the γ-ray source flux we need to integrate on energy the differential flux as stated in

$$\Phi(E) = \frac{dF}{dE}(E) = \frac{dN_\gamma}{dE\ dA_{eff}\ dt_{eff}} \tag{26}$$

---

[32] From a general point of view, also other specific observational conditions (as weather, zenith and azimuth angle, etc.) can influence the efficiency parameter, therefore IRFs should be attached to each real observation and provide values to take these parameters into account.

where dN_γ is the number of excess events in dE energy, A_{eff} is the Effective Area in the chosen source region and t_{eff} is the effective observation time[33].

The RTA effective area algorithm splits the considered region in sub-pixels of configurable arbitrary size — see Figure 25 for a region pixelization with 0.05° pixel size. The distance between each pixel center inside the region and the observation pointing direction is considered in order to fetch the effective area value from the selected IRF. Choosing a fine pixels approximation, the algorithm simulates the offset gradient's changes that occour when the source is away from pointing.

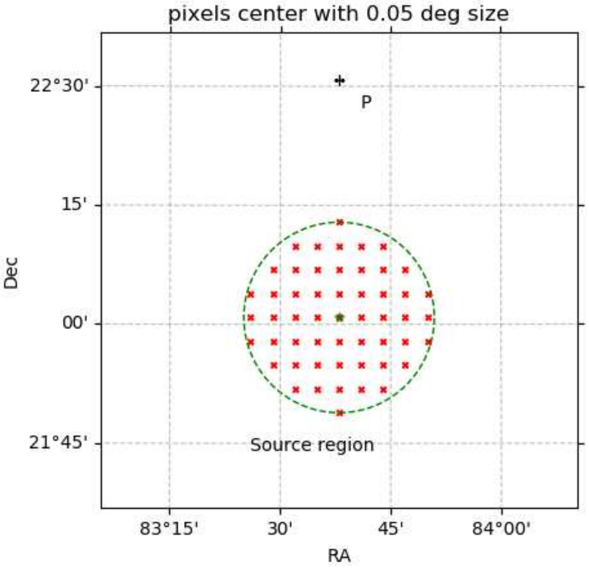

Figure 25: The effective area pixelization by RTA aperture photometry with 0.05 pixel size. Each red cross represents the center of the pixel used to compute the effective area. A fine granularity allows to simulate the instrument response within the region as the distance from the pointing increases.

As the angle offset between pointing and pixel center provides a spatial distribution of effective area values from the IRF, the energy range is involved in order to weight every pixel by an energy perspective. For each pixel a sequence of energy bins logarithmically separated are considered to retrieve the reference

---

[33] About the observation time, `ctools` introduces the livetime. The livetime is the effective observation time calculated as the exposure time multiplied by the deadtime correction factor that `ctools` estimates with an average value of 0.95. This correction factor takes into account the fact that incident photons are undercounted due to the photomultiplier tube limits — when a photon hits the detector while a pulse of a previous photon is still being elaborated, the second photon is not counted; see [6]. In our context, the full observation time is considered a good approximation.

value. Different ways to retrieve effective area values have been tested as showed in Figure 26.

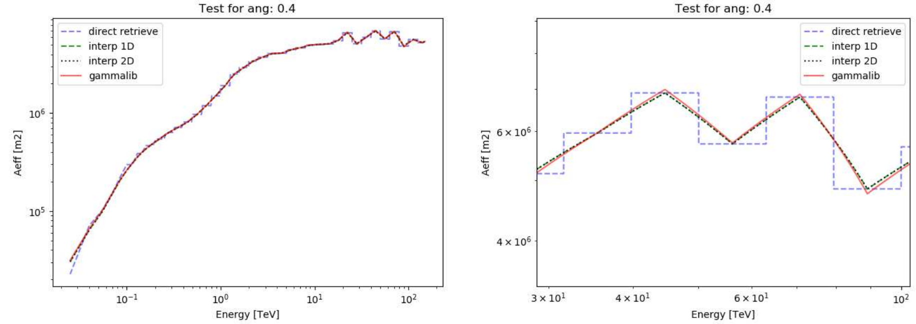

Figure 26: Effective area comparison with the different dimensions management from IRF with a fixed 0.4° theta offset. The left panel shows the effective area curve for the full energy range; the right panel shows a detail on high-energy interval (30–100 TeV). To smooth the values directly retrieved from IRFs, different interpolation types as been tested on one or both dimensions. GammaLib trend was plotted as benchmark.

Since the impact of photons with different energies has different probability, an energy-dependent weight has been introduced integrating a powerlaw probability distribution in the energy interval to compute the region effective area:

$$A_{eff}^{region}(\theta, E) = \frac{1}{N} \sum_i \int_{E_{min}}^{E_{max}} A_{eff}(\theta_i, E)\ P^{\Gamma}(E)\ dE \tag{27}$$

where θ_i is the angular distance between the pixel i and the pointing, P^{Γ} is the powerlaw probability distribution with index Γ. For each bin obtained from the initial energy input, a powerlaw-linked weight is used to determinate the specific energy bin photon contribution for each pixel: low-energy photons are present in larger number than those at high energies, therefore the A_{eff} contribution for low energy is prominent. In short, this sophistication enables the software to handle a higher number of photons in the GeV spectrum with respect to infrequent TeV photons. The powerlaw index Γ is configurable on function call. This function handles the energy range given in input dividing it by 10 bins per decade. This splitting is used both for the fetching of the data from the IRFs and for the calculation of the powerlaw-weights.
The function code is shown in Listing 6.

```
def weighted_value_for_region_w_powerlaw(self, region, pointing,
    input_energies, pixel_size=0.05, e_index=-2.4):
    """return effective area value [m2] for a specific region

    Parameters
      region:   { ’ra’: ..., ’dec’: ..., ’rad’: ... }
      pointing: { ’ra’: ..., ’dec’: ... }
      energies: a couple of values in TeV (ex: [ 0.025, 1.0 ])
      pixel_size: a value in degree (default: 0.05)
      e_index: is the powerlaw index (default: -2.4)
    """
    if len(input_energies) != 2:
        raise Exception(’need␣two␣energies’)

    # create a grid of points
    points = self.create_pixel_map(region, pixel_size)
    # select the points inside the region
    internal_points = self.select_points_in_region(points, region)
    # calculate the offsets
    offsets = self.get_thetas(pointing, internal_points)

    log_energies = np.log10(input_energies)
    # N steps for every unit of log energy
    steps = int(np.ceil(log_energies[1]-log_energies[0]) * 10)
    energies = 10**np.linspace(log_energies[0], log_energies[1],
        steps)
    powerlaw = lambda x: x**e_index
    i_full = integrate.quad(powerlaw, input_energies[0],
        input_energies[1])
    i_partials = [ integrate.quad(powerlaw, energies[i],
        energies[i+1]) for i,v in enumerate(energies[:-1]) ]
    i_factor = [ p[0]/i_full[0] for p in i_partials ]
    energies_middle = (energies[1:]+energies[:-1])/2
    n_points = len(offsets)
    val = 0
    for t in offsets:
        for i, en in enumerate(energies_middle):
            val += self.get_aeff_2d_log(t, en) * i_factor[i] /
                n_points
    return val
```

Listing 6: The effective area function with powerlaw weight.

5.1.3 The Point Spread Function factor

The Point Spread Function (PSF) describes the response of an imaging system to a point source. The PSF information in CTA IRF files is a function of energy and offset angle, and it is implemented as a superposition of three 2D Gaussian functions that are each characterized by a width and a relative amplitude[34]. As for the effective area, the PSF depends on the pointing offset θ and photon energy E. Since our goal is to compute the flux of a source enclosed in a well-defined region, the region area information is needed to determinate if the PSF

---

[34] `http://cta.irap.omp.eu/ctools/users/user_manual/irf_cta.html` .

is fully contained in the region itself.

The data in Table 9 show how the PSF is not fully contained in a 0.2 degree region when the photon energy is below 1 TeV. In this case we have an angular distance of 0.5 degrees between pointing and source point and we are assuming at least 5σ of PSF to have 100% of flux inside the selected area.

Energy	Source coverage
25.0 GeV	41.7 %
50.0 GeV	55.9 %
100.0 GeV	90.5 %
200.0 GeV	99.5 %
1.0 TeV	100.0 %
100.0 TeV	100.0 %
150.0 TeV	100.0 %

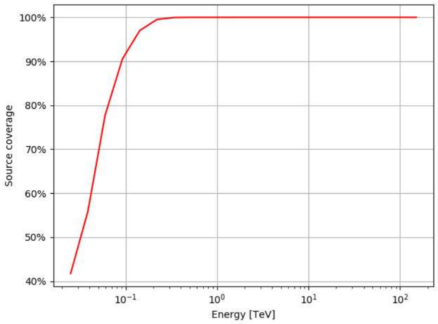

Table 9: The source coverage percentage in a 0.2° radius region at 0.5 degree of declination from pointing evaluated with RTA PSF implementation. The `prod3b-v2` `South_z20_0.5h` IRF is used.

The source coverage can be defined as

$$SC(\delta, \theta, E) = \frac{\int_0^{\delta} PSF(\theta, E)}{\int_0^{+\infty} PSF(\theta, E)} \tag{28}$$

and it represents the percentage of photons at energy E included in the region of radius δ.

Therefore, we need to apply a correction factor SC to the previously estimated effective area to consider the fraction of events that fall outside the region at lower energies. The equation 27 becomes a response of the instrument in the region:

$$R_{eff}^{region}(\theta, E) = \frac{1}{N} \sum_i \int_{E_{min}}^{E_{max}} A_{eff}(\theta_i, E)\ P^{\Gamma}(E)\ (1/SC(\delta, \theta, E))\ dE \tag{29}$$

where $SC(\delta, \theta, E)$ is the source coverage of a region with δ radius as described in 28.

The code in Listing 7 implements the PSF correction factor on the top of the effective area code (i.e. `weighted_value_for_region_w_powerlaw`).

```
def weighted_aeff_flat_psf_w_powerlaw(self, region, pointing,
    input_energies, pixel_size=0.05, e_index=-2.4):
    """return effective area value [m2] for a specific region

    Parameters
      region:   { 'ra': ..., 'dec': ..., 'rad': ... }
      pointing: { 'ra': ..., 'dec': ... }
      energies: a couple of values in TeV (ex: [ 0.025, 1.0 ])
      pixel_size: a value in degree (default: 0.05)
      e_index: is the powerlaw index (default: -2.4)
    """
    if len(input_energies) != 2:
        raise Exception('need␣two␣energies')

    psf = PSF(irf_filename=self.irf_filename)

    # create a grid of points
    points = self.create_pixel_map(region, pixel_size)
    # select the points inside the region
    internal_points = self.select_points_in_region(points, region)
    # calculate the offsets
    offsets = self.get_thetas(pointing, internal_points)

    log_energies = np.log10(input_energies)
    # N steps for every unit of log energy
    steps = int(np.ceil(log_energies[1]-log_energies[0]) * 10)
    energies = 10**np.linspace(log_energies[0], log_energies[1],
        steps)
    powerlaw = lambda x: x**e_index
    i_full = integrate.quad(powerlaw, input_energies[0],
        input_energies[1])
    i_partials = [ integrate.quad(powerlaw, energies[i],
        energies[i+1]) for i,v in enumerate(energies[:-1]) ]
    i_factor = [ p[0]/i_full[0] for p in i_partials ]
    energies_middle = (energies[1:]+energies[:-1])/2

    psf_engines = {}
    for en in energies_middle:
        psf_engines[en] = psf.get_psf_engine(region, pointing, en)
    region_radius_rad = np.deg2rad(region['rad'])

    n_points = len(offsets)
    val = 0
    for t in offsets:
        for i, en in enumerate(energies_middle):
            psf_rate = psf_engines[en](0, region_radius_rad)[0]
            val += self.get_aeff_2d_log(t, en) * i_factor[i] *
                psf_rate / n_points
    return val
```

Listing 7: Effective area function with PSF correction factor.

The PSF code is implemented in `lib.irf.PSF` class. The class constructor requires an IRF file or a PSF bintable from which to extract the parameters when needed. The function `get_psf_engine` extract values from IRF via energy and angular distance between region center and pointing and returns a function ready to evaluate the probability within a specific radius. See Listing 8.

```
def get_psf_engine(self , region , pointing , energy):
    """
    return psf engine. The engine function can elaborate the psf
        rate given
    starting and stop angle [rad]. Each engine depends by theta
        (between
    source region and pointing , and energy.

    Parameters
        region: source region (ra , dec , rad)
        pointing: pointing direction (ra , dec)
        energy: energy in TeV
    """
    region_center = utils.get_skycoord(region)
    region_radius = utils.get_angle(region[’rad’])
    pnt_center    = utils.get_skycoord(pointing)
    theta = pnt_center.separation(region_center)

    sigma_1 , sigma_2 , sigma_3 , scale , ampl_2 , ampl_3 =
        self.get_psf_values(theta , energy)
    sigmas2_rad = [ np.deg2rad(s)**2 for s in [sigma_1 , sigma_2 ,
        sigma_3] ]
    prefactor_rad = 1.0 / (2.0 * np.pi * sigmas2_rad[0] + ampl_2 *
        sigmas2_rad[1] + ampl_3 * sigmas2_rad[2])

    def _integrate_psf(start_rad , stop_rad):
        # typical params:
        #   start_rad = 0
        #   stop_rad = np.deg2rad(region_radius.degree))
        if start_rad < 0:
            raise Exception(’The␣starting␣angle␣[rad]␣must␣be␣
                positive’)
        def psf_value(delta_rad):
            d2 = delta_rad**2
            numerator  = np.exp( -1/2 * d2 / sigmas2_rad[0] )
            numerator += np.exp( -1/2 * d2 / sigmas2_rad[1] ) *
                ampl_2 if sigma_2 > 0 else 0
            numerator += np.exp( -1/2 * d2 / sigmas2_rad[2] ) *
                ampl_3 if sigma_3 > 0 else 0
            return prefactor_rad * numerator

        # integration to start_rad to stop_rad on region
            circumference of psf value
        crf_psf_fn = lambda delta: psf_value(delta) * 2.0 * np.pi
            * np.sin(delta)
        return integrate.quad(crf_psf_fn , start_rad , stop_rad)
    return _integrate_psf
```

Listing 8: The PSF function code. The engine method returns a function with the configured PSF for a specific source region, pointing direction and energy. The returned function will be integrated to obtain the source coverage.

Using the computed effective area corrected by the source coverage factor (which depends on PSF) and weighted with a powerlaw probability distribution to take into account the greater number of low energy photons, the RTA software can provide the flux in $\mathrm{ph\,cm^{-2}\,s^{-1}}$ for selected regions.

5.2 Empty-field simulation

To test the false alarm rate we simulate empty fields with a 100 seconds exposure and run the RTA aperture photometry over them. As point-source test statistic we use the square of Li and Ma significance (from 12) that we know to be

$$TS = 2 \ln \lambda = 2 \left[\ln L(M_s + M_b) - \ln L(M_b) \right] \tag{30}$$

where λ is the maximum likelihood ratio between the hypothesis that there are counts from an existing source over the background and the null hyphotesis where all the photons are only from background.

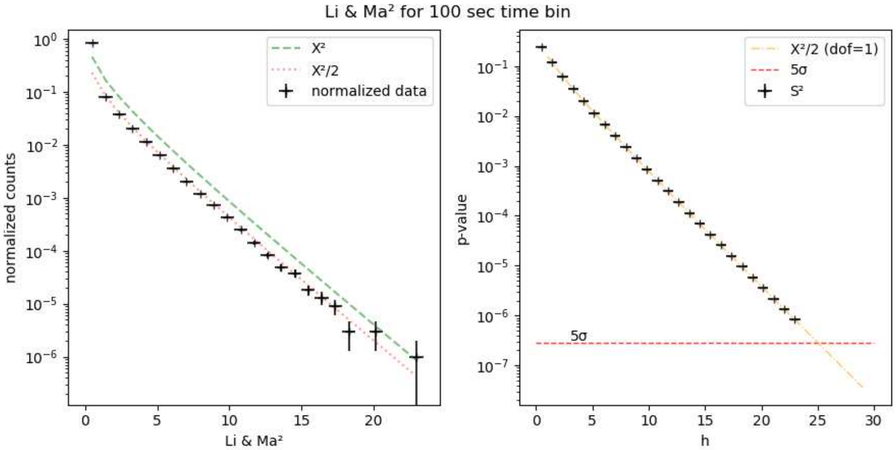

Figure 27: Li and Ma significance squared distribution for empty fields and p-value plots. 1×10^6 samples, 25 bins.

The p-value defined in equation 25 is the probability that the result of a trial in an empty field has $TS \geq h$, so a false positive detection at a level equal or higher than a defined threshold h. The Figure 27 shows the χ^2_1 distribution is followed for 100 seconds exposure time for the considered RTA aperture photometry procedure, verifying that the implemented algorithm are following the Wilks' theorem (§ 2.2), therefore the relation between the implemented significance with Li and Ma formula and Gaussian sigma is confirmed.

5.3 A Crab-like full observation

The first test for RTA aperture photometry is a full observation of the Crab-like source for a total of 80 minutes using a full wobble rotation of the source region, divides in four runs of 20 minutes each. The simulation runs through four different pointings with a full energy range of 25 GeV–150 TeV. The pointings are approximately 0.5° away from the source in four positions around the source itself. The powerlaw index for Crab-like simulation is -2.48. The IRF file used in this context is the `prod3b-v2 South z20 0.5h`.

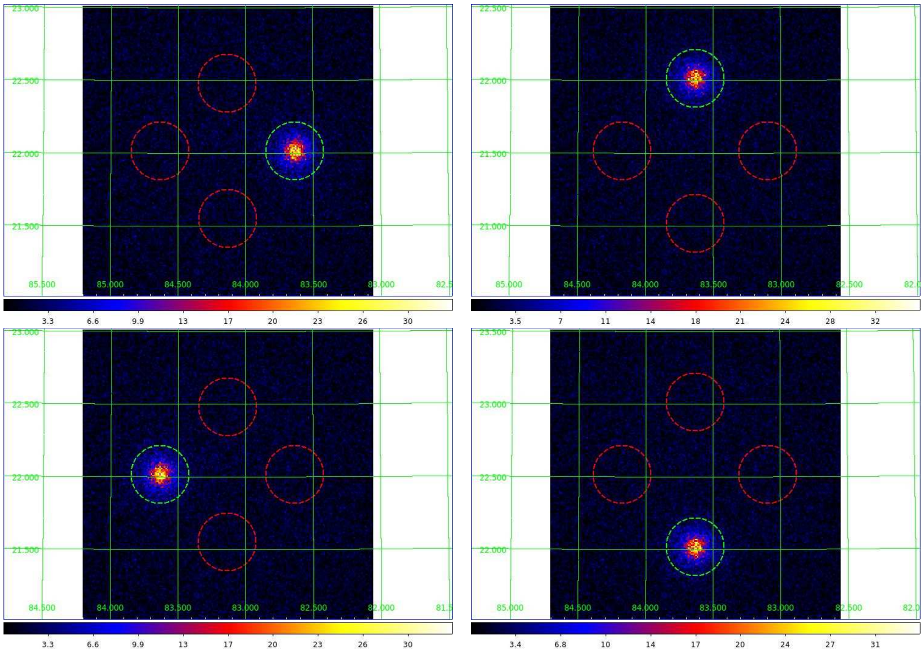

Figure 28: A full 80 minutes observation in wobble mode on Crab-like source. The order of observations is top-left, top-right, bottom-left, bottom-right.

The pipeline receives the observed events list from four different pointings but it can integrate the results from each single observation on the whole time. The analysis is composed by the total count in the on source region for each pointing. The same happens for the background region events. The background scale factor ($\alpha = 1/3$) is the same for each pointing and the source signal (i.e. the excess of photons from source) can be estimated via equation 1 from the total on and off photon counts. The same data are used to obtain the observation detection significance from equation 12.

The effective area is computed (§ 5.1.2) for each pointing, and an average value is used for the flux evaluation. However, it is expected that the effective area measurement deviation is almost zero because the pointing-source distance should be the same for each pointing used in this "integrated" mode.

Finally, the integrated flux is:

$$F = \frac{\sum_i N_i^{exc}}{\overline{A}_{eff} \sum_i t_i} \tag{31}$$

where N_i^{exc} is the excess count for pointing i, $\overline{A}_{eff}$ is the average effective area and t_i is the time for pointing i. The results for a sample of one thousand simulations are showed in the following Table 10.

samples:	1000
time [sec]:	4800
on counts:	31886.41 ± 313.69
off counts:	20850.82 ± 239.70
alpha:	1/3
excess:	24936.14 ± 303.34
detection significance:	172.11 ± 1.63
flux [$\mathrm{ph\,cm^{-2}\,s^{-1}}$]:	$4.4 \times 10^{-9} \pm 5.4 \times 10^{-11}$

Table 10: Results for Crab observation of 4800 seconds analyzed with the photometric RTA aperture photometry and wobble strategy. 1000 samples are simulated.

Such long exposures provide a very high detection significance and the flux is accurate in relation to the simulated model.
After this test, it is possibile to say that the core functions described in § 5.1 allow us to compute aperture photometry with a composition of different pointings and integrate their results with no issue. The software supports also a faster pointing swapping than 20 minutes, and can provide detection significance and flux as long as every photon list is provided with a specific source and pointing direction.

The modularity of this approach allows us to obtain partial results (i.e. on source counts, background counts, detection significance and flux) for each single pointing and to integrate the data after every step. As example of this workflow, with an extreme granularity, is shown in Figure 29. The Crab-like source was analyzed second per second. Integrating over time, the RTA aperture photometry checks each second the results taking into account the previous measures. At the sixth second the RTA aperture photometry returns the first significance over 5σ and starts measuring the flux. From that second onwards, the accumulated counts grow increasing the significance, but above all estimating the source flux with a better accuracy.

We also used the RTA aperture photometry to analyze the Crab-like source for 1800 seconds in consecutive 100 sec time bins. Taking into account the wobble pointing swap every 20 minutes, the effective area was evaluated for each pointing direction. Therefore, for each time bin we obtain on and off counts, an excess and a detection significance that have to be $S > 5\sigma$ to calculate the corresponding flux.
The lightcurve provided by RTA aperture photometry is shown in Figure 30, where it is compared with the one derived using `ctools` and the flux obtained from the model from which the simulation started. The `ctools` lightcurve program was performed in two distinct steps with respect to the two wobble pointings — the first run analyzes the lightcurve for the first 1200 seconds, and

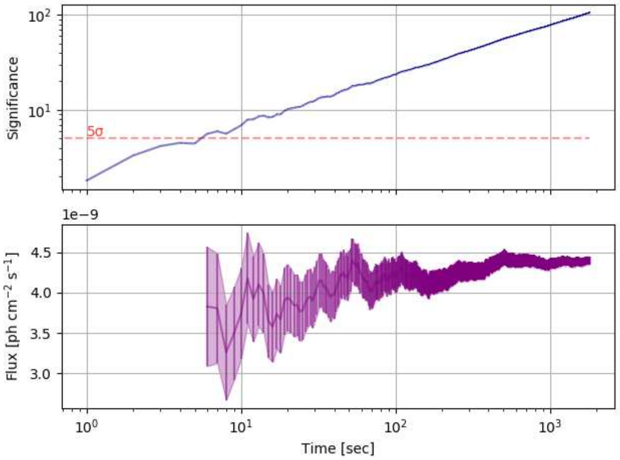

Figure 29: Significance and flux integrated (second by second) in a Crab-like simulation. The red dashed line represents the adopted 5σ significance threshold.

the second one provides results from 1200 to 1800 seconds. The energy bin number parameter for `ctools` lightcurve was set to 1 to have a fair comparison with the RTA aperture photometry, but also the 10 energy bins option was tested and results are similar.

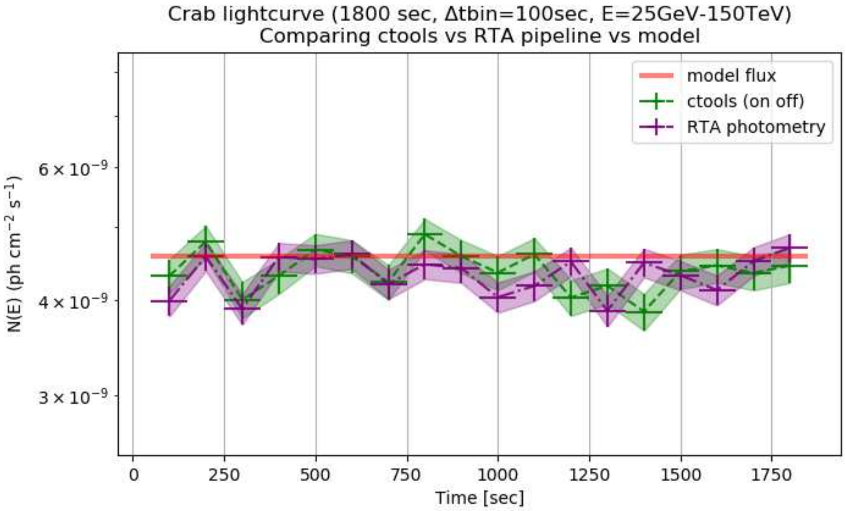

Figure 30: Comparing the Crab lightcurve between `ctools`, RTA aperture photometry data and the model from which the data were generated.

To check the pipeline consistency, 5000 simulations have been performed with RTA aperture photometry and `ctools` lightcurve. The data obtained are showed in Table 11 and plotted in Figure 31.

time	N_{on}	N_{off}	N_{exc}	Significance
100	665.62 ± 25.81	435.68 ± 20.83	520.39 ± 26.48	24.85 ± 1.04
200	665.08 ± 25.99	434.87 ± 20.77	520.12 ± 26.94	24.85 ± 1.07
300	665.56 ± 25.41	435.23 ± 20.64	520.48 ± 26.36	24.86 ± 1.05
⋮		…		
1600	662.03 ± 25.61	432.80 ± 20.96	517.76 ± 26.56	24.80 ± 1.06
1700	663.02 ± 25.58	433.35 ± 21.23	518.57 ± 26.51	24.82 ± 1.06
1800	662.42 ± 25.74	433.13 ± 20.52	518.05 ± 26.53	24.80 ± 1.05

Table 11: Crab observation of 1800 seconds analyzed with the RTA aperture photometry and wobble strategy in 100 seconds consecutive bins. 5000 samples were simulated.

As expected by previous estimations (in § 4.1), each time interval has a very high detection significance and the average flux settles on $4.4 \times 10^{-9} \pm 2.3 \times 10^{-10}$ $\mathrm{ph\,cm^{-2}\,s^{-1}}$ after 5000 samples. From the plots in Figure 31 it is possibile to observe the high correspondence between the two methods. The gap between

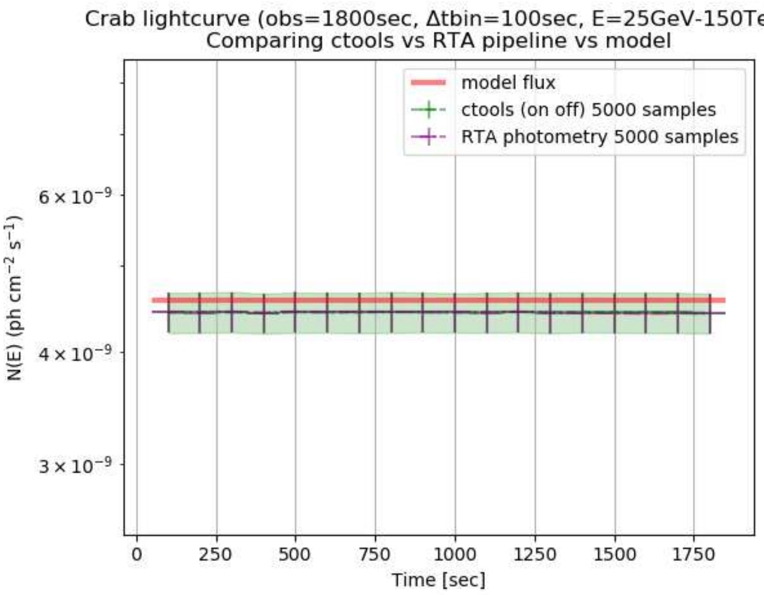

Figure 31: Comparing the Crab lightcurve computed with `ctools` and RTA aperture photometry for 5000 samples.

the computed fluxes and the starting model is because the simulated events are generated without applying the energy dispersion[35].

5.4 Short GRB afterglow

We run the RTA aperture photometry to analyze the GRB afterglow described in section 4.3. The GRB spectrum is based on the template with Gilmore's EBL absorption. The full observation lasts 1800 seconds and is performed simulating the wobble strategy with position swapping after 20 minutes.

The software was configured to bin time dimension in 100 seconds intervals, pointing at 0.5 degrees from source with 0.2° of region radius. The IRF are the `prod3b-v2 South_z40_0.5h` and simulated photons are from the full energy range 25 GeV–150 TeV. The powerlaw index used to take in account the energy distribution of photons is -2.40. A lightcurve is shown in Figure 32.

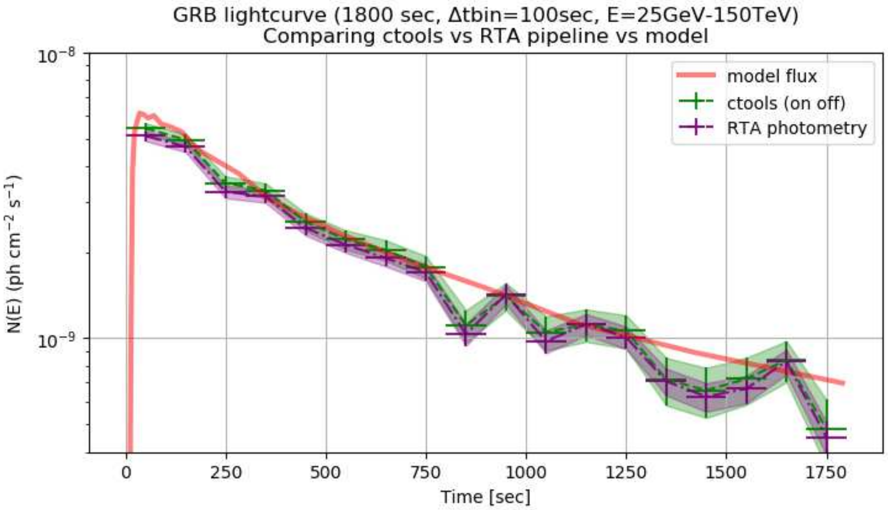

Figure 32: The GRB afterglow lightcurve computed with RTA aperture photometry and `ctools`.

The results of 5000 simulations are shown in Table 12 and the relative lightcurve is plotted in Figure 33. The flux computed with both the approaches is consistent, and the gap with the starting model is ascribed to the energy dispersion factor as stated in Crab-like simulations.

The flux computed by RTA aperture photometry and `ctools` is very similar as well as the detection significance for each time bin showed in Figure 34. Studying

---

[35] Because the detector has a finite energy resolution, the reconstructed event energy will differ from the true photon energy by a factor called energy dispersion, and this effect will become particularily important at low energies ($E < 100$ GeV); see `https://tinyurl.com/cta-energy-disp` .

this afterglow using a 100 seconds time bin provided a high significance also when the signal is poor, after 1600 seconds.

Time	N_{on}	N_{off}	N_{exc}	Significance	Flux $[\mathrm{ph\,cm^{-2}\,s^{-1}}]$
100	801.57 ± 43.47	425.06 ± 55.17	659.89 ± 47.58	29.76 ± 2.03	$5.4 \times 10^{-9} \pm 3.9 \times 10^{-10}$
200	747.71 ± 34.31	423.85 ± 33.25	606.43 ± 36.07	27.99 ± 1.44	$5.0 \times 10^{-9} \pm 3.0 \times 10^{-10}$
300	592.28 ± 31.06	421.88 ± 28.32	451.66 ± 32.84	22.53 ± 1.41	$3.7 \times 10^{-9} \pm 2.7 \times 10^{-10}$
400	497.27 ± 24.74	419.62 ± 23.74	357.40 ± 26.28	18.86 ± 1.21	$2.9 \times 10^{-9} \pm 2.2 \times 10^{-10}$
500	434.06 ± 21.03	418.36 ± 20.63	294.61 ± 22.33	16.21 ± 1.08	$2.4 \times 10^{-9} \pm 1.8 \times 10^{-10}$
600	384.10 ± 19.49	417.61 ± 20.61	244.89 ± 20.98	13.97 ± 1.08	$2.0 \times 10^{-9} \pm 1.7 \times 10^{-10}$
700	351.97 ± 19.19	417.48 ± 20.41	212.81 ± 20.55	12.44 ± 1.09	$1.7 \times 10^{-9} \pm 1.7 \times 10^{-10}$
800	334.26 ± 18.20	416.84 ± 20.31	195.32 ± 19.64	11.59 ± 1.06	$1.6 \times 10^{-9} \pm 1.6 \times 10^{-10}$
900	287.63 ± 17.02	416.25 ± 20.56	148.88 ± 18.40	9.20 ± 1.06	$1.2 \times 10^{-9} \pm 1.5 \times 10^{-10}$
1000	287.20 ± 16.65	415.79 ± 20.63	148.61 ± 17.96	9.19 ± 1.03	$1.2 \times 10^{-9} \pm 1.5 \times 10^{-10}$
1100	256.08 ± 16.01	415.38 ± 20.61	117.62 ± 17.63	7.50 ± 1.06	$9.6 \times 10^{-10} \pm 1.4 \times 10^{-10}$
1200	255.81 ± 16.32	415.54 ± 20.70	117.30 ± 17.68	7.48 ± 1.06	$9.6 \times 10^{-10} \pm 1.4 \times 10^{-10}$
1300	241.65 ± 18.86	408.49 ± 27.30	105.49 ± 21.17	6.85 ± 1.32	$8.7 \times 10^{-10} \pm 1.7 \times 10^{-10}$
1400	226.50 ± 14.86	407.53 ± 19.89	90.66 ± 16.26	5.99 ± 1.02	$7.5 \times 10^{-10} \pm 1.3 \times 10^{-10}$
1500	226.35 ± 15.07	407.79 ± 20.39	90.42 ± 16.40	5.97 ± 1.03	$7.4 \times 10^{-10} \pm 1.3 \times 10^{-10}$
1600	223.29 ± 14.71	408.06 ± 19.69	87.27 ± 15.86	5.78 ± 1.00	$7.2 \times 10^{-10} \pm 1.3 \times 10^{-10}$
1700	205.87 ± 14.64	407.48 ± 20.31	70.05 ± 16.34	4.73 ± 1.06	$5.8 \times 10^{-10} \pm 1.3 \times 10^{-10}$
1800	206.04 ± 14.53	408.18 ± 20.08	69.98 ± 15.66	4.73 ± 1.01	$5.8 \times 10^{-10} \pm 1.3 \times 10^{-10}$

Table 12: Results from RTA aperture photometry after GRB afterglow analysis.

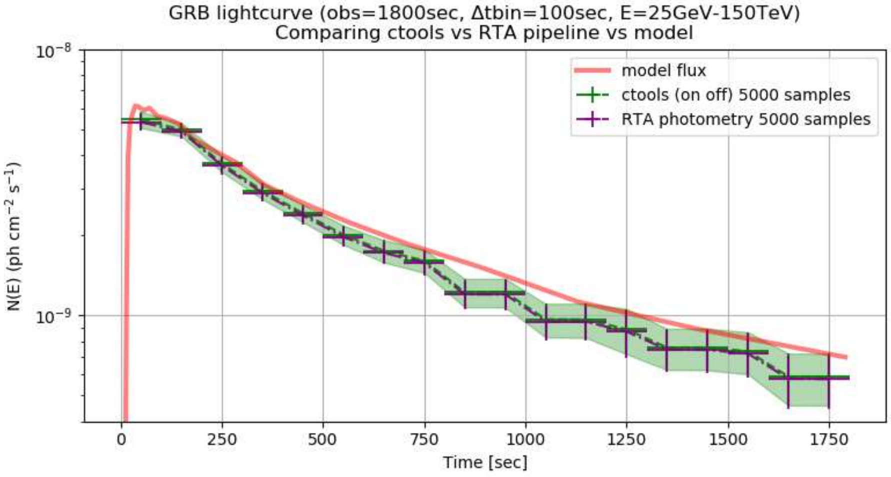

.

Figure 33: The GRB afterglow lightcurve computed with RTA aperture photometry and `ctools` for 5000 samples.

In a RTA context, a transient is unlikely to be observed from the first moment. We must assume that time passes between the generation of alarms, the repositioning of the telescope, and the effective analysis of the pointed field.

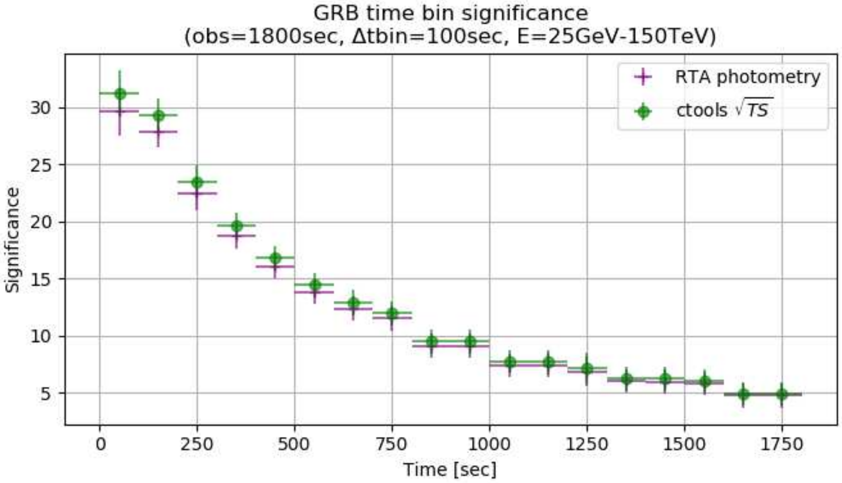

.

Figure 34: The detection significance for each time bin computed to provide the GRB afterglow lightcurve. Significance was computed with RTA aperture photometry and `ctools` $\sqrt{TS}$ for 5000 samples.

From these simulations we can deduce that a 100 seconds time bin is sufficient to capture an afterglow like the simulated one event up to 1600 seconds. Shorter time bins can give more responsive results but the signal significance can drop below 5σ fastly. Figure 35 shows the significance trend over time (and the flux, when it is possibile to compute it) choosing 20 seconds and 5 seconds

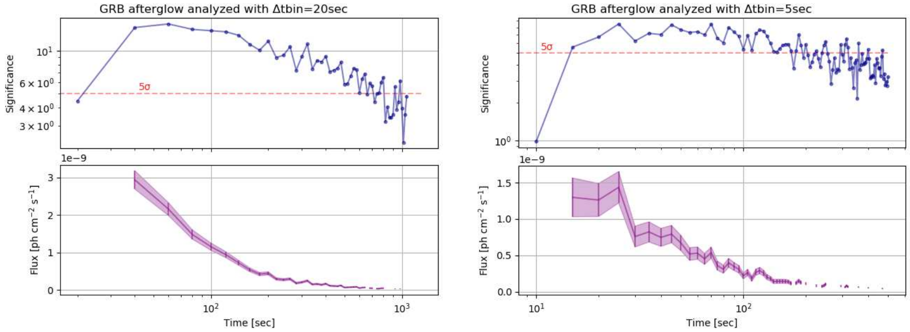

Figure 35: The RTA aperture photometry software analyzes GRB afterglow with different time bins. The upper plots show the significance over time. The lower plots show the flux for time bin when significance is above the adopted threshold. Left panel: the significance for tbin = 20 s drops after about 1000 seconds. Right panel: the significance for tbin = 5 s fluctuates around 5σ after a few hundred seconds.

time bin (left and right panels, respectively).
With longer time bin as 20 seconds, the aperture photometry software has more events to evaluate the signal and detects the GRB afterglow up to 1000 seconds after its beginning. After that, the significance drops below the threshold and the flux is not computed. If the time bin is set to 5 seconds, the software may lose the detection already after a few hundred seconds.

6 Conclusions

In this thesis I explored the potential of Cherenkov Telescope Array (CTA) to detect transient phenomena on very short timescales using the Real-Time Analysis (RTA) pipeline. A timely analysis of transients is crucial in current multi-messenger astrophysics, and the CTA program includes follow-up observations (e.g. from gravitational waves) and provides alerts to other facilities when needed (e.g. for serendipitous discoveries in the field of view).

CTA will collect γ-rays through its two arrays of telescopes placed in the two hemispheres. The γ-rays in different energy ranges will be detected combining three kind of telescopes: large-sized telescopes will be sensitive to lower energy γ-rays in the 20 GeV–150 GeV range with 4 mirrors in both hemispheres, medium-sized telescopes (in number of 15 in the northern hemisphere and 25 in the southern hemisphere) will capture γ-rays in the core energy range 150 GeV–5 TeV, and the small-sized telescopes will be sensitive to the highest energy γ-rays from 5 TeV up to 300 TeV; 70 of them will be built in the southern hemisphere only. Due to this innovative configuration, compared to existing Imaging Athmospheric Cherenkov Telescopes, CTA will cover a wider energy range with a significantly larger field-of-view and about an order of magnitude improvement in sensitivity.

One of the methods which can be adopted to detect and characterize very-high energy sources relies on the on/off technique. As described in section 2.1, this technique deduces the source emitted photons by subtracting an estimation of background counts from a region enclosing the source. The detection can be evaluated obtaining on- and off-source counts with the so-called on/off technique. Flux and lightcurves can be computed from the estimated emitted photons and considering the effective area in the region and the observation time.
Using the `ctools` framework, I performed a maximum likelihood on/off analysis, based on the simulated photon counts (within the on source region and the background regions) and the predicted ones, and I obtained the best-fit parameters to describe the target. The background photons are derived using the reflected-region method, a technique that estimates the counts that have to be subtracted from the source region by mediating among selected background regions having similar characteristics as the source (e.g. same offset from the pointing direction, same homogeneity in the distribution of the background photons, etc.).

The on/off analysis was performed simulating the CTA full-array to collect photons in a wide range of energies (between 25 GeV and 150 TeV) in decreasing time intervals from 1800 seconds to 1 second. The results for each observation time provided γ-ray source detection significance useful to evaluate short time scales. These time boundaries can be considered as detection thresholds to understand the limits for the RTA pipeline software. Empty-field analysis confirmed that the Test statistic values provided by the `ctools` Maximum Likelihood Estimation (MLE) are reliable to evaluate the significance of

the detection. The obtained significance was verified with Li and Ma formula. Crab-like simulations showed that a similar flux can be detected within 3 seconds with a full-array configuration. More simulations showed that, selecting narrower energy ranges as reported in A.3, CTA can still detect a Crab-like source in tens of seconds. A short GRB afterglow template provided by L. Nava and POSyTIVE project allowed me to simulate a GRB afterglow scenario. The simulated GRB afterglow detection was confirmed at 5σ with just 20 seconds observation in full-array configuration, despite the absorption of high-energy γ-rays due to Extragalactic Background Light (which is the totality of light emitted by stars and AGN over the lifetime of the Universe).
From the data produced during these on/off analyses, some results related to the short-time uncertainties of the differential and integral sensitivity, shown at the 2019 CTA Consortium Meeting, have been extracted.

After the tests previously described, I implemented algorithms and procedures to perform aperture photometry in γ-ray analysis, whose results are comparable with best-fit obtained using MLE. Whereas `ctools` was designed as a high-level tool to perform "vertical" analyses (i.e. from the list of events to the desired result), the new tool allows us to compose different processes to obtain more results (significance, counts and fluxes in different regions of the field of view, lightcurve) at the same time. This approach saves time, and the software has proven to be simple, reliable, flexible and easily modular; another advantage is that the detection significance is computed in a full "passive" mode, based only on the observed data without input from the user — instead, `ctools` requires as input a model to fit for every analysis process.
Sophisticated functions were implemented to estimate the flux accurately, taking into account the effective area of the system and the source coverage of the region. The effective area was computed as a composition of pixels considering the typical wobble offset between the pointing direction and the source position. The source coverage was estimated using the width of the point spread function with respect to the region radius: low-energy photons are more scattered than high-energy ones, spilling out from the source region, therefore low-energy photons are more underestimated inside the region then the high-energy ones. Because the photometric approach integrates on the full energy range, the energy information of the photon is lost; to overcome this issue, I used a powerlaw distribution to weight the photons population inside the source region. This gimmick enables a great accuracy in flux extimation but introduces a user input as the powerlaw index, which makes the feature less automatic (i.e. less "passive", as stated above); in other words, we need to consider in advance the type of target we are going to observe and choose the appropriate powerlaw index to estimate the flux.

Tests indicate that the aperture photometry tool is faster than the likelihood approach, making it particularly suitable in the RTA pipeline and, in particular, with respect to the transient searches that are a key science project for CTA.
Some measurements on execution times were taken on GRB afterglow 100-second photons list. In order to compute the detection significance, 0.25 s are

sufficent; the flux can be calculated in the same time after an 1.8 s initial setup, deriving by the region data (i.e. effective area and point spread function) with respect to pointing direction[36]. Considering the RTA requirement to send alerts within 30 seconds, the aperture photometry tool consumes at most 2 seconds to provide significance and flux for a 100-second photon lists.

Exploiting the flexibility of the RTA aperture photometry tool, different approaches to data aggregation over time (binning or continuously) have been tested, proving that interesting results can be obtained analyzing data with a very small time granularity and virtually with different pointings during the same observation. This information allows us to evaluate how much time the pipeline has to find a transient like a GRB and how large the time bin must be to ensure a good detection.

The aperture photometry software has been used to estimate the lightcurve (time bin of 100 seconds) of a Crab-like source with a very high significance. A real-time test integrating the emission second by second showed that we can obtain a 5σ detection after 5 seconds and a converging flux estimation after tens of seconds.

The same tool has been used to compute the GRB afterglow lightcurve. With 100-second time bin to analyze, the RTA pipeline can provide detection of the GRB afterglow until 1500 seconds after the beginning of the event. Some tests have been run with different time bin: when the analysis is applied to 20-second intervals, the pipeline can have a detection at 5σ for about 1000 seconds. If the time bin for the analysis is reduced to 5 seconds, the tool has a detection window of about two hundreds seconds. Flux estimations in a shorter time are less accurate than when a longer time is used.

Further developments can be summarized as follows:

- to test the aperture photometry tool with IRFs describing specific types of telescope (e.g. large-sized telescope); the tests performed so far used the public full array IRFs that do not necessarily correspond to the medium and low-energy configuration that will search for GRB afterglows and flares under 10 TeV;
- to test an exponentially cut-off powerlaw spectral model in order to define the tool efficiency when EBL absorption affects the observed astrophysical source at high energy;
- to understand the feasibility of the RTA aperture photometry approach when the background is not homogeneous as on the Galactic plane;
- more checks on execution times with input event lists with different lengths;
- to implement a solution to take into account the energy dispersion of reconstructed photons at low energy;

---

[36] If more lists of events share the same pointing direction and source region information, the initial setup time can be evaluated only one time.

- to develop a better interface to allow analysis to the end-users not only in RTA mode;
- to generalize and optimize specific features to increase the performance and maintentenance, such as the off regions generator and events handling.

Finally, I think that this tool can be a starting point to improve and automate the RTA pipeline, developing algorithms to resolve dynamically

(a) the time bin choice strategies using the integration time feature to detect transient phenomena in a tailored way;

(b) the background extimation in aperture photometry analysis using an automatic strategy aimed at optimizing the source region radius and, consequently, the pointing strategy with respect to the source.

Acknowledgements

This thesis took place at Istituto Nazionale di Astrofisica / Osservatorio di astrofisica e scienza dello spazio (INAF OAS) in Bologna.

I would like to dedicate this space to those who, with dedication and patience, contributed to the realization of this work.

A special thanks goes to my relator Professor Cristian Vignali for his precision and infinite availability.

Thanks also to my correlators Andrea Bulgarelli and Valentina Fioretti, for their indications and suggestions, for their valuable advice and for having promptly suggested the right changes to make to my thesis.

Thanks to Rubén López-Coto from INFN – Section of Padua of the LST Collaboration for the explanations about the large-sized telescope wobble pointing strategy.

Thanks to Leonardo, Nicolò, Ambra, Giulia, Claudio, Federico, Vito, and all the people in the INAF staff, who shared with me these months of chatting and different experiences.

Thanks to all my course colleagues and friends, Claudia, Graziano, Manuela, Giacomo, Monica, Valerio, Stefano for always encouraging me.

Thanks to my family, especially my late grandmother, uncle and aunt who made me feel their closeness and affection.

I infinitely thank my wife, Angela. Without her support, this thesis work would not even exist.

A Appendix

A.1 Flux comparison between `ctools` and aperture photometry

Using the on/off analysis with `ctools` we can obtain the best-fit model that provides a flux for each time window elaborated as described in § 4.1. The data in Table 13 show flux values computed with likelihood method from `ctools` and aperture photometry method implemented in RTA pipeline code (§ 5.1). The corresponding plot in Figure 36.

secs	Likelihood flux [$\mathrm{ph\,cm^{-2}\,s^{-1}}$]	Aperture ph. flux [$\mathrm{ph\,cm^{-2}\,s^{-1}}$]
1800	$4.4 \times 10^{-9} \pm 5.2 \times 10^{-11}$	$4.4 \times 10^{-9} \pm 5.3 \times 10^{-11}$
600	$4.4 \times 10^{-9} \pm 8.9 \times 10^{-11}$	$4.4 \times 10^{-9} \pm 9.0 \times 10^{-11}$
100	$4.4 \times 10^{-9} \pm 2.2 \times 10^{-10}$	$4.4 \times 10^{-9} \pm 2.3 \times 10^{-10}$
60	$4.4 \times 10^{-9} \pm 2.9 \times 10^{-10}$	$4.4 \times 10^{-9} \pm 2.9 \times 10^{-10}$
30	$4.4 \times 10^{-9} \pm 4.1 \times 10^{-10}$	$4.4 \times 10^{-9} \pm 4.1 \times 10^{-10}$
20	$4.4 \times 10^{-9} \pm 5.0 \times 10^{-10}$	$4.4 \times 10^{-9} \pm 5.1 \times 10^{-10}$
10	$4.4 \times 10^{-9} \pm 7.0 \times 10^{-10}$	$4.4 \times 10^{-9} \pm 7.1 \times 10^{-10}$
5	$4.4 \times 10^{-9} \pm 1.0 \times 10^{-9}$	$4.4 \times 10^{-9} \pm 1.0 \times 10^{-9}$
4	$4.4 \times 10^{-9} \pm 1.1 \times 10^{-9}$	$4.4 \times 10^{-9} \pm 1.1 \times 10^{-9}$
3	$4.4 \times 10^{-9} \pm 1.3 \times 10^{-9}$	$4.4 \times 10^{-9} \pm 1.3 \times 10^{-9}$
2	$4.4 \times 10^{-9} \pm 1.6 \times 10^{-9}$	$4.4 \times 10^{-9} \pm 1.6 \times 10^{-9}$
1	$4.5 \times 10^{-9} \pm 2.2 \times 10^{-9}$	-

Table 13: Comparison between fluxes computed with likelihood method and aperture photometry RTA code. The likelihood flux was provided by the best-fit model obtained with `ctools`. The flux in second column was calculated from the excess found with aperture photometry analysis as described in § 5.1. The results come from 10K simulated Crab-like source spectra. Pointing is at $dec_{source}\ +0.5^{\circ}$, E_{min} is 25 GeV, E_{max} is 150.0 TeV.

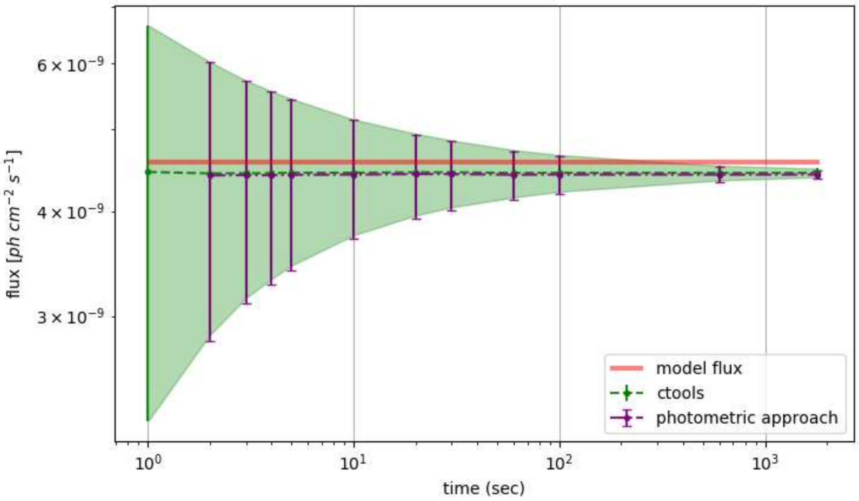

Figure 36: The flux comparison between `ctools` and photometric evaluation. The two approaches are equivalent for the flux calculation. The gap between the computed fluxes and the starting model is due to the missing contribution from energy dispersion.

A.2 Real-Time Analysis python code snippet

In this section it is shown some code snippets from the classes that provide data for the Real-Time Analysis are shown.

A.2.1 Photometrics class

A synopsis of regions generation and photometrics counts.

```python
from lib.photometry import Photometrics

phm = Photometrics({ ’events_list’: events_list })
# ... or ...
phm = Photometrics({ ’events_filename’: fits_filename })

# count events from region with optional energy thresholds
on_count    = phm.region_counter(src_coords, radius,
    emin=energy_min, emax=energy_max)

# background counts
off_regions = phm.cross_regions(pnt_coords, src_coords, radius)
# ... or ...
other_off_regions = phm.reflected_regions(pnt_coords, src_coords,
    radius)

off_count = 0
for region in off_regions:
    off_count += phm.region_counter(region, radius)

# an helper to write the region ds9 string into file
phm.write_region(off_regions, ’path/to/file/off.reg’, color=’red’,
    dash=True, width=2)
```

Listing 9: A brief use case of photometric code.

The Photometric class constructor handles events as fits bintable or list of events as showed in 10. The list of events can be extract from different formats and convert to recarray with a code similar to 11. This conversion, for example, is needed when the events are extracted from a `ctools` observation not saved on hard disk (e.g. `fits = gammalib.GFits() fits.table(’EVENTS’)`).

```python
from astropy.coordinates import SkyCoord, Angle
from astropy.io import fits
from lib import utils
from regions import CircleSkyRegion
from regions import write_ds9
import astropy.units as u
import numpy as np
import logging
logging.basicConfig(level=logging.WARN)

# Bintable columns:
# 0  name = ’EVENT_ID’; format = ’1J’; bscale = 1; bzero =
    2147483648
#    name = ’TIME’; format = ’1D’; unit = ’s’
#    name = ’RA’; format = ’1E’; unit = ’deg’
#    name = ’DEC’; format = ’1E’; unit = ’deg’
```

```
#    name = ’ENERGY’; format = ’1E’; unit = ’TeV’
# 5  name = ’DETX’; format = ’1E’; unit = ’deg’
# 6  name = ’DETY’; format = ’1E’; unit = ’deg’
#    name = ’MC_ID’; format = ’1J’

class Photometrics():
    def __init__(self, args):
        self.events_data = None
        self.events_filename = None
        self.mandatory_fields = [’RA’, ’DEC’, ’ENERGY’]
        if ’events_filename’ in args:
            self.events_filename = args[’events_filename’]
            self.events_data =
                self.load_data_from_fits_file(self.events_filename)
        elif ’events_list’ in args:
            self.events_data = args[’events_list’]
        self.events_list_checks()

    def events_list_checks(self):
        """Data con be a FITS_rec or a np.recarray
        see here:
        https://docs.astropy.org/en/stable/io/fits/usage/table.html
        """
        if self.events_data is None:
            raise Exception(’Events␣data␣is␣empy.␣Need␣a␣events␣
                list.’)
        if isinstance(self.events_data, fits.fitsrec.FITS_rec):
            for f in self.mandatory_fields:
                if f not in self.events_data.columns.names:
                    raise Exception("Events␣data␣has␣no␣’{}’␣
                        col".format(f))
        elif isinstance(self.events_data, np.recarray):
            for f in self.mandatory_fields:
                if f not in self.events_data.dtype.names:
                    raise Exception("Events␣data␣has␣no␣’{}’␣
                        col".format(f))
        else:
            raise Exception("Events␣data␣must␣be␣FITS_rec␣or␣
                np.recarray")

    @staticmethod
    def load_data_from_fits_file(filename):
        """Load events extension data from a fits file.
        Parameters
            filename: str

        Returns:
            events_bintable data
        """
        hdul = fits.open(filename)
        events_bintable = hdul[’EVENTS’]
        data = events_bintable.data
        hdul.close()
        return data
```

Listing 10: The Photometrics class constructor in lib/photometry.py module

```
# ...
ev_list = []
tuples = [ (events_data['RA'][i], events_data['DEC'][i],
    events_data['ENERGY'][i]) for i in range(events_num) ]
ev_list += tuples
np.rec.array(ev_list, formats='float,float,float',
    names='RA,DEC,ENERGY')
```

Listing 11: A data transformer to other format to rec.array with names

A.3 More Crab data obtained with `ctools`

All the following tables show data from 10K simulated Crab-like source, with +0.5° declination. The background is extracted using a four regions reflection algorithm. The data energy range is provided in the first column; the lower boundary is increasing throughout the following tables. TS is from `ctools`; the photon counts and significance are from photometric approach and Li & Ma equation. These data are cited in § 4.1.

Energy [TeV]	secs	TS	N_{on}	N_{off}	N_{exc}	Significance	$\sigma/Sign.$
0.029–150.0	1800	15515.37 ± 276.76	11316.70 ± 106.74	8910.90 ± 94.44	9088.97 ± 109.32	112.47 ± 1.10	0.01
0.029–150.0	600	5172.51 ± 158.71	3771.87 ± 60.84	2970.44 ± 55.38	3029.26 ± 62.34	64.93 ± 1.09	0.02
0.029–150.0	100	862.93 ± 65.52	628.81 ± 25.34	495.36 ± 22.47	504.97 ± 25.96	26.50 ± 1.11	0.04
0.029–150.0	60	518.17 ± 50.89	377.15 ± 19.67	297.19 ± 17.38	302.85 ± 20.16	20.52 ± 1.11	0.05
0.029–150.0	30	260.53 ± 36.04	188.84 ± 13.86	148.51 ± 12.11	151.71 ± 14.18	14.53 ± 1.10	0.08
0.029–150.0	20	174.08 ± 29.45	125.85 ± 11.31	98.88 ± 9.86	101.13 ± 11.59	11.86 ± 1.10	0.09
0.029–150.0	10	87.44 ± 20.64	62.86 ± 7.97	49.48 ± 6.93	50.49 ± 8.13	8.37 ± 1.09	0.13
0.029–150.0	5	44.33 ± 14.83	31.43 ± 5.66	24.75 ± 4.90	25.24 ± 5.79	5.91 ± 1.10	0.19
0.029–150.0	4	35.69 ± 13.27	25.12 ± 5.09	19.80 ± 4.40	20.17 ± 5.21	5.28 ± 1.11	0.21
0.029–150.0	3	27.06 ± 11.51	18.85 ± 4.38	14.85 ± 3.79	15.14 ± 4.48	4.57 ± 1.10	0.24
0.029–150.0	2	18.46 ± 9.59	12.57 ± 3.59	9.92 ± 3.11	10.09 ± 3.68	3.72 ± 1.12	0.30
0.029–150.0	1	9.91 ± 6.89	6.31 ± 2.51	4.95 ± 2.21	5.07 ± 2.57	2.60 ± 1.10	0.42

Energy [TeV]	secs	TS	N_{on}	N_{off}	N_{exc}	Significance	$\sigma/Sign.$
0.041–150.0	1800	14949.23 ± 270.37	9949.50 ± 99.93	6244.12 ± 78.99	8388.47 ± 102.02	114.97 ± 1.10	0.01
0.041–150.0	600	4984.22 ± 155.22	3316.45 ± 57.17	2081.40 ± 46.20	2796.10 ± 58.36	66.38 ± 1.09	0.02
0.041–150.0	100	831.44 ± 64.07	552.73 ± 23.76	347.04 ± 18.74	465.97 ± 24.20	27.09 ± 1.10	0.04
0.041–150.0	60	499.40 ± 49.87	331.58 ± 18.47	208.14 ± 14.47	279.55 ± 18.84	20.98 ± 1.11	0.05
0.041–150.0	30	251.06 ± 35.28	166.05 ± 12.98	104.05 ± 10.19	140.04 ± 13.25	14.85 ± 1.11	0.07
0.041–150.0	20	167.78 ± 28.79	110.68 ± 10.59	69.25 ± 8.31	93.36 ± 10.82	12.13 ± 1.11	0.09
0.041–150.0	10	84.36 ± 20.28	55.29 ± 7.50	34.65 ± 5.85	46.63 ± 7.63	8.56 ± 1.10	0.13
0.041–150.0	5	42.75 ± 14.46	27.65 ± 5.29	17.37 ± 4.13	23.31 ± 5.40	6.04 ± 1.11	0.18
0.041–150.0	4	34.43 ± 12.93	22.09 ± 4.75	13.89 ± 3.71	18.62 ± 4.84	5.40 ± 1.11	0.21
0.041–150.0	3	26.09 ± 11.21	16.57 ± 4.11	10.42 ± 3.21	13.97 ± 4.18	4.67 ± 1.11	0.24
0.041–150.0	2	17.79 ± 9.33	11.04 ± 3.36	6.96 ± 2.63	9.30 ± 3.43	3.79 ± 1.13	0.30
0.041–150.0	1	9.50 ± 6.71	5.53 ± 2.36	3.48 ± 1.86	4.66 ± 2.41	2.56 ± 1.16	0.45

Energy [TeV]	secs	TS	N_{on}	N_{off}	N_{exc}	Significance	$\sigma/Sign.$
0.065–150.0	1800	14083.06 ± 262.08	8209.23 ± 90.06	3926.49 ± 62.29	7227.61 ± 91.43	113.57 ± 1.09	0.01
0.065–150.0	600	4695.39 ± 151.25	2736.50 ± 51.88	1308.93 ± 36.42	2409.27 ± 52.67	65.57 ± 1.09	0.02
0.065–150.0	100	783.29 ± 62.24	456.08 ± 21.43	218.27 ± 14.80	401.51 ± 21.74	26.76 ± 1.10	0.04
0.065–150.0	60	470.60 ± 48.42	273.61 ± 16.67	130.87 ± 11.45	240.89 ± 16.93	20.73 ± 1.10	0.05
0.065–150.0	30	236.58 ± 34.39	137.02 ± 11.79	65.41 ± 8.07	120.67 ± 11.97	14.67 ± 1.10	0.08
0.065–150.0	20	158.04 ± 28.19	91.31 ± 9.64	43.56 ± 6.61	80.42 ± 9.79	11.98 ± 1.11	0.09
0.065–150.0	10	79.48 ± 19.78	45.61 ± 6.78	21.81 ± 4.65	40.16 ± 6.87	8.45 ± 1.10	0.13
0.065–150.0	5	40.36 ± 14.11	22.82 ± 4.80	10.93 ± 3.29	20.08 ± 4.88	5.97 ± 1.11	0.19
0.065–150.0	4	32.52 ± 12.63	18.23 ± 4.31	8.74 ± 2.97	16.05 ± 4.37	5.33 ± 1.11	0.21
0.065–150.0	3	24.65 ± 10.94	13.66 ± 3.73	6.56 ± 2.56	12.02 ± 3.78	4.60 ± 1.12	0.24
0.065–150.0	2	16.82 ± 9.09	9.11 ± 3.06	4.38 ± 2.09	8.01 ± 3.11	3.69 ± 1.18	0.32
0.065–150.0	1	8.81 ± 6.58	4.56 ± 2.15	2.17 ± 1.47	4.02 ± 2.18	2.24 ± 1.28	0.57

Energy [TeV]	secs	TS	N_{on}	N_{off}	N_{exc}	Significance	$\sigma/Sign.$
0.103–150.0	1800	11774.62 ± 238.13	6229.37 ± 78.80	2240.05 ± 47.38	5669.36 ± 79.74	106.14 ± 1.09	0.01
0.103–150.0	600	3926.62 ± 137.43	2076.58 ± 45.55	746.50 ± 27.64	1889.96 ± 46.09	61.28 ± 1.09	0.02
0.103–150.0	100	655.33 ± 56.54	346.11 ± 18.72	124.43 ± 11.18	315.00 ± 18.95	25.02 ± 1.10	0.04
0.103–150.0	60	393.71 ± 43.83	207.61 ± 14.53	74.57 ± 8.61	188.97 ± 14.72	19.38 ± 1.10	0.06
0.103–150.0	30	198.10 ± 31.26	103.97 ± 10.28	37.23 ± 6.09	94.66 ± 10.43	13.72 ± 1.11	0.08
0.103–150.0	20	132.29 ± 25.55	69.22 ± 8.42	24.81 ± 4.98	63.02 ± 8.53	11.19 ± 1.11	0.10
0.103–150.0	10	66.72 ± 17.94	34.60 ± 5.96	12.41 ± 3.53	31.50 ± 6.02	7.90 ± 1.10	0.14
0.103–150.0	5	33.97 ± 12.76	17.29 ± 4.19	6.22 ± 2.50	15.74 ± 4.23	5.56 ± 1.13	0.20
0.103–150.0	4	27.38 ± 11.38	13.81 ± 3.75	4.96 ± 2.25	12.57 ± 3.78	4.93 ± 1.18	0.24
0.103–150.0	3	20.75 ± 9.87	10.34 ± 3.25	3.73 ± 1.93	9.41 ± 3.28	4.17 ± 1.25	0.30
0.103–150.0	2	14.12 ± 8.13	6.89 ± 2.65	2.49 ± 1.58	6.26 ± 2.68	3.12 ± 1.40	0.45
0.103–150.0	1	7.06 ± 5.97	3.44 ± 1.86	1.23 ± 1.11	3.13 ± 1.88	1.54 ± 1.32	0.86

Energy [TeV]	secs	TS	N_{on}	N_{off}	N_{exc}	Significance	$\sigma/Sign.$
0.163–150.0	1800	9060.29 ± 207.76	4374.07 ± 66.34	1162.51 ± 33.90	4083.44 ± 67.04	94.38 ± 1.09	0.01
0.163–150.0	600	3021.99 ± 119.23	1458.22 ± 38.22	387.25 ± 19.83	1361.41 ± 38.57	54.50 ± 1.08	0.02
0.163–150.0	100	504.44 ± 48.72	242.98 ± 15.51	64.54 ± 8.03	226.84 ± 15.68	22.24 ± 1.08	0.05
0.163–150.0	60	303.21 ± 37.66	145.78 ± 12.03	38.69 ± 6.19	136.11 ± 12.15	17.23 ± 1.08	0.06
0.163–150.0	30	152.76 ± 26.76	73.05 ± 8.55	19.31 ± 4.37	68.23 ± 8.63	12.20 ± 1.08	0.09
0.163–150.0	20	102.14 ± 21.94	48.65 ± 7.01	12.87 ± 3.58	45.43 ± 7.08	9.95 ± 1.09	0.11
0.163–150.0	10	51.62 ± 15.46	24.29 ± 4.93	6.43 ± 2.55	22.68 ± 4.97	7.02 ± 1.11	0.16
0.163–150.0	5	26.35 ± 11.05	12.13 ± 3.52	3.22 ± 1.80	11.33 ± 3.54	4.72 ± 1.43	0.30
0.163–150.0	4	21.20 ± 9.83	9.70 ± 3.15	2.57 ± 1.61	9.06 ± 3.17	4.02 ± 1.55	0.39
0.163–150.0	3	15.99 ± 8.46	7.27 ± 2.73	1.92 ± 1.36	6.79 ± 2.75	3.18 ± 1.62	0.51
0.163–150.0	2	10.68 ± 7.00	4.83 ± 2.22	1.29 ± 1.13	4.51 ± 2.24	2.06 ± 1.56	0.76
0.163–150.0	1	4.98 ± 5.27	2.41 ± 1.56	0.63 ± 0.80	2.26 ± 1.57	0.81 ± 1.10	1.35

Energy [TeV]	secs	TS	N_{on}	N_{off}	N_{exc}	Significance	$\sigma/Sign.$
0.258–150.0	1800	6595.38 ± 175.16	3007.32 ± 54.87	652.55 ± 25.28	2844.19 ± 55.34	80.87 ± 1.07	0.01
0.258–150.0	600	2199.66 ± 100.32	1002.57 ± 31.63	217.47 ± 14.86	948.20 ± 31.81	46.69 ± 1.07	0.02
0.258–150.0	100	367.13 ± 41.19	166.99 ± 12.84	36.30 ± 6.01	157.91 ± 12.96	19.05 ± 1.07	0.06
0.258–150.0	60	220.71 ± 31.86	100.13 ± 9.95	21.74 ± 4.64	94.70 ± 10.04	14.75 ± 1.07	0.07
0.258–150.0	30	111.26 ± 22.75	50.14 ± 7.09	10.85 ± 3.29	47.43 ± 7.15	10.44 ± 1.09	0.10
0.258–150.0	20	74.47 ± 18.67	33.39 ± 5.83	7.22 ± 2.69	31.58 ± 5.88	8.51 ± 1.11	0.13
0.258–150.0	10	37.78 ± 13.10	16.69 ± 4.10	3.61 ± 1.90	15.78 ± 4.13	5.84 ± 1.42	0.24
0.258–150.0	5	19.26 ± 9.21	8.33 ± 2.91	1.81 ± 1.35	7.88 ± 2.93	3.40 ± 1.80	0.53
0.258–150.0	4	15.49 ± 8.21	6.65 ± 2.59	1.44 ± 1.20	6.29 ± 2.61	2.72 ± 1.78	0.65
0.258–150.0	3	11.65 ± 7.17	4.98 ± 2.25	1.09 ± 1.04	4.71 ± 2.26	1.98 ± 1.65	0.83
0.258–150.0	2	7.94 ± 6.27	3.30 ± 1.83	0.73 ± 0.85	3.12 ± 1.84	1.17 ± 1.35	1.15
0.258–150.0	1	3.87 ± 5.45	1.65 ± 1.28	0.36 ± 0.60	1.56 ± 1.29	0.39 ± 0.78	1.99

Energy [TeV]	secs	TS	N_{on}	N_{off}	N_{exc}	Significance	$\sigma/Sign.$
0.408–150.0	1800	4746.26 ± 149.09	2099.17 ± 46.07	406.46 ± 20.06	1997.55 ± 46.47	68.68 ± 1.08	0.02
0.408–150.0	600	1582.88 ± 84.85	699.66 ± 26.64	135.40 ± 11.59	665.81 ± 26.75	39.65 ± 1.06	0.03
0.408–150.0	100	264.39 ± 34.56	116.52 ± 10.79	22.60 ± 4.75	110.87 ± 10.84	16.17 ± 1.06	0.07
0.408–150.0	60	159.06 ± 26.98	69.86 ± 8.38	13.53 ± 3.67	66.48 ± 8.43	12.52 ± 1.07	0.09
0.408–150.0	30	80.32 ± 19.21	34.99 ± 5.93	6.75 ± 2.61	33.30 ± 5.97	8.85 ± 1.12	0.13
0.408–150.0	20	53.79 ± 15.70	23.29 ± 4.87	4.50 ± 2.14	22.16 ± 4.90	7.14 ± 1.30	0.18
0.408–150.0	10	27.40 ± 11.11	11.64 ± 3.43	2.25 ± 1.51	11.07 ± 3.45	4.47 ± 1.83	0.41
0.408–150.0	5	14.01 ± 7.99	5.81 ± 2.42	1.13 ± 1.07	5.52 ± 2.43	2.24 ± 1.77	0.79
0.408–150.0	4	11.37 ± 7.30	4.63 ± 2.16	0.90 ± 0.96	4.41 ± 2.17	1.68 ± 1.62	0.96
0.408–150.0	3	8.80 ± 6.87	3.45 ± 1.86	0.67 ± 0.83	3.28 ± 1.87	1.14 ± 1.37	1.20
0.408–150.0	2	6.49 ± 6.80	2.30 ± 1.52	0.45 ± 0.67	2.18 ± 1.52	0.63 ± 1.02	1.63
0.408–150.0	1	4.37 ± 6.76	1.15 ± 1.07	0.22 ± 0.47	1.09 ± 1.07	0.19 ± 0.54	2.81

Energy [TeV]	secs	TS	N_{on}	N_{off}	N_{exc}	Significance	$\sigma/Sign.$
0.650–150.0	1800	3418.69 ± 125.04	1484.65 ± 38.48	266.75 ± 16.25	1417.96 ± 38.77	58.34 ± 1.07	0.02
0.650–150.0	600	1140.30 ± 71.56	494.91 ± 22.35	88.90 ± 9.29	472.69 ± 22.45	33.68 ± 1.06	0.03
0.650–150.0	100	190.70 ± 29.21	82.42 ± 9.03	14.84 ± 3.86	78.71 ± 9.08	13.74 ± 1.06	0.08
0.650–150.0	60	114.99 ± 22.84	49.46 ± 7.05	8.87 ± 2.98	47.25 ± 7.09	10.64 ± 1.08	0.10
0.650–150.0	30	58.30 ± 16.33	24.77 ± 4.99	4.42 ± 2.12	23.67 ± 5.02	7.43 ± 1.33	0.18
0.650–150.0	20	39.16 ± 13.34	16.49 ± 4.08	2.95 ± 1.73	15.75 ± 4.10	5.78 ± 1.69	0.29
0.650–150.0	10	19.90 ± 9.43	8.23 ± 2.89	1.47 ± 1.24	7.86 ± 2.91	3.16 ± 1.98	0.63
0.650–150.0	5	9.92 ± 7.09	4.11 ± 2.04	0.73 ± 0.87	3.93 ± 2.05	1.37 ± 1.52	1.11
0.650–150.0	4	7.92 ± 6.57	3.27 ± 1.82	0.58 ± 0.78	3.13 ± 1.83	0.98 ± 1.30	1.33
0.650–150.0	3	5.78 ± 5.90	2.43 ± 1.57	0.44 ± 0.67	2.32 ± 1.57	0.63 ± 1.03	1.65
0.650–150.0	2	3.83 ± 5.09	1.62 ± 1.28	0.29 ± 0.55	1.55 ± 1.28	0.32 ± 0.72	2.23
0.650–150.0	1	1.21 ± 3.25	0.81 ± 0.90	0.14 ± 0.38	0.77 ± 0.90	0.09 ± 0.35	3.91

Other data from Crab simulations have been provided selecting events in arbitrary GeV energy ranges, from 25 to 800 GeV.

Energy [GeV]	secs	TS	N_{on}	N_{off}	N_{exc}	Significance	$\sigma/Sign.$
25.0–32.0	1800	201.39 ± 29.92	1011.08 ± 31.81	2322.33 ± 48.51	430.50 ± 34.09	14.13 ± 1.05	0.07
25.0–32.0	600	67.56 ± 17.23	336.93 ± 18.35	774.13 ± 28.21	143.39 ± 19.62	8.15 ± 1.05	0.13
25.0–32.0	100	12.00 ± 7.25	56.26 ± 7.58	128.99 ± 11.50	24.01 ± 8.08	3.33 ± 1.06	0.32
25.0–32.0	60	7.49 ± 5.70	33.69 ± 5.85	77.27 ± 8.83	14.37 ± 6.25	2.57 ± 1.04	0.41
25.0–32.0	30	4.14 ± 4.14	16.87 ± 4.09	38.64 ± 6.22	7.21 ± 4.36	1.84 ± 0.98	0.53
25.0–32.0	20	3.04 ± 3.51	11.23 ± 3.33	25.71 ± 5.08	4.81 ± 3.56	1.54 ± 0.93	0.60
25.0–32.0	10	1.87 ± 2.72	5.61 ± 2.38	12.85 ± 3.60	2.40 ± 2.53	1.21 ± 0.83	0.69
25.0–32.0	5	1.20 ± 3.42	2.79 ± 1.67	6.39 ± 2.51	1.20 ± 1.78	0.94 ± 0.77	0.82
25.0–32.0	4	1.14 ± 4.38	2.24 ± 1.51	5.13 ± 2.27	0.96 ± 1.60	0.85 ± 0.76	0.90
25.0–32.0	3	1.24 ± 5.73	1.68 ± 1.30	3.83 ± 1.96	0.72 ± 1.39	0.73 ± 0.74	1.01
25.0–32.0	2	1.62 ± 7.44	1.12 ± 1.07	2.56 ± 1.61	0.48 ± 1.14	0.55 ± 0.69	1.24
25.0–32.0	1	2.16 ± 8.05	0.56 ± 0.74	1.29 ± 1.13	0.23 ± 0.80	0.28 ± 0.51	1.83

Energy [GeV]	secs	TS	N_{on}	N_{off}	N_{exc}	Significance	$\sigma/Sign.$
32.0–50.0	1800	693.75 ± 56.24	1702.46 ± 41.69	2951.53 ± 54.34	964.58 ± 43.60	26.17 ± 1.07	0.04
32.0–50.0	600	231.70 ± 32.57	567.34 ± 23.90	983.99 ± 31.75	321.34 ± 25.17	15.10 ± 1.07	0.07
32.0–50.0	100	39.46 ± 13.43	94.60 ± 9.70	164.12 ± 13.10	53.57 ± 10.28	6.15 ± 1.08	0.18
32.0–50.0	60	24.03 ± 10.35	56.75 ± 7.48	98.55 ± 10.14	32.11 ± 7.91	4.76 ± 1.07	0.23
32.0–50.0	30	12.46 ± 7.41	28.36 ± 5.34	49.26 ± 7.05	16.04 ± 5.62	3.35 ± 1.07	0.32
32.0–50.0	20	8.59 ± 6.15	18.90 ± 4.39	32.81 ± 5.75	10.70 ± 4.61	2.73 ± 1.07	0.39
32.0–50.0	10	4.63 ± 4.40	9.41 ± 3.07	16.43 ± 4.05	5.31 ± 3.22	1.93 ± 1.01	0.52
32.0–50.0	5	2.64 ± 3.41	4.70 ± 2.18	8.19 ± 2.85	2.65 ± 2.28	1.42 ± 0.93	0.65
32.0–50.0	4	2.21 ± 3.26	3.75 ± 1.95	6.55 ± 2.54	2.12 ± 2.05	1.29 ± 0.90	0.70
32.0–50.0	3	1.82 ± 3.92	2.82 ± 1.68	4.90 ± 2.18	1.60 ± 1.77	1.13 ± 0.87	0.77
32.0–50.0	2	1.54 ± 5.08	1.88 ± 1.37	3.28 ± 1.79	1.06 ± 1.44	0.89 ± 0.83	0.94
32.0–50.0	1	2.23 ± 7.79	0.96 ± 0.97	1.64 ± 1.27	0.55 ± 1.02	0.50 ± 0.67	1.34

Energy [GeV]	secs	TS	N_{on}	N_{off}	N_{exc}	Significance	$\sigma/Sign.$
50.0–80.0	1800	1594.54 ± 87.34	1870.21 ± 43.42	1969.43 ± 44.33	1377.85 ± 44.84	39.73 ± 1.09	0.03
50.0–80.0	600	531.97 ± 50.14	623.25 ± 25.00	656.44 ± 25.50	459.14 ± 25.79	22.93 ± 1.09	0.05
50.0–80.0	100	89.57 ± 20.65	103.87 ± 10.31	109.34 ± 10.41	76.54 ± 10.62	9.36 ± 1.10	0.12
50.0–80.0	60	53.99 ± 16.15	62.27 ± 8.00	65.65 ± 8.08	45.85 ± 8.26	7.23 ± 1.10	0.15
50.0–80.0	30	27.47 ± 11.38	31.20 ± 5.60	32.88 ± 5.67	22.98 ± 5.79	5.11 ± 1.10	0.21
50.0–80.0	20	18.69 ± 9.39	20.83 ± 4.59	21.88 ± 4.66	15.36 ± 4.75	4.18 ± 1.11	0.27
50.0–80.0	10	9.74 ± 6.66	10.40 ± 3.23	10.92 ± 3.29	7.67 ± 3.33	2.94 ± 1.09	0.37
50.0–80.0	5	5.31 ± 5.27	5.21 ± 2.30	5.47 ± 2.31	3.84 ± 2.38	2.07 ± 1.06	0.51
50.0–80.0	4	4.41 ± 5.15	4.16 ± 2.06	4.39 ± 2.09	3.07 ± 2.13	1.82 ± 1.05	0.58
50.0–80.0	3	3.65 ± 5.74	3.12 ± 1.78	3.28 ± 1.80	2.30 ± 1.84	1.52 ± 1.03	0.68
50.0–80.0	2	3.01 ± 6.55	2.08 ± 1.44	2.19 ± 1.47	1.53 ± 1.49	1.10 ± 0.95	0.87
50.0–80.0	1	2.46 ± 6.74	1.04 ± 1.01	1.10 ± 1.05	0.76 ± 1.05	0.50 ± 0.71	1.43

Energy [GeV]	secs	TS	N_{on}	N_{off}	N_{exc}	Significance	$\sigma/Sign.$
80.0–126.0	1800	2337.14 ± 104.78	1976.20 ± 44.02	1460.18 ± 38.41	1611.16 ± 45.00	48.23 ± 1.08	0.02
80.0–126.0	600	779.30 ± 60.77	658.66 ± 25.52	486.93 ± 22.17	536.93 ± 26.09	27.84 ± 1.09	0.04
80.0–126.0	100	130.46 ± 24.86	109.73 ± 10.46	81.27 ± 9.03	89.41 ± 10.68	11.35 ± 1.09	0.10
80.0–126.0	60	78.67 ± 19.29	65.86 ± 8.11	48.73 ± 6.94	53.68 ± 8.28	8.79 ± 1.09	0.12
80.0–126.0	30	39.77 ± 13.69	32.93 ± 5.76	24.33 ± 4.90	26.85 ± 5.87	6.21 ± 1.09	0.18
80.0–126.0	20	26.88 ± 11.20	21.99 ± 4.67	16.19 ± 4.00	17.94 ± 4.77	5.08 ± 1.09	0.22
80.0–126.0	10	13.79 ± 7.97	11.00 ± 3.33	8.12 ± 2.84	8.97 ± 3.38	3.57 ± 1.10	0.31
80.0–126.0	5	7.41 ± 6.58	5.50 ± 2.35	4.09 ± 2.02	4.47 ± 2.40	2.45 ± 1.12	0.46
80.0–126.0	4	6.23 ± 6.49	4.40 ± 2.09	3.26 ± 1.82	3.58 ± 2.14	2.11 ± 1.13	0.53
80.0–126.0	3	5.08 ± 6.57	3.30 ± 1.80	2.46 ± 1.58	2.68 ± 1.85	1.67 ± 1.11	0.67
80.0–126.0	2	4.10 ± 7.01	2.21 ± 1.49	1.63 ± 1.28	1.80 ± 1.53	1.14 ± 1.03	0.90
80.0–126.0	1	2.92 ± 6.35	1.12 ± 1.06	0.81 ± 0.90	0.91 ± 1.08	0.47 ± 0.72	1.56

Energy [GeV]	secs	TS	N_{on}	N_{off}	N_{exc}	Significance	$\sigma/Sign.$
126.0–200.0	1800	2650.20 ± 111.90	1668.78 ± 40.50	787.13 ± 27.82	1472.00 ± 41.16	51.40 ± 1.09	0.02
126.0–200.0	600	883.59 ± 65.01	556.12 ± 23.49	262.44 ± 16.09	490.51 ± 23.89	29.66 ± 1.10	0.04
126.0–200.0	100	148.43 ± 26.78	92.83 ± 9.66	43.76 ± 6.59	81.89 ± 9.81	12.12 ± 1.10	0.09
126.0–200.0	60	89.59 ± 20.65	55.75 ± 7.42	26.21 ± 5.09	49.20 ± 7.54	9.39 ± 1.09	0.12
126.0–200.0	30	45.40 ± 14.83	27.93 ± 5.30	13.09 ± 3.62	24.66 ± 5.39	6.65 ± 1.11	0.17
126.0–200.0	20	30.42 ± 12.19	18.57 ± 4.34	8.73 ± 2.97	16.39 ± 4.41	5.41 ± 1.12	0.21
126.0–200.0	10	15.68 ± 8.79	9.26 ± 3.05	4.37 ± 2.10	8.17 ± 3.10	3.74 ± 1.17	0.31
126.0–200.0	5	8.85 ± 7.87	4.64 ± 2.15	2.18 ± 1.47	4.09 ± 2.19	2.27 ± 1.29	0.57
126.0–200.0	4	7.57 ± 7.86	3.70 ± 1.92	1.74 ± 1.31	3.27 ± 1.95	1.83 ± 1.27	0.69
126.0–200.0	3	6.35 ± 8.10	2.77 ± 1.66	1.30 ± 1.13	2.44 ± 1.69	1.33 ± 1.18	0.89
126.0–200.0	2	5.30 ± 7.87	1.85 ± 1.36	0.86 ± 0.93	1.63 ± 1.38	0.77 ± 0.96	1.25
126.0–200.0	1	2.94 ± 5.60	0.92 ± 0.96	0.42 ± 0.65	0.82 ± 0.98	0.26 ± 0.57	2.19

Energy [GeV]	secs	TS	N_{on}	N_{off}	N_{exc}	Significance	$\sigma/Sign.$
200.0–316.0	1800	2188.95 ± 101.24	1145.18 ± 33.88	362.12 ± 19.20	1054.65 ± 34.18	46.75 ± 1.08	0.02
200.0–316.0	600	731.35 ± 58.77	381.97 ± 19.46	120.56 ± 11.03	351.83 ± 19.70	27.01 ± 1.09	0.04
200.0–316.0	100	122.72 ± 23.93	63.68 ± 7.98	20.10 ± 4.49	58.65 ± 8.05	11.02 ± 1.08	0.10
200.0–316.0	60	73.84 ± 18.47	38.18 ± 6.17	12.09 ± 3.46	35.16 ± 6.22	8.52 ± 1.08	0.13
200.0–316.0	30	37.63 ± 13.40	19.16 ± 4.42	6.04 ± 2.45	17.65 ± 4.46	6.02 ± 1.13	0.19
200.0–316.0	20	25.55 ± 11.29	12.75 ± 3.57	4.01 ± 2.01	11.75 ± 3.60	4.80 ± 1.27	0.26
200.0–316.0	10	13.83 ± 8.95	6.37 ± 2.52	2.01 ± 1.42	5.87 ± 2.54	2.89 ± 1.50	0.52
200.0–316.0	5	7.94 ± 7.59	3.19 ± 1.78	1.00 ± 1.00	2.94 ± 1.80	1.36 ± 1.31	0.96
200.0–316.0	4	6.61 ± 7.39	2.56 ± 1.60	0.80 ± 0.90	2.36 ± 1.61	1.00 ± 1.16	1.16
200.0–316.0	3	4.91 ± 6.31	1.94 ± 1.39	0.59 ± 0.76	1.79 ± 1.40	0.67 ± 0.97	1.46
200.0–316.0	2	3.15 ± 5.26	1.29 ± 1.13	0.41 ± 0.63	1.19 ± 1.14	0.34 ± 0.68	2.01
200.0–316.0	1	1.55 ± 3.77	0.65 ± 0.81	0.20 ± 0.45	0.60 ± 0.82	0.10 ± 0.35	3.61

Energy [GeV]	secs	TS	N_{on}	N_{off}	N_{exc}	Significance	$\sigma/Sign.$
316.0–500.0	1800	1563.39 ± 84.96	750.00 ± 27.20	186.59 ± 13.71	703.36 ± 27.45	39.52 ± 1.07	0.03
316.0–500.0	600	521.73 ± 48.45	249.93 ± 15.48	62.15 ± 7.96	234.40 ± 15.62	22.82 ± 1.06	0.05
316.0–500.0	100	87.82 ± 20.14	41.65 ± 6.39	10.35 ± 3.23	39.06 ± 6.46	9.31 ± 1.08	0.12
316.0–500.0	60	52.96 ± 15.62	24.95 ± 4.97	6.20 ± 2.48	23.40 ± 5.02	7.19 ± 1.11	0.16
316.0–500.0	30	27.14 ± 11.37	12.50 ± 3.50	3.09 ± 1.75	11.73 ± 3.54	4.83 ± 1.46	0.30
316.0–500.0	20	18.56 ± 9.70	8.33 ± 2.87	2.06 ± 1.43	7.82 ± 2.89	3.54 ± 1.65	0.47
316.0–500.0	10	10.08 ± 7.66	4.17 ± 2.03	1.03 ± 1.01	3.91 ± 2.05	1.68 ± 1.51	0.90
316.0–500.0	5	5.34 ± 6.03	2.08 ± 1.45	0.52 ± 0.73	1.95 ± 1.46	0.63 ± 0.99	1.56
316.0–500.0	4	4.37 ± 5.79	1.66 ± 1.29	0.42 ± 0.65	1.56 ± 1.30	0.44 ± 0.82	1.85
316.0–500.0	3	3.48 ± 5.27	1.25 ± 1.12	0.32 ± 0.56	1.17 ± 1.13	0.28 ± 0.64	2.28
316.0–500.0	2	2.17 ± 4.11	0.83 ± 0.91	0.21 ± 0.46	0.78 ± 0.91	0.14 ± 0.44	3.12
316.0–500.0	1	1.05 ± 3.18	0.41 ± 0.64	0.11 ± 0.32	0.38 ± 0.64	0.04 ± 0.21	5.75

Energy [GeV]	secs	TS	N_{on}	N_{off}	N_{exc}	Significance	$\sigma/Sign.$
500.0–800.0	1800	1185.82 ± 74.59	541.12 ± 23.47	114.72 ± 10.74	512.44 ± 23.67	34.42 ± 1.08	0.03
500.0–800.0	600	396.06 ± 42.56	180.41 ± 13.37	38.24 ± 6.29	170.85 ± 13.47	19.87 ± 1.07	0.05
500.0–800.0	100	66.61 ± 17.72	30.01 ± 5.55	6.41 ± 2.57	28.41 ± 5.59	8.07 ± 1.15	0.14
500.0–800.0	60	40.26 ± 13.71	17.99 ± 4.31	3.84 ± 1.97	17.03 ± 4.34	6.07 ± 1.44	0.24
500.0–800.0	30	20.55 ± 9.71	9.00 ± 3.04	1.93 ± 1.37	8.52 ± 3.06	3.64 ± 1.81	0.50
500.0–800.0	20	13.97 ± 7.95	6.01 ± 2.48	1.29 ± 1.14	5.68 ± 2.49	2.43 ± 1.75	0.72
500.0–800.0	10	7.41 ± 6.09	3.02 ± 1.75	0.65 ± 0.81	2.86 ± 1.76	1.00 ± 1.26	1.26
500.0–800.0	5	3.96 ± 5.30	1.51 ± 1.23	0.33 ± 0.58	1.43 ± 1.24	0.33 ± 0.71	2.15
500.0–800.0	4	3.47 ± 5.29	1.20 ± 1.10	0.26 ± 0.52	1.14 ± 1.10	0.22 ± 0.57	2.56
500.0–800.0	3	2.56 ± 4.95	0.90 ± 0.95	0.20 ± 0.45	0.85 ± 0.96	0.14 ± 0.43	3.19
500.0–800.0	2	1.89 ± 4.66	0.59 ± 0.78	0.13 ± 0.37	0.56 ± 0.78	0.07 ± 0.29	4.41
500.0–800.0	1	1.61 ± 4.64	0.30 ± 0.55	0.06 ± 0.25	0.28 ± 0.55	0.02 ± 0.13	8.35

References

[1] S. S. Wilks. “The Large-Sample Distribution of the Likelihood Ratio for Testing Composite Hypotheses”. In: *Ann. Math. Statist.* 9.1 (Mar. 1938), pp. 60–62 (cit. on p. 24).
DOI: `10.1214/aoms/1177732360`.

[2] W. Cash. “Parameter estimation in astronomy through application of the likelihood ratio.” In: *The Astrophysical Journal* 228 (Mar. 1979), pp. 939–947 (cit. on p. 24).
DOI: `10.1086/156922`.

[3] L. Maraschi and A. Treves. “A model for LS I +61 303.” In: *Monthly Notices of the Royal Astronomical Society* 194 (Jan. 1981), 1P–5 (cit. on p. 10).
DOI: `10.1093/mnras/194.1.1P`.

[4] Ti-Pei Li and Yu-Qian Ma. “Analysis methods for results in gamma-ray astronomy”. In: *The Astrophysical Journal* 272 (Sept. 1983), pp. 317–324 (cit. on pp. 24, 39).
DOI: `10.1086/161295`.

[5] A. M. Hillas. “Cerenkov light images of EAS produced by primary gamma rays and by nuclei”. In: *Proc. of the 19th ICRC (International Cosmic Ray Conf.)* (1985), pp. 445–448 (cit. on p. 14).

[6] J. L. Hopkins. “Dead Time”. In: *International Amateur-Professional Photoelectric Photometry Communications* 46 (Dec. 1991), p. 9 (cit. on p. 56).

[7] V.P. Fomin, A.A. Stepanian, R.C. Lamb, D.A. Lewis, M. Punch, T.C. Weekes. “New methods of atmospheric Cherenkov imaging for gamma-ray astronomy. I. The false source method”. In: *Astroparticle Physics* 2 (2 May 1994), pp. 137–150 (cit. on pp. 27, 28).
DOI: `10.1016/0927-6505(94)90036-1`.

[8] J. R. Mattox et al. “The Likelihood Analysis of EGRET Data”. In: *The Astrophysical Journal* 461 (Apr. 1996), p. 396 (cit. on p. 23).
DOI: `10.1086/177068`.

[9] F. Aharonian et al. “Discovery of the binary pulsar PSR B1259-63 in very-high-energy gamma rays around periastron with HESS”. In: *Astronomy and Astrophysics* 442.1 (Oct. 2005), pp. 1–10 (cit. on p. 9).
DOI: `10.1051/0004-6361:20052983`.

[10] F. Aharonian et al. “Discovery of Very High Energy Gamma Rays Associated with an X-ray Binary”. In: *Science* 309.5735 (July 2005), pp. 746–749 (cit. on p. 9).
DOI: `10.1126/science.1113764`.

[11] D. Berge, S. Funk, and J. Hinton. “Background modelling in very-high-energy γ-ray astronomy”. In: *Astronomy and Astrophysics* 466.3 (May 2007), pp. 1219–1229 (cit. on p. 26).
DOI: `10.1051/0004-6361:20066674`.

[12] J. Albert et al. “Implementation of the Random Forest method for the Imaging Atmospheric Cherenkov Telescope MAGIC”. In: *Nuclear Instruments and Methods in Physics Research Section A: Accelerators, Spectrometers, Detectors and Associated Equipment* 588.3 (2008), pp. 424–432. ISSN: 0168-9002 (cit. on p. 16).
DOI: `https://doi.org/10.1016/j.nima.2007.11.068`.

[13] A. A. Abdo et al. “Gamma-Ray Emission from the Shell of Supernova Remnant W44 Revealed by the Fermi LAT”. In: *Science* 327.5969 (2010), pp. 1103–1106. ISSN: 0036-8075 (cit. on p. 9).
DOI: `10.1126/science.1182787`.

[14] Justin D. Finke, Soebur Razzaque, and Charles D. Dermer. “Modeling the Extragalactic Background Light from Stars and Dust”. In: *The Astrophysical Journal* 712.1 (Mar. 2010), pp. 238–249 (cit. on p. 12).
DOI: `10.1088/0004-637X/712/1/238`.

[15] Brant E. Robertson and Richard S. Ellis. “CONNECTING THE GAMMA RAY BURST RATE AND THE COSMIC STAR FORMATION HISTORY: IMPLICATIONS FOR REIONIZATION AND GALAXY EVOLUTION”. In: *The Astrophysical Journal* 744.2 (Dec. 2011), p. 95 (cit. on p. 10).
DOI: `10.1088/0004-637x/744/2/95`.

[16] J. Beringer et al. “Review of Particle Physics”. In: *Phys. Rev. D* 86 (1 July 2012), p. 010001 (cit. on p. 7).
DOI: `10.1103/PhysRevD.86.010001`.

[17] Rudy C. Gilmore et al. “Semi-analytic modelling of the extragalactic background light and consequences for extragalactic gamma-ray spectra”. In: *Monthly Notices of the Royal Astronomical Society* 422.4 (May 2012), pp. 3189–3207. ISSN: 0035-8711 (cit. on pp. 12, 47).
DOI: `10.1111/j.1365-2966.2012.20841.x`.

[18] Andreja Gomboc. “Unveiling the secrets of gamma ray bursts”. In: *Contemporary Physics* 53.4 (2012), pp. 339–355 (cit. on p. 12).
DOI: `10.1080/00107514.2012.701453`.

[19] Morlino, G. and Caprioli, D. “Strong evidence for hadron acceleration in Tycho´s supernova remnant”. In: *A&A* 538 (2012), A81 (cit. on p. 9).
DOI: `10.1051/0004-6361/201117855`.

[20] F.A. Aharonian. “Gamma rays from supernova remnants”. In: *Astroparticle Physics* 43 (2013), pp. 71–80. ISSN: 0927-6505 (cit. on p. 9).
DOI: `DOI10.1016/j.astropartphys.2012.08.007`.

[21] Andrea Bulgarelli et al. “The Real-Time Analysis of the Cherenkov Telescope Array Observatory”. In: *International Cosmic Ray Conference*. Vol. 33. International Cosmic Ray Conference. Jan. 2013, p. 3099 (cit. on pp. 20, 51).

[22] V.K. Dhar et al. “Artificial Neural Network based γ-hadron segregation methodology for TACTIC telescope”. In: *Nuclear Instruments and Methods in Physics Research Section A: Accelerators, Spectrometers, Detectors and Associated Equipment* 708 (2013), pp. 56–71. ISSN: 0168-9002 (cit. on p. 15).
DOI: `https://doi.org/10.1016/j.nima.2012.12.118`.

[23] L. Nava et al. “Afterglow emission in Gamma-Ray Bursts: I. Pair-enriched ambient medium and radiative blast waves”. In: *Monthly Notices of the Royal Astronomical Society* 433.3 (June 2013), pp. 2107–2121. ISSN: 0035-8711 (cit. on p. 45).
DOI: `10.1093/mnras/stt872`.

[24] J. Aleksić et al. “The major upgrade of the MAGIC telescopes, Part II: A performance study using observations of the Crab Nebula”. In: *Astroparticle Physics* 72 (Jan. 2016), pp. 76–94 (cit. on p. 17).
DOI: `10.1016/j.astropartphys.2015.02.005`.

[25] Gabici, Stefano and Aharonian, Felix. “Gamma-ray emission from young supernova remnants: Hadronic or leptonic?” In: *EPJ Web of Conferences* 121 (2016), p. 04001 (cit. on p. 9).
DOI: `10.1051/epjconf/201612104001`.

[26] HESS Collaboration et al. “Acceleration of petaelectronvolt protons in the Galactic Centre”. In: *Nature* 531.7595 (Mar. 2016), pp. 476–479 (cit. on p. 17).
DOI: `10.1038/nature17147`.

[27] Knödlseder, J. et al. “GammaLib and ctools - A software framework for the analysis of astronomical gamma-ray data”. In: *A&A* 593 (2016), A1 (cit. on p. 30).
DOI: `10.1051/0004-6361/201628822`.

[28] Grzegorz (Greg) Madejski and Marek Sikora. “Gamma-Ray Observations of Active Galactic Nuclei”. In: *Annual Review of Astronomy and Astrophysics* 54 (Sept. 2016), pp. 725–760 (cit. on p. 10).
DOI: `10.1146/annurev-astro-081913-040044`.

[29] Dan Hooper, Ilias Cholis, and Tim Linden. “TeV gamma rays from Galactic Center pulsars”. In: *Physics of the Dark Universe* 21 (Sept. 2018), pp. 40–46 (cit. on p. 8).
DOI: `10.1016/j.dark.2018.05.004`.

[30] Barbara Patricelli et al. *GW COSMoS: Gravitational Wave COmpact binary SysteM Simulations*. Oct. 2018 (cit. on p. 46).
DOI: `10.6084/m9.figshare.c.4243595.v1`.

[31] Maurizio Spurio. *Probes of Multimessenger Astrophysics. Charged Cosmic Rays, Neutrinos, gamma-Rays and Gravitational Waves*. Springer, 2018 (cit. on pp. 9, 12, 14, 15).

[32] M. Amenomori et al. "First Detection of Photons with Energy beyond 100 TeV from an Astrophysical Source". In: *Phys. Rev. Lett.* 123 (5 July 2019), p. 051101 (cit. on p. 8).
DOI: `10.1103/PhysRevLett.123.051101`.

[33] Roger Blandford, David Meier, and Anthony Readhead. "Relativistic Jets from Active Galactic Nuclei". In: *Annual Review of Astronomy and Astrophysics* 57 (Aug. 2019), pp. 467–509 (cit. on p. 10).
DOI: `10.1146/annurev-astro-081817-051948`.

[34] CTA Consortium and Rene A. Ong. "The Cherenkov Telescope Array Science Goals and Current Status". In: *European Physical Journal Web of Conferences*. Vol. 209. European Physical Journal Web of Conferences. Sept. 2019, p. 01038 (cit. on p. 19).
DOI: `10.1051/epjconf/201920901038`.

[35] Matthews, James H. et al. "Cosmic ray acceleration to ultrahigh energy in radio galaxies". In: *EPJ Web Conf.* 210 (2019), p. 04002 (cit. on p. 10).
DOI: `10.1051/epjconf/201921004002`.

[36] M. Seglar-Arroyo et al. "The gravitational wave follow-up program of the Cherenkov Telescope Array". In: *36th International Cosmic Ray Conference (ICRC2019)*. Vol. 36. International Cosmic Ray Conference. July 2019, p. 790 (cit. on p. 21).

[37] S. Lombardi et al. "First detection of the Crab Nebula at TeV energies with a Cherenkov telescope in a dual-mirror Schwarzschild-Couder configuration: the ASTRI-Horn telescope". In: *Astronomy and Astrophysics* 634, A22 (Feb. 2020), A22 (cit. on p. 19).
DOI: `10.1051/0004-6361/201936791`.